DISS. ETH NO. 28096

X-RAY IMAGING OF SPIN-WAVE DYNAMICS: FROM FERROMAGNETIC TO ANTIFERROMAGNETIC SYSTEMS

A thesis submitted to attain the degree of

DOCTOR OF SCIENCES of ETH ZURICH

(Dr. sc. ETH Zurich)

presented by

SINA MAYR

M.Sc.
Technical University of Munich

born on 25.09.1991

citizen of
Germany

accepted on the recommendation of

Prof. Dr. Laura Heyderman
Dr. Jörg Raabe
Prof. Dr. Pietro Gambardella
Prof. Dr. Christian Back

2021

Abstract

Spin waves are collective excitations of ordered spin systems, for which, in a classical view, the magnetic moments precess with a spatially periodic phase shift that determines their wavelength. In terms of applications, the use of spin waves as signal carriers in future spintronic logic and memory devices has the advantages of potentially lower power consumption and improved miniaturisation compared to today's charge-based technologies. The use of antiferromagnetic systems with their ultrafast spin dynamics could additionally boost the operational speed of future spin-wave devices. As the dynamics of spin waves in antiferromagnets is still largely unknown, ferrimagnets offer an ideal intermediate step on the way towards the investigation of fully antiferromagnetic systems.

The research projects described in this thesis follow the route from ferromagnetic towards antiferromagnetic magnonic systems. To directly image spin waves in these systems with a spatial and temporal resolution on the order of 10 nm and 10 ps in a phase-resolved way, time-resolved scanning transmission x-ray microscopy (TR-STXM) was employed. A process to fabricate x-ray transparent windows into bulk samples based on Xe plasma focused ion beam milling was developed to be able to image spin waves in single crystalline systems.

At first, the manipulation of short-wavelength spin-wave emission from vortex cores in both a synthetic ferrimagnet and single-layer ferromagnetic films with an applied static magnetic field is discussed. In the single-layer system, the vortex core exhibits a field-induced expansion and thus becomes a source for the directional emission and focussing of spin waves.

Subsequently, the direct imaging of spin waves with nanoscale wavelengths in ferromagnetic systems at high frequencies exceeding 30 GHz is demonstrated. Acoustic and optical modes were observed in coupled ferromagnetic systems with antiparallel magnetic orientation. In single-layer systems, spin-wave modes up to the fourth perpendicular standing order were directly imaged.

Furthermore, spin waves in ferrimagnetic Ga-doped yttrium-iron-garnet (YIG) with a reduced net magnetization to approach compensation are discussed. Despite their relatively long wavelengths, the spin waves in this material exhibit exchange-governed dynamics. Moreover, a non-linear effect in the spin-wave excitation was observed, which leads to giant spin-wave precession angles exceeding 20°.

Finally, the coherent excitation and imaging of spin-wave dynamics in antiferromagnetic hematite at room temperature above 20 GHz is demonstrated.

Kurzfassung

Spinwellen sind kollektive Anregungen von geordneten Spinsystemen, bei denen, klassisch betrachtet, die magnetischen Momente mit einer räumlich periodischen Phasenverschiebung, die die Wellenlänge bestimmt, präzessieren. In Bezug auf Anwendungen bietet die Verwendung von Spinwellen als Signalträger in zukünftigen spintronischen Logik- und Speicherbauteilen zwei wesentliche Vorteile gegenüber den heutigen ladungsbasierten Technologien: einen potenziell geringeren Energieverbrauch und bessere Miniaturisierungsmöglichkeiten. Daneben könnte die Verwendung antiferromagnetischer Systeme mit intrinsisch ultraschneller Spindynamik die Operationsgeschwindigkeit künftiger Spinwellen-Bauelemente zusätzlich erhöhen. Da die Dynamik von Spinwellen in Antiferromagneten zur Zeit noch weitgehend unbekannt ist, bieten Ferrimagnete einen idealen Zwischenschritt auf dem Weg zur Untersuchung vollständig antiferromagnetischer Systeme.

Die in dieser Arbeit beschriebenen Forschungsprojekte befassen sich mit dem Übergang von ferromagnetischen zu antiferromagnetischen magnonischen Systemen. Für die phasenaufgelöste Abbildung von Spinwellen in diesen Systemen mit einer kombinierten räumlichen und zeitlichen Auflösung in der Größenordnung von 10 nm und 10 ps, wurde zeitaufgelöste Rastertransmissionsröntgenmikroskopie (TR-STXM) eingesetzt. Um Spinwellen in einkristallinen Systemen abbilden zu können, wurde ein Verfahren zur Herstellung von röntgentransparenten Fenstern in massiven Proben entwickelt, das auf fokussiertem Ionenstrahldünnen mit in einem Plasma erzeugten Xe-Ionen basiert.

Zunächst wird der Einfluss eines statischen Magnetfelds auf die kurzwellige Spinwellenemission von magnetischen Wirbelkernen sowohl in einem synthetischen Ferrimagneten als auch in einschichtigen ferromagnetischen Filmen diskutiert. Im einschichtigen System weist der Wirbelkern eine feldinduzierte Ausdehnung auf und wird so zu einer Quelle für die gerichtete Emission und Fokussierung von Spinwellen.

Anschließend wird die direkte Abbildung von Spinwellen mit nanoskaligen Wellenlängen in ferromagnetischen Systemen bei hohen Frequenzen von über 30 GHz gezeigt. Akustische und optische Moden wurden in gekoppelten ferromagnetischen Systemen mit antiparalleler magnetischer Orientierung beobachtet. In einschichtigen Systemen wurden Spinwellenmoden bis zur vierten senkrecht stehenden Ordnung direkt abgebildet.

Außerdem werden Spinwellen in ferrimagnetischem Ga-dotiertem Yttrium-Eisen-Granat (YIG) mit reduzierter Nettomagnetisierung in Annäherung an den magnetischen Kompensationspunkt diskutiert. Trotz ihrer relativ langen Wellenlängen zeigen die Spinwellen in diesem Material eine durch die Austauschwechselwirkung dominierte Dynamik. Darüber hinaus wurde ein nichtlinearer Effekt bei der Spinwellenanregung beobachtet, der zu außergewöhnlich großen Präzessionswinkeln der Spinwellen von über 20° führt.

Abschließend wird die kohärente Anregung und Abbildung der Spinwellen-Dynamik in antiferromagnetischem Hämatit bei Raumtemperatur oberhalb von 20 GHz demonstriert.

Contents

1 Introduction

Novel developments in different areas of spintronics, which is the research field that utilises the spin degree of freedom of electrons, hold great potential to cope with the increasing societal demand for computational power and data storage with a low environmental footprint.

In this regard, new concepts and materials will be needed that are able to make devices not only smaller and faster, but at the same time more energy efficient. A concept to achieve this is to use a different way to propagate and process information: Instead of displacing charges, information can be transmitted by waves in magnetic materials referred to as spin waves. Their quasiparticles are called magnons, from which the name of the associated research field, magnonics, is derived.

When compared to present technology, the use of spin waves as signal carriers has two main advantages. Given that the displacement of electric charges results in the dissipation of heat via ohmic losses, the first advantage originates from the fact that no charges are displaced during spin-wave propagation. This could lead to a comparatively lower power consumption of spin-wave based devices with respect to conventional technologies. The second advantage is that the wavelengths of spin waves are, at the same frequency, often orders of magnitude shorter than those of electromagnetic waves [1]. This means that devices relying on spin waves as signal carriers have a high potential for miniaturisation and, to use this to full capacity, it will be indispensable to utilise ultra-short spin waves with nanoscale wavelengths.

Present spin-wave computing concepts mainly rely on mechanisms such as wave interference and non-linear interaction of waves. Consequently, any technological implementation will require full control over the efficient excitation, low-loss propagation, reliable manipulation, and robust detection of spin waves with short wavelengths. To this end, significant advances have been made in ferromagnetic and ferrimagnetic systems over the past years.

With regards to efforts to increase the computation performance, there is a strong demand for expanding the bandwidth of future magnonic devices, as both the signal transfer rate and processing speed scale with the operation frequency. While a decrease of wavelengths typically coincides with an increase of the frequencies, the fundamental resonances of ferromagnets and ferrimagnets often do not exceed the low GHz range, and only highly anisotropic systems provide a means to partially circumvent this restriction.

Prime candidates to boost the intrinsic frequencies for spin-wave computing are antiferromagnetic materials with resonances ranging from 10s of GHz up to the THz regime. The reason for this is that, in contrast to ferromagnets where, in the absence of an external magnetic field, the uniform precession frequency is only determined by anisotropy, antiferromagnets exhibit dynamic sublattice canting, which results in an additional exchange contribution and thus leads to higher frequencies [2, 3].

While pioneering investigations of coherent spin dynamics in antiferromagnets already go back to the 1950s [4, 5], and seminal advances were reported recently [6, 7], a clear understanding and direct observation of the real space dynamics of antiferromagnetic spin waves has not been achieved to date. One reason for this is the difficulty in spatially probing antiferromagnetic systems.

Ferrimagnets, which exhibit a net magnetization despite having antiferromagnetically coupled sublattices, offer possibilities to study effects similar to those found in antiferromagnets such as sublattice canting, while still being probed by similar means to those used to investigate ferromagnets. Moreover, their magnetization can be tuned by varying their constituents or by doping to reach magnetization compensation [8]. Therefore, ferrimagnets offer an ideal playground and intermediate step for scientific studies on the way towards the investigation of fully antiferromagnetic systems.

To study spin waves with nanoscale wavelengths and gain a better understanding of their properties, advanced magnetic imaging techniques with high spatial and temporal resolutions are required. For probing spin waves on the nanoscale in both ferro- and ferrimagnets, scanning transmission x-ray microscopy (STXM) exploiting the x-ray magnetic circular dichroism (XMCD) effect has already been established [9, 10], whereas antiferromagnetic spin waves are yet to be imaged by direct means. Here, the x-ray magnetic linear dichroism (XMLD) effect, in combination with x-ray microscopy, stands out as one of the few techniques that allows for the direct imaging of antiferromagnets with nanoscale resolution [11, 12]. This means that STXM is the ideal technique to study spin-wave dynamics in ferromagnetic, ferrimagnetic and antiferromagnetic systems, as it will be shown in this thesis.

The projects presented in this thesis follow the route from ferromagnetic towards antiferromagnetic magnonic systems. At first the advanced generation and manipulation of short wavelength and high frequency spin waves in ferromagnetic systems is presented. Then, the dynamics in low-damping ferrimagnets approaching their magnetic compensation point are described. Finally, the generation and direct imaging of spin waves in an antiferromagnetic system is demonstrated. This thesis is structured as follows:

In **Chapter 2**, a brief introduction is given to the essential theoretical background of magnetism and spin waves in particular.

In **Chapter 3**, the sample fabrication with electron beam lithography as well as scanning transmission x-ray microscopy (STXM), which was used throughout this project to image spin waves, are explained. Additionally, a technique developed to fabricate soft x-ray transparent windows out of bulk substrates is presented.

In **Chapter 4** the manipulation of the emission of short-wavelength spin waves from a vortex core in antiferromagnetically coupled and single-layer ferromagnetic systems by applying a static magnetic bias field is shown. By expanding the vortex core in a single layer system, it becomes a source for the directional emission of spin waves and even allows for focusing effects.

In **Chapter 5** the direct imaging of spin waves in ferromagnetic systems at high frequencies exceeding 30 GHz is demonstrated. Different modes are imaged in coupled and single-layer systems and various means to influence the spin-wave dispersion relation are analysed.

In **Chapter 6** spin waves measured in the low-damping ferrimagnet yttrium-iron-garnet (YIG) are shown, which is additionally doped with Ga to lower its magnetization to reach compensation. Effects such as non-linearities in the spin-wave angle and exchange-dominated spin waves at long wavelengths, are discussed. Furthermore, domain and domain-wall dynamics in the system are presented.

In **Chapter 7** the possibility to directly image dynamics in antiferromagnetic hematite is introduced. The spin reorientation transition from an easy-axis to an easy-plane antiferromagnet is shown. Additionally, it is demonstrated that spin-wave dynamics can be coherently excited and imaged in the canted antiferromagnet hematite at room temperature.

In **Chapter 8** the results of the different chapters are summarised and an outlook to future research directions is given.

Parts and ideas of this introduction have been submitted for publication as part of Chumak et. al, "Roadmap on Spin-Wave Computing", IEEE Transactions on Magnetics, as Mayr and Wintz, "Increasing the signal bandwidth - From ferromagnetic to antiferromagnetic magnonic systems" [13]. My contribution to this work is co-writing the article.

2 Background: Magnetism and Spin Waves

Magnetism and magnetization dynamics are a sub-field of condensed matter physics. In this chapter, a brief introduction is given to the theoretical background of the underlying phenomena of different forms of magnetic order. General magnetization dynamics are explained before spin waves, which are the main focus of this thesis, are introduced. Their properties as well as common ways to generate and detect them are described.

2.1 Ferro-, Ferri- and Antiferromagnetism

Whereas electrodynamics describes the interactions between currents and magnetic fields, magnetism in matter is a quantum-mechanical phenomenon, which cannot be explained by classical physics. In contrast to diamagnets, in which magnetic moments can be induced by an external magnetic field, and paramagnets, which have unordered magnetic moments, which can be ordered by an external magnetic field, certain materials exhibit spontaneous magnetic order. Such spontaneous magnetic order can arise when the wave functions of particles overlap [14]. For the case of two electrons, the Heisenberg uncertainty principle states that the kinetic energy can be lowered if the electrons are delocalised [14]. According to the Pauli exclusion principle, two electrons, as fermions, cannot be at the same position, i.e. share the same orbital, at the same time if they have the same spin [15]. This means that their total wave function must be antisymmetric; a condition that can be fulfilled by splitting the antisymmetric wave function into a spatial and a spin part of which one is antisymmetric and the other one symmetric. The type of symmetry of the spatial wave function is related to the charge distribution and therefore to the potential energy of the system [16]. The energy difference between the two spin symmetries is defined as the exchange constant J. For $J > 0$ a symmetric spin function, corresponding to a parallel alignment of the spins, is favoured, while for $J < 0$ an antiparallel alignment of the spins is preferred [14]. The effective spin Hamiltonian can then be written as

$$\hat{\mathcal{H}}^{spin} = -2J\mathbf{S}_i \cdot \mathbf{S}_j. \tag{2.1}$$

As the exchange interaction acts between all spins in a system, these can be summed up leading to the Hamiltonian of the Heisenberg model:

$$\hat{\mathcal{H}} = -\sum_{i,j} J_{ij} \mathbf{S}_i \cdot \mathbf{S}_j. \tag{2.2}$$

Most often only the interaction between neighbouring spins has to be accounted for, with $J = 0$ otherwise [15].

The Heisenberg model works well for localised electrons as they occur e.g. in rare earths and oxides. However, for delocalised electrons as they occur in metals, where the interaction between an electron and all other electrons has to be considered, a band model should be applied instead. Here the electrons move more freely within a band. For a non-ferromagnetic material, the same number of electrons are spin-up and spin-down polarised at the Fermi energy. While flipping the spin of some electrons will increase the overall kinetic energy, it can reduce the exchange energy which favours a parallel alignment of the spins [15]. If this reduces the overall energy, there will be a spin-split band structure and the material will be ferromagnetic [14]. For elements, this condition is only fulfilled for the classical band ferromagnets Fe, Co and Ni.

The existence of opposing signs of J indicates the occurrence both of ferromagnets that show parallel alignment of magnetic moments (Fig. 2.1a), and of antiferromagnets and ferrimagnets that exhibit an antiparallel alignment. In their simplest form, antiferro- and ferrimagnets can be understood as having two sublattices, with the magnetic moments aligned parallel within each sublattice, but with opposite orientation of the sublattices. The difference between antiferro- and ferrimagnets is that in antiferromagnets the two sublattices have the same magnetization, so that there is no net magnetization (Fig. 2.1b), whereas in ferrimagnets the sublattices have different magnetizations, resulting in a net magnetization (Fig. 2.1c). Ferrimagnetism can occur for different magnetic elements or even for the same element but with atoms occupying different lattice sites, as it is the case, e.g., for yttrium iron garnet [17]. It should be noted that such magnetic ordering only occurs below a certain temperature for each material, which is referred to as Curie temperature (T_C) for ferro- and ferrimagnets and Néel temperature (T_N) for antiferromagnets. Above this temperature, the material is paramagnetic. Some ferrimagnets can additionally have a compensation temperature, where the magnetizations of the sublattices cancel out.

In addition to the exchange interaction that favours a collinear alignment of the magnetic moments, there exists an antisymmetric exchange interaction, referred to as Dzyaloshinsky-Moriya interaction (DMI) [18, 19], which can lead to a canting of

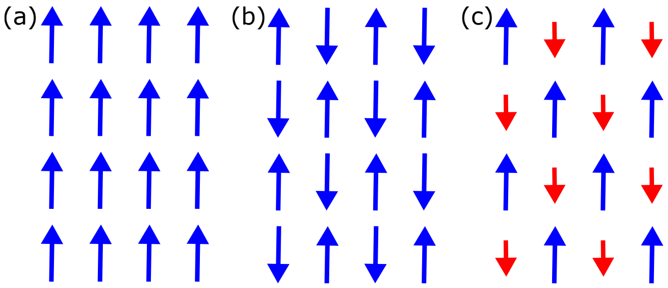

Figure 2.1: Schematics of spontaneous magnetic configurations. a) Ferromagnetic alignment with magnetic moments pointing in the same direction. b) Antiferromagnetic alignment, where the magnetic moments have the same magnitude but with alternating orientations, resulting in no net magnetization. c) Ferrimagnetic alignment, where the magnitude of the moments on the two antiparallel sublattices is not equal and a net magnetization of the material occurs.

magnetic moments. This leads to the following term in the Hamiltonian [15]:

$$\hat{\mathcal{H}}^{DMI} = \mathbf{D} \cdot \mathbf{S}_i \times \mathbf{S}_j . \tag{2.3}$$

2.2 Micromagnetic Approximation

Despite magnetism being a quantum phenomenon, a many-body quantum mechanical description is not practically possible for typical condensed matter systems due to the amount of magnetic moments to consider. Hence, a mean-field approach, called micromagnetic approximation, is often used, where a local spatial average of the magnetization is assumed [15]. The system will occupy a state of minimum energy to which there are different contributions [14]. Whereas ferri- and antiferromagnetic systems can be treated analogously, the description for ferromagnets is the most straightforward and the different contributions to the energy are as follows:

- The exchange energy is caused by the previously described exchange interaction and leads to a parallel alignment of the magnetic moments as shown in Figure 2.2a. It is an intrinsic and local energy contribution of the system and is given by: [20]

  $$E_{exchange} = \frac{A}{M_s^2} \int_{sample} (\nabla \mathbf{M})^2 \, dV \tag{2.4}$$

  where M_s is the saturation magnetization, A is the exchange constant and $\mathbf{M}$ the magnetization.

- The demagnetization energy, also referred to as magnetostatic or dipolar energy, is caused by demagnetizing fields within and stray fields outside the magnetic material. It is given by [20]:

  $$E_{demag} = -\frac{\mu_0}{2} \int_{space} \mathbf{H_{demag}} \cdot \mathbf{M}\, dV \tag{2.5}$$

  with the vacuum permeability μ_0. This is also referred to as shape anisotropy, which is an extrinsic anisotropy strongly influenced by the form of the magnet. The minimisation of this non-local demagnetization energy is the reason why magnetic materials break into domains [15]. This is depicted in Figure 2.2b.

- The anisotropy energy consists of different contributions. The magnetocrystalline anisotropy energy favours the alignment of the magnetization along certain crystal axes, which means that the system can have certain preferred easy axes and unfavourable hard axes. For a uniaxial anisotropy this is given by [20]:

  $$E_{ani,u} = \int_{sample} K_{u1} \sin^2\theta + K_{u2} \sin^4\theta\, dV \tag{2.6}$$

  where K_{u1} and K_{u2} are anisotropy constants and θ is the angle between the anisotropy axis and the magnetization. This anisotropy energy is intrinsic to a material. Besides the previously mentioned shape anisotropy, there can also be induced anisotropies that come from external influences such as strain (see Fig. 2.2c).

- There is also the Zeeman energy if the material is subject to an external magnetic field $\mathbf{H_{ext}}$. In this case, the magnetic moments will preferably align along the direction of the magnetic field (Fig. 2.2d). This is given by [20]:

  $$E_{Zeeman} = -\mu_0 \int_{sample} \mathbf{M} \cdot \mathbf{H_{ext}}\, dV \tag{2.7}$$

Thin films, which are mainly discussed in this thesis, typically exhibit a magnetization aligned in the film plane due to the demagnetization energy, even though it is possible to rotate the magnetization out-of-plane by introducing additional anisotropies. Whereas laterally confined magnetic elements with sizes below approximately 1 µm are typically in a single domain state, larger elements can break into domains to minimise their total energy as shown in Fig. 2.2b, c and d. Within a domain, the magnetic moments are aligned parallel. The domains are separated by localised domain walls, in which the magnetization continuously rotates from one configuration to the other. The magnetization configuration in Fig. 2.2b is called a Landau pattern, where there is an in-plane

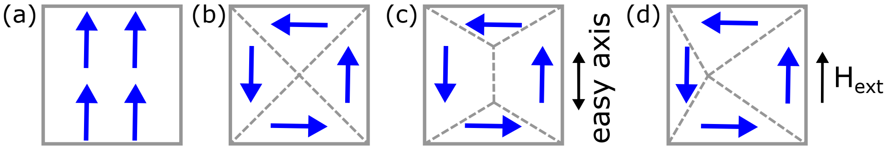

Figure 2.2: Schematics of the effects of different energy contributions on the magnetic moments (blue arrows) in a ferromagnet. a) The exchange energy favours parallel alignment of the magnetic moments. b) The shape anisotropy leads to the formation of domains. c) Influence of an easy-axis anisotropy that enlarges domains with magnetization along the axis. d) The Zeeman energy from an external magnetic field $\mathbf{H}_{\mathbf{ext}}$ causes expansion of the domain where the magnetic moments align with $\mathbf{H}_{\mathbf{ext}}$.

flux-closure with a central core pointing perpendicular to the plane (not shown) [21, 22]. It is topologically equivalent to a magnetic vortex, which has a continuous in-plane flux-closure of the magnetization and is typically found in circularly shaped patterns [23].

The micromagnetic approximation can be used to find the equilibrium configuration of a system and, as discussed in the following, to describe dynamic magnetic processes.

2.3 Magnetization Dynamics

If the magnetization $\mathbf{M}$ is not aligned with the effective magnetic field $\mathbf{H}_{\mathbf{eff}}$, which contains all contributions from the previously listed energy terms, there will be a torque exerted on $\mathbf{M}$ that leads to a precession of the magnetization around $\mathbf{H}_{\mathbf{eff}}$. This precession can be described by the equation proposed by Landau and Lifshitz [24]:

$$\frac{\mathrm{d}\mathbf{M}}{\mathrm{d}t} = -\gamma(\mathbf{M} \times \mathbf{H}_{\mathbf{eff}}) \tag{2.8}$$

where γ is the electron gyromagnetic ratio. In reality, such a precession is damped until the magnetization aligns with the effective magnetic field. This damping can be added to equation 2.8 transforming it into the so-called Landau-Lifshitz-Gilbert (LLG) equation:

$$\frac{\mathrm{d}\mathbf{M}}{\mathrm{d}t} = -\gamma(\mathbf{M} \times \mathbf{H}_{\mathbf{eff}}) + \frac{\alpha}{M_s}\left(\mathbf{M} \times \frac{\mathrm{d}\mathbf{M}}{\mathrm{d}t}\right) \tag{2.9}$$

where α is a damping constant. These equations show that external magnetic fields can be used to induce dynamics in a magnetic material.

In addition, spin-polarised currents can induce dynamics in a system by exerting a torque on the magnetization [25–27]. Terms from such spin torques can be added to the LLG equation, but are not relevant for the work presented in this thesis.

2.3.1 Micromagnetic Simulations

The LLG equation can be solved numerically, which allows for the simulation of the magnetic state of a material as well as of its dynamic evolution. Various software packages exist to perform such micromagnetic simulations. For the simulations shown in this thesis, the finite-differences MuMax3 framework is used [28]. In this method, the magnetic sample is divided into orthorombic cells where each cell has a magnetic moment pointing in the direction of the corresponding average magnetization. In order to reproduce all magnetic features, the cell sizes should be sufficiently small. Additionally, too large angles of the magnetization between neighbouring cells can lead to imprecise results as the contribution of the exchange interaction will be underestimated. Therefore, the cell size should be smaller than the exchange length of the system[29]

$$l_{ex} = \sqrt{\frac{2A}{\mu_0 M_s^2}}. \tag{2.10}$$

2.4 Spin Waves

Spin waves are collective excitations of ordered spin systems. In the micromagnetic framework, they can be visualised as the magnetic moments precessing with a spatially periodic phase shift to form a wave with a wavelength λ as shown in Fig. 2.3, propagating in the direction of $\mathbf{e_k}$. The quanta of spin waves are called magnons and follow Bose-Einstein statistics [14]. Spin waves can be found in ferro-, ferri- and antiferromagnets. This section introduces the fundamental properties of such spin waves in different materials and gives an overview of experimental methods to excite and detect them.

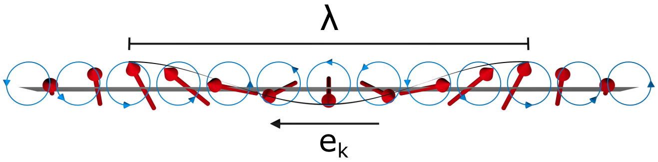

Figure 2.3: Schematics of a spin wave with wavelength λ. Magnetic moments (red) precess at their locations and form a wave propagating along $\mathbf{e_k}$. Adapted from [30]. Published under CC BY 4.0.

2.4.1 Dispersion Relation

The spin-wave dispersion relation is the fundamental relation between the frequency f and the wavelength λ of a spin wave. Often it is expressed in terms of the angular frequency $\omega = 2\pi f$ and the wavevector $k = \frac{2\pi}{\lambda}$ as $\omega = \omega(k)$. From the dispersion relation, phase and group velocities can be directly calculated as $v_p = \frac{\omega}{k}$ and $v_g = \frac{\mathrm{d}\omega}{\mathrm{d}k}$, respectively.

Different energies govern the behaviour of the spin waves at different ranges of the dispersion relation: for spin waves with a short wavelengths on the order of the exchange length, the exchange interaction plays the dominant role. For long wavelengths, the dispersion is governed by magnetostatics. For spin waves in the intermediate regime, both interactions have to be considered and the spin waves are referred to as dipole-exchange waves.

In the short-wavelength, exchange-dominated dispersion part in ferromagnets all modes exhibit an $\omega \sim k^2$ dependence, while for ferromagnetic thin films in the magnetostatic regime, i.e. the long wavelength limit, three modes with fundamentally different dispersion relations exist (see Fig. 2.4). These depend on the orientation of the magnetization of the film $\mathbf{M}$ and the wavevector of the spin waves $\mathbf{k}$ defined as follows:

- forward volume (FV) mode for $\mathbf{M}$ perpendicular to the film plane and $\mathbf{k}$ in the film plane
- backward volume (BV) mode for $\mathbf{M}$ lying in the film plane and $\mathbf{k}$ collinear to $\mathbf{M}$
- Damon-Eshbach (DE) mode for $\mathbf{M}$ and $\mathbf{k}$ lying in the film plane and $\mathbf{k}$ being perpendicular to $\mathbf{M}$ [31]

These corresponding dispersion relations can be calculated analytically. In the thin film dipole-exchange region, where the spin waves discussed in this thesis are located, the dispersion relations can be analytically calculated for the nth mode from [32]:

$$\omega = \mu_0 \gamma \sqrt{\left(H + \frac{2A}{\mu_0 M} k^2\right)\left(H + \frac{2A}{\mu_0 M} k^2 + M F_{nn}\right)} \tag{2.11}$$

with

$$F_{nn} = P_{nn} + \sin^2\theta \left(1 - P_{nn}\left(1 + \cos^2\varphi\right) + P_{nn}\left(1 - P_{nn}\right)\sin^2\varphi \left(\frac{M}{H + \frac{2A}{\mu_0 M} k^2}\right)\right). \tag{2.12}$$

Here, θ is the angle between the surface normal and $\mathbf{M}$, while φ is the angle between $\mathbf{M}$ and $\mathbf{k}$. The matrix element P_{nn} can be calculated analytically. For the simplest case of the fundamental zeroth-order mode with unpinned surface spins

$$P_{00} = 1 - \frac{1 - e^{-kd}}{kd} \tag{2.13}$$

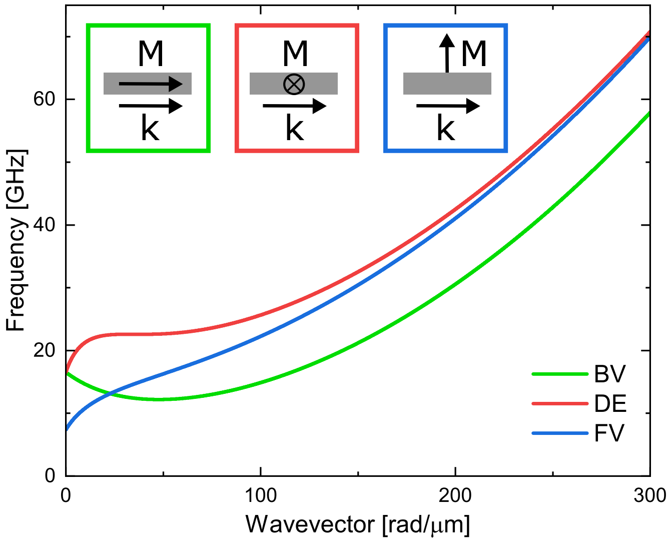

Figure 2.4: Dispersion relation of the three different modes, calculated for a 70 nm NiFe film in an external magnetic field: backward volume (BV) mode (green), forward volume (FV) mode (blue) and Damon-Eshbach (DE) mode (red). All modes exhibit a $\omega \sim k^2$ dependence in the exchange regime. The inset depicts the different orientations between $\mathbf{M}$ and $\mathbf{k}$ for the different modes.

where d is the thickness of the film [33]. These equations require the magnetic field to be applied in the direction of the magnetization and do not take into account anisotropy. A description taking into account arbitrary magnetic field directions and crystalline anisotropy is possible but more involved [34].

In contrast to the two volume modes, the Damon-Eshbach mode is a surface mode, meaning its precession amplitude spatially decays over the film thickness. For in-plane magnetized films, both the backward volume and Damon-Eshbach mode can be excited. The group velocity, which is the velocity relevant for information transfer, can have opposite sign with respect to the phase velocity for the backward volume mode in the $\mathbf{k}$ range before the dispersion minimum, but is always positive for the Damon-Eshbach mode. This makes the Damon-Eshbach mode the one typically considered for technological applications based on in-plane magnetized films.

In addition to the previously described fundamental zeroth-order mode, higher order modes exist as well. Whereas the fundamental mode shows a uniform precession over the film thickness, higher order modes exhibit nodes across the film thickness. Here, the number of nodes n typically corresponds to the nth order. Furthermore, hybridisation may occur between these different modes, which means that a mode can adapt characteristics of other modes. Such hybridisation leads to avoided crossings at mode interceptions and changes of mode profiles for larger wavevectors [9].

In coupled ferromagnetic layers with parallel magnetizations, the spin waves in the individual layers can precess in phase or with a phase shift of 180°, which are referred to as acoustic and optical modes, respectively. In antiferromagnetically coupled layers, referred to as synthetic antiferromagnets (SAFs) or synthetic ferrimagnets (SFis), the localisation of the spin-wave amplitude at one side of each layer can lead to a concentration of the coupled spin-wave amplitude either at the interface or at the two opposite surfaces. Due to the chirality of precession, this leads to a non-reciprocity of the occurring spin waves, which means that the dispersion relation is not symmetric with respect to $k = 0$ and that waves propagating in opposite directions have different wavelengths at the same frequency leading to a so-called fast and slow branch of the dispersion. The distinction whether the slow branch corresponds to $k < 0$ or $k > 0$ is determined by the relative magnetization orientation of the ferromagnetic layers with respect to k.

Antiferromagnets typically exhibit precession frequencies that are much higher than in ferromagnets, which is a result of the strong exchange field (H_{ex}) that couples the two sublattices, while in ferromagnets the dynamics is governed by the anisotropy fields (H_{ani}) [35]. Any canting of the sublattices against each other as in optical modes, therefore, involves the exchange field. This means that in antiferromagnets, even the dynamics of infinite-wavelength spin waves, the antiferromagnetic resonance (AFMR), are typically enhanced by a factor of $\sqrt{H_{ex}/H_{ani}}$ compared to the ferromagnetic resonance (FMR) [35]. In general, complex spin-wave modes can exist in antiferromagnets, which depend on their structures and properties [16]. Even simple antiferromagnetic structures, such as easy-axis and easy-plane AFMs, show diverse precessional dynamics. For an easy-axis antiferromagnet, the two antiferromagnetically coupled sublattices can only precess in opposite directions, leading to an overall precession in the same circular sense. This is due to the anisotropy field, which points in opposite directions for the sublattices. This is in contrast to an easy-plane AFM, where the additional anisotropy leads to a precession in overall opposite directions [36]. The application of an external magnetic field can influence the spin-wave modes further depending on the field magnitude and direction, i.e. whether it is applied along an easy axis or perpendicular to it. However, these fields typically need to be on the order of several tesla to induce a spin-flop transition, which drastically changes the modes [36]. In general, antiferromagnetic spin-wave dispersions exhibit a linear $\omega \sim k$ dependence instead of a quadratic one as for ferromagnets [14]. The reason for this lies in the rotational invariance and spontaneous magnetization in a ferromagnet, which lead to the occurrence of only one magnon as a Goldstone bososn instead of two magnons in antiferromagnets [37, 38].

2.4.2 Generation and Detection of Spin Waves

There are different methods to excite spin waves in a spatially controlled way. A widespread technique to achieve this utilises the inhomogeneous magnetic Oersted field of a patterned antenna, through which an AC current flows. These antennas, in the form of micrometre-sized striplines or coils, are patterned on top of continuous films and provide both in-plane and out-of-plane magnetic fields. The use of such antennas allows for a full control over the resulting spin-wave frequency and phase with the driving current. There is a lower limit to wavelengths that can be excited by this method, which is mostly determined by the size of the magnetic field inhomogeneity and therefore the antenna size. The fabrication of nanoscale antennas and the matching of their impedance to transmission lines can be difficult [39]. The samples in chapters 6 and 7 utilise such patterned antennas to excite spin waves.

A different way to excite spin waves is to use spin torques, where spin-polarised-charge currents create a torque on the magnetization. Both spin-orbit [40–42] and spin-transfer torques [43, 44] can be used. These techniques have the advantage that they do not rely on magnetic fields, making them promising for the controlled excitation of spin waves in antiferromagnets. The strength of the torque scales with the current per unit area while additionally being inversely proportional to the layer thickness for spin-orbit torques. Therefore, it mainly has an influence in thin films and, in particular, in nanostructures [16].

In order to overome size restrictions imposed by impedance-matching antennas, different excitation concepts were developed. In a grating coupler, arrays of nanostructures are patterened below an antenna to generate spin waves with short wavelengths of less than 100 nm [45, 46]. In graded-index magnonics, a variation of the magnetic landscape of a sample can not only be used to guide spin waves, but also to induce a wavelength reduction in magnetically confined regions by a so-called Schlömann mechanism [47, 48]. A similar way to overcome the size restrictions of patterned structures and to generate short-wavelength spin wave, is to use nanometre-sized topological defects as spin-wave emitters. This has been demonstrated, for example, for magnetic vortex cores [9, 49–53] and domain walls [54, 55]. Here, the vortex cores perform a small oscillating motion when they are excited by an rf magnetic field. The motion of the cores leads to strongly enhanced local effective magnetic fields and, hence, torques that couple to the spin-wave continuum and result in the emission of high-amplitude, short wavelength spin waves [9]. This method to excite spin waves is utilised in Chapters 4 and 5.

There is a variety of different measurement techniques available to detect spin waves, which have different characteristics. Inelastic neutron scattering and resonant inelastic x-ray scattering are particularly suited to detect incoherent short wavelength spin waves at high frequencies in the deep exchange regime [15]. All-electrical detection set-ups can be either wavevector independent [56] or selective [57]. Magneto-optical techniques, such as time-resolved magneto-optical Kerr effect measurements (TR-MOKE), allow to measure coherent spin waves in the time domain [58]. Brillouin light scattering (BLS) is sensitive to the magnetic excitations within a sample with wavevectors similar to the wavevector of the used probing laser and allows for the detection of both coherent and incoherent spin waves [59]. Ferromagnetic resonance (FMR) experiments allow the measurement of $k = 0$ spin waves, i.e. spin waves with an infinite wavelength, where all magnetic moments precess in phase [16].

In this thesis, synchrotron-based time-resolved scanning transmission x-ray microscopy is used to image coherent spin waves in a phase-resolved way. It has the advantage of a higher spatial resolution when compared to optical methods, so allowing the imaging of spin waves with wavelength below 100 nm, and covering a wide frequency range. Furthermore, it allows the use of two different magnetic dichroism effects, providing sensitivity to the magnetization in different materials, and the distinction between different elements as well as sublattices. A detailed description is given in Section 3.2.

3 Experimental Methods

In this chapter the sample fabrication via electron beam lithography is introduced, which provides a method for the patterning of structures in the micro- and nanometre range. After this, the main measurement method, scanning transmission x-ray microscopy (STXM) is explained in detail, together with the generation of x-rays at synchrotrons as well as the methods used to perform magnetic and time-resolved measurements. Finally, a technique to fabricate soft x-ray transparent windows into bulk samples and substrates, which was developed during the course of this project, is presented.

3.1 Sample Fabrication with Electron Beam Lithography

In order to define structures with sizes in the micrometre range and below, electron beam lithography (EBL) is used. Here, parts of an electron sensitive resist are exposed with a focused electron beam to change its structure and, hence, solubility in a developer. There are positive resists, where the electron-beam exposed areas become soluble in a developer and negative resists, where the electron beam modifies the exposed part to make it insoluble. Throughout this thesis, lift-off lithographical patterning, achieved by means of a positive resist, was most commonly used. Therefore, in the next paragraphs, this process will be described in detail. Different fabrication methods and sample specific details will be given in the respective chapters.

An EBL process with lift-off involves several steps that are schematically shown in figure 3.1. The first step is the spin-coating of a resist onto a substrate. Because the measurements are in an x-ray transmission geometry, x-ray transparent Si_3N_4 membranes were used as substrates during this project whenever possible. They consist of a thin Si_3N_4 layer with a thickness on the order of 100 nm on a Si frame. For the patterning performed in this work, a bilayer of the electron beam resists methyl methacrylate(MMA)/poly(methyl methacrylate)(PMMA) was used. The advantage of using a resist with a lower molecular weight as an underlayer facilitates the lift-of process. This is likely to be due to the formation of an undercut in the resist so that the material deposited on top is discontinuous. The thickness of a given resist is primarily determined by the rotation velocity of the spin coater and is adapted depending on the required thickness of the film to deposit, where the lift-off of thicker films requires thicker resists. After spincoating, the sample is baked on a hotplate to remove the remaining solvent and to harden the resist.

The sample is then transferred to an electron beam writer, where the microstructures are exposed in the resist. The exposed part of the resist becomes soluble in a developer because the focused electron beam breaks up the polymer chains. The feature size that can be achieved by this technique is below 10 nm and depends on various parameters, e.g. aperture sizes and the used resist. The actual beam size additionally scales with the current. Smaller currents lead to a smaller spot size, meaning more smaller feature sizes but longer exposure times. Therefore, low currents were used for defining the magnetic microstructures, whereas higher currents were employed for the larger structures, such as e.g. the coplanar waveguides, to reduce the overall exposure time. Another important parameter is the exposure dose, i.e. the charge deposited per unit area. It needs to be adjusted for different resist thicknesses and substrate materials.

After the exposure, the sample is developed for 60 s to 90 s in a methyl isobutyl ketone:isopropyl alcohol (MIBK:IPA) mixture (1:3 volume ratio) which removes the soluble resist in the exposed areas. Afterwards the sample is rinsed in IPA for 60 s.

Then the films are deposited onto the patterned resist. For the deposition of the films several different methods e.g. sputter deposition, thermal or electron beam evaporation can be employed, depending on the individual requirements. The used deposition techniques are described in more detail in Subsection 3.1.1.

Finally, the sample is immersed in acetone for several hours for lift-off. This removes the remaining resist with the material on top of it, leaving only the desired structures on the substrate.

Often more than one such lithography process has to be performed on a single sample. In this case, the first step is the fabrication of alignment markers that will later be employed for the alignment of the subsequent layers. They consist of arrays of Au squares that give good contrast for the electron beam. Afterwards, one or more steps can be performed for the definition of the actual magnetic structures. Usually, the last fabrication step consists of patterning a conducting micro-stripline.

3.1.1 Thin Film Deposition Methods

The deposition of the thin films for the samples in this thesis was primarily carried out with the physical vapour deposition techniques, magnetron sputter deposition and thermal evaporation, which are well suited for thin films with a thickness of below 1 µm.

In magnetron sputtering, a target of the desired material is kept in ultra high vacuum (UHV). Then a working gas, usually Ar, is let into the chamber and a negative potential

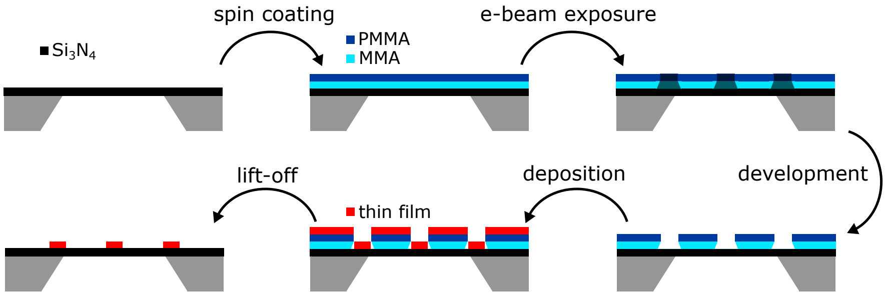

Figure 3.1: Schematics detailing the processing steps of EBL with lift-off for a bilayer of positive resists on a Si_3N_4 membrane.

is applied to the target, which leads to a plasma of the working gas ions. These ions are accelerated towards the target and sputter atoms off the material, which can then condense on the sample forming a thin film. Additionally, a magnetic field is applied to the target, which forces the charged particles in the plasma to spiral around magnetic field lines, increasing the ionisation probability for the working gas, making the ionisation more efficient. The deposition rate is typically calibrated before the actual film deposition by measuring the thickness of a calibration layer. Due to a UHV base pressure, the use of high-purity materials as well as being a process that can keep the stoichiometry of the target material, sputtering was employed for the fabrication of the magnetic materials during this project.

Thermal evaporation is based on passing a high current through a crucible, typically made out of W, in which the material to deposit is placed. This current heats up the material so that it either melts and evaporates or sublimates and redeposits onto the sample. The thickness of the deposited material is measured using a quartz balance. Due to the poorer quality of the vacuum in the set-up available, this method was primarily used for the deposition of markers and striplines during this project.

The Ga-doped YIG films in Chapter 6 were fabricated by INNOVENT Technologieentwicklung Jena using liquid phase epitaxy (LPE) on GGG substrates [60]. LPE uses an oversaturated melt containing the desired materials for the thin film, into which a substrate is dipped. Depending on parameters such as temperature, concentration as well as substrate rotation speed, a thin film with the desired composition will then crystallise on the substrate. This method has been established for the growth of high-quality YIG films with low magnetic damping [61].

3.2 Scanning Transmission X-Ray Microscopy

To directly image the local magnetic orientation and its changes over time in the patterned microstructures and thin films, an element specific technique that has a high spatial and temporal resolution and is at the same time not surface sensitive and non-invasive is required. These requirements are uniquely fulfilled by scanning transmission x-ray microscopy (STXM). To gain a maximum performance, STXM experiments are typically based at synchrotron sources. Therefore, the basics of x-ray generation at synchrotrons are explained first, followed by an introduction to the magnetic dichroism effects that are used for magnetic contrast. Afterwards the set-up of a STXM is explained in detail before the methods to perform time-resolved measurements are explained.

3.2.1 Synchrotron X-Rays

The term x-rays typically refers to electromagnetic radiation with a wavelength of approximately 10 nm to 10 pm, which corresponds to a photon energy of approximately 100 eV to 100 keV. Due to their possibility to penetrate matter, x-rays are used in various areas of research e.g. medicine, biology, and physics [62].

In particular, x-rays produced at synchrotrons are useful because of their high brilliance, tunable energy and variable polarisation. At such a synchrotron light source, electrons circulate at relativistic energies in a closed orbit in a storage ring. An electron storage ring consists of straight sections that are connected by curved parts, in which the electrons are deflected by dipolar bending magnets. When they are deflected, relativistic electrons emit x-rays in the form of bremsstrahlung along the forward direction, similar to a searchlight [62]. However, at modern synchrotrons, x-rays are not only generated at bending magnets. It is additionally possible to use arrays of alternatingly oriented strong permanent magnets to force the electrons on a slalom path in a straight section of the storage ring. Then radiation is generated at each of the slalom turns, which interferes to create a coherent x-ray beam of higher intensity than at bending magnets. Such a set-up is called an undulator.

A necessity for magnetic measurements is that the x-rays are circularly polarised. At bending magnets, this is achieved because the electrons oscillate in the plane of their orbit, leading to a linear horizontal polarisation of the x-rays. Out of this plane, the electron path appears to be elliptical. The thus created angular momentum is transferred to the emitted x-rays, which leads to opposing circular polarisation fractions above and below the central beam [62]. At modern undulators, which typically consist of four arrays of permanent magnets, an elliptical path can be achieved by shifting these arrays with respect to each other to introduce a vertical component into the electron path. This also means that, in addition to linear horizontal and circular polarisations, linear vertically polarised x-rays can be generated [62, 63].

The x-rays generated by the electrons in the storage ring are then guided in vacuum by mirrors and a slit system towards the experiment. To select x-rays with a defined energy, a monochromator, which is a diffractive single or double grating, is used.

3.2.2 X-Ray Magnetic Circular and Linear Dichroism

X-ray magnetic circular dichroism (XMCD) refers to a magnetization dependent absorption of circularly polarised x-rays near the absorption edges of a material [64]. As previously described, circularly polarised x-rays carry an angular momentum that is transferred to a bound electron upon absorption. Circularly left polarised photons carry an angular momentum of -1 in units of $\hbar$ in the direction of propagation and are therefore also referred to as negatively polarised, while right polarised photons have a momentum of $+1$ and are called positively polarised [65].

If such a polarised photon excites an electron transition from a core state, only certain transitions are allowed for which selection rules apply. The dipole selection rule for the orbital quantum number l states that $\Delta l = \pm 1$. Because the photon is annihilated in the absorption process, it has to transfer its angular moment to the system due to the conservation of angular momentum. This leads to a change of $\Delta m = +1$ for positively and $\Delta m = -1$ for negatively polarised x-rays in the magnetic quantum number m [65]. Furthermore, because spin is conserved, one can assume that spin flips are forbidden [62]. One now considers electrons in a spin-orbit split core level, e.g. $2p_{1/2}$ and $2p_{3/2}$ and their transition to the d level. This corresponds to the L_2 and L_3 edges, which are most commonly probed for magnetic transition elements and their oxides. Summing up all possible excitations, taking into account their probabilities, a positively polarised photon will excite 75% $\downarrow$ (spin down) and 25% $\uparrow$ (spin up) electrons from the $2p_{1/2}$ level. For the $2p_{3/2}$ level, the distribution is inverted with 37.5% $\downarrow$ and 62.5% $\uparrow$. For a negatively polarised photon, the probabilities invert [66]. However, these transition probabilities do not yet take into account how many final states are available for the excited electrons to occupy at the d level according to Fermi's Golden Rule. For a non-magnetic material, the number of unoccupied states is the same for both polarisations (see Fig. 3.2a). However, for a ferromagnetic material, the number of occupied and unoccupied states differs for the two spin polarisations at the Fermi level due to the spin-split band structure as shown in Figure 3.2b [66]. Therefore, the transition probability is higher for electrons with the polarisation that offers more unoccupied states. This difference gives rise to an XMCD signal [66].

This means that the XMCD effect depends on the relative orientation of the wavevector of the incoming photon and the magnetization vector and is therefore $\propto \mathbf{k} \cdot \mathbf{M}$.

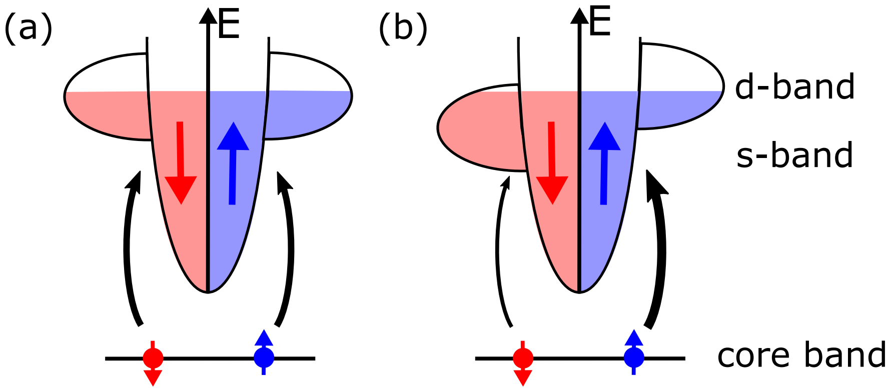

Figure 3.2: Schematic of the XMCD effect. (a) For a non-magnetic material the spin-up and spin-down states are equally occupied leading to an equal transition probability for the excited electrons. (b) In a ferromagnetic material, the difference in occupation for the spin-split bands results in different transition probabilities for the ↑ and ↓ electrons.

Hence, the effect is strongest for collinear orientation between magnetization and polarisation, and disappears when they are orthogonal [64, 67].

While it is possible to extract quantitative information on the orbital and spin moments by applying the so-called XMCD sum rules on energy absorption spectra [68–70], XMCD in this thesis is used as a qualitative contrast mechanism for imaging. For this purpose, the energy of the x-rays is usually tuned to give the strongest magnetic contrast at the absorption edge.

Another dichroic effect that can be employed for the imaging of magnetic configurations is the x-ray magnetic linear dichroism (XMLD)[71]. It is based on a distortion of the charge density, which is induced by the magnetic state via spin-orbit coupling [62]. This distortion is probed by linearly polarised x-rays. However, distortions of the charge density can be caused by effects other than magnetism, which can make the interpretation of XMLD difficult.

The XMLD effect exhibits a $\cos^2(\theta)$ dependence between the linear polarization of the x-rays and the spin axis of the sample. This means that it is sensitive to the orientation of the spin axis and not the direction of the magnetization [62]. Here the measurement of the spin configuration in antiferromagnetic materials is enabled, which is not accessible by XMCD. However, ferromagnetic materials can in principle be measured using XMLD as well [72].

3.2.3 STXM Set-up

In STXM, the spatially resolved transmission of x-rays through a sample is measured. The set-up is schematically shown in Figure 3.3. Monochromatic, soft x-rays are focused onto a spot of around 20 nm in diameter on the sample using a diffractive Fresnel zone plate (FZP), which consists of alternating transparent and absorbing concentric rings. The width of the outermost ring determines the ultimately achievable width of the focal spot. A beamstop in the centre of the FZP blocks the direct beam. An order selecting aperture (OSA), which is a pinhole between the FZP and the sample, aditionally blocks the direct beam (zeroth order) as well as the higher diffraction orders of the light, which have a different focal point. Downstream from the sample, the transmitted x-rays are detected with a point detector, which is usually an avalanche photodiode (APD). To form an image, the sample is then raster scanned through the beam with a piezoelectric stage [73]. The samples are typically mounted with the surface normal aligned with the photon beam. For magnetic investigations, this means that the XMCD effect is sensitive to the out-of-plane component of the magnetization. To probe in-plane magnetic contrast, the samples are tilted by 30°. As STXM is a photon-in/photon-out technique and no charged particles are detected, it does not require UHV conditions and it is straightforward to apply magnetic fields or electric currents to the sample.

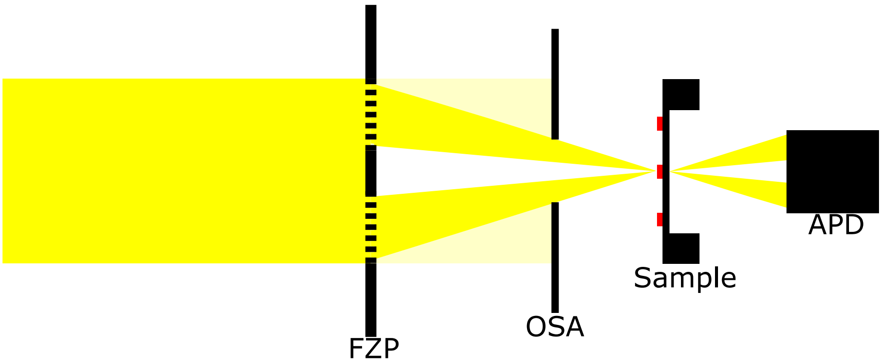

Figure 3.3: Schematic of a STXM: the incoming monochromatic x-rays are focused on the sample using a Fresnel zone plate (FZP) and an order selecting aperture (OSA) to block the direct beam and higher diffraction orders. The sample is then raster scanned through the photon beam to obtain the image. The transmitted x-rays are recorded with an avalanche photodiode (APD) point detector behind the sample.

The STXM experiments during this project were performed at the endstations PolLux at the SLS and Maxymus at BESSY II. In both set-ups, in-plane and out-of-plane magnetic fields of up to 250 mT can be applied to the sample [74]. At Maxymus additionally a He cryostat and heater was utilised, which allows for measurements in a temperature range between 30 K and 360 K.

3.2.4 Time-Resolved Measurements

The measurement of magnetization dynamics, such as spin waves, is realised in a pump-probe scheme. Here, the sample is pumped using an electric current to generate a magnetic field in e.g. a stripline, while the x-rays are used as a probing signal. This is possible due to the inherent time structure of the electrons in the storage ring, which travel in well-separated regularly spaced bunches. The time between these bunches is defined by the frequency of the RF cavities in the electron storage ring, which for the SLS and BESSY II is approximately 500 MHz and leads to a time difference of 2 ns between two consecutive bunches. This means that x-ray flashes reach the sample every 2 ns with a transmitted flux of typically not more than a single photon per flash. As described in Section 3.2.3, the photons are then recorded by an APD and the result, whether a photon was detected or not, is routed to a specific counter of a register set by a field-programmable gate array (FPGA) in real time. To perform time-resolved measurements, these probing flashes have to be synchronised to a pump signal, which is the electrical excitation applied to excite the sample. For this purpose, the applied frequencies have to be commensurate with the time structure of the synchrotron. For an RF signal this means that they have to fulfil the relation

$$f = \frac{500\,\mathrm{MHz} \cdot M}{N}, \tag{3.1}$$

where N is the number of channels and M is an integer chosen to match the desired frequency with N and M coprime. The number of channels determines into how many counters the photons are routed and equals the number of frames the time-resolved movie has [75]. Typical values for N used here are between 7 and 23. This acquisition scheme means that the recorded processes must be fully reproducible. Typically, time-resolved images are not taken as dichroic images but only with a single polarisation and then shown in a normalised view. To form such a set of normalised images, each image of the corresponding set is divided by the time average of all images. This highlights the temporal changes of the magnetization while the static contrast is removed.

In this pump-probe set-up the detected photons are assigned to a certain bunch but their exact time is not measured. Therefore, it is assumed that the photon is emitted at the centre of the electron bunch, which limits the time resolution of the x-ray flashes. In a standard multibunch filling pattern as currently offered by SLS or BESSY II, the bunch width FWHM is in between 50 ps to 70 ps. With an additional decrease in time resolution due to a phase shift of the electron bunches, this limits the measurements to frequencies of 5 GHz to 10 GHz [76]. Therefore, to achieve a better time resolution, shorter electron bunches are needed, which are provided at certain synchrotrons in a so-called low-α optics mode. At the BESSY II synchrotron, a low-α multibunch filling pattern with an x-ray flash FWHM down to 16 ps is offered, which allows for probing frequencies of up to 40 GHz.

Time-of-Arrival Detection

Another possibility to increase the time resolution is to directly measure the arrival time of a photon instead of assuming its generation at the centre of the electron bunch. Such a setup relies on a fast time-to-digital converter (e.g. QuTAG, from qutools GmbH) that measures the time at which an input signal, which corresponds to the instant at which the voltage pulse is generated by the APD, crosses a defined threshold with a sub-10 ps precision. In practice, a constant fraction discrimination is used, which means that, because these pulses can have different heights, not only the rising but also the falling edge is taken into account. This data is timestamped and can then be binned and analysed further. Another advantage of this detection scheme is that, in principle, no synchronisation with the synchrotron clock is needed. This means that the restrictions of the frequency selection do not apply any more and arbitrary frequencies can be chosen. In test measurements of the standard SLS multibunch filling pattern, a time resolution of 20 ps to 30 ps was achieved using the standard multibunch pattern with a bunch width of 70 ps [76].

3.3 Xe Plasma Focused Ion Beam Milling for Obtaining Soft X-Ray Transparent Sample Windows

The content of this section is based on the publication Mayr et al. Crystals 11(5), p. 546 (2021) [77]. My personal contribution to this article is developing the Xe PFIB window milling process and associated mechanical grinding step, participating in the STXM measurements and writing the manuscript with input from the other authors.

A prerequisite for the previously described STXM experiments is to have samples that are transparent in the soft x-ray regime. This is usually achieved by growing thin films and structures on $\approx 100\,\mathrm{nm}$ thick Si_3N_4 membranes as previously described in Section 3.1. However, for materials that need to be grown on specific substrates or for bulk single crystals, this is not possible and different approaches exist: For a few specific material and sample structures, selective chemical etching can be used [78, 79]. Another option is to cut out a lamella with a focused ion beam (FIB) and place it on an x-ray transparent membrane [33, 80].

An approach that allows the study of continuous films is based on a combination of mechanical grinding and Ga FIB milling to remove material from the back side of the sample in order to create x-ray transparent windows [10, 81–85]. However, this technique is limited by the slow milling speed of the Ga FIB and therefore requires the sample to have a thickness in the low micrometre range prior to the FIB milling. This is typically achieved by mechanical grinding of the full sample to a thickness of approximately 50 µm to 100 µm followed by dimple grinding of a smaller sample area to a thickness of below 20 µm. In this emerging dimple, the remaining material is then removed with the Ga FIB until soft x-ray transparency is reached, which corresponds to a thickness on the order of a few hundred nanometres.

An advancement of this technique was developed and applied during the course of this project and is based on the use of a Xe Plasma FIB (PFIB), which has a more than 10 times higher milling rate compared to the Ga FIB [86]. This faster milling facilitates the overall window fabrication process, which is described in the following and schematically shown in Figure 3.4.

Due to the high milling rate, the samples can have a thickness of up to approximately 100 µm prior to the PFIB processing step. This means that no dimple grinding step is necessary. For many common materials, substrates are commercially available with such thicknesses and can be directly used. Where this is is not possible, the samples have to be mechanically thinned. For this, the sample is attached with a thermoplastic polymer on a glass support with the film facing the glass. The back of the substrate is then lapped with a 12 µm Al_2O_3 abrasive. To reduce the surface roughness, the sample is then polished with a suspension containing 6 µm diamonds and a Microtex polishing cloth. To achieve a higher surface quality, an additional polishing step with a suspension containing 3 µm diamonds and a silk polishing cloth can be employed. Afterwards, the sample is immersed in acetone to remove it from the glass support.

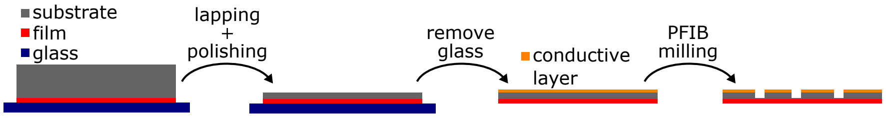

Figure 3.4: Schematics of the window milling steps using a Xe PFIB. Adapted from [77]. Published under CC BY 4.0.

To reduce charging effects during the PFIB processing, a layer of conducting Cr with a thickness of approximately 10 nm is deposited onto non-conducting substrates prior to the PFIB milling. The PFIB processing itself is performed with a Tescan Fera3 Xe PFIB-SEM equipped with a high resolution scanning electron microscope (SEM) column and a high resolution plasma FIB (so called HR-iFIB) column. An acceleration voltage of 30 kV and currents of up to 1 µA for the Xe ions are used. Thus, it is possible to mill windows with areas extending to 100 µm × 100 µm. Figure 3.5 depicts SEM images of such windows, milled into $SrTiO_3$ (STO) (Fig. 3.5a) and $Gd_3Ga_5O_{12}$ (GGG) (Fig. 3.5b). Both images are taken with the secondary electron detector at an incident electron energy of 10 kV and a 55° tilt (with respect to the surface normal). This corresponds to the milling position as it provides normal incidence of the Xe^+ beam onto the sample. It can be seen that in both materials, the Xe PFIB milling results in a plane and smooth surface, which is essential to achieve final window thicknesses of below 1 µm. Here, it is beneficial that the current density distribution of the Xe PFIB beam has a wider maximum due to a larger emission area of the source when compared to the Ga FIB beam.

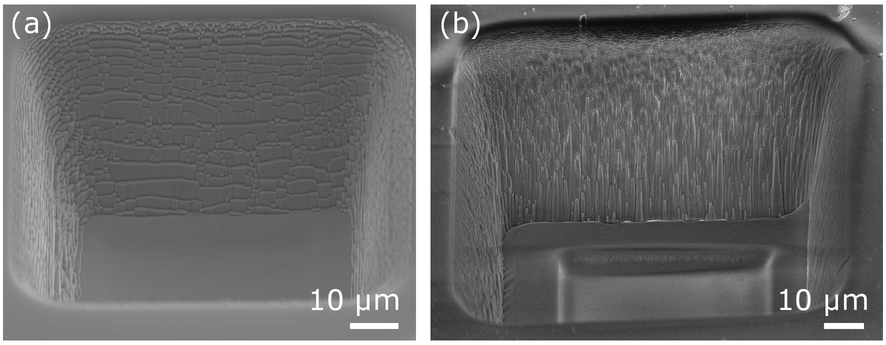

Figure 3.5: SEM images of windows milled into (a) STO and (b) GGG. (a) Adapted from [77]. Published under CC BY 4.0.

The most difficult challenge of the PFIB milling is to accurately stop at a thickness of below 1 µm. Additionally, it should be determined already during the milling process, i.e. before the sample is taken out of the PFIB, whether the milled window will be suitable for soft x-ray transmission measurements. To achieve this, the transparency for the electrons in the two beam PFIB-SEM system and for soft x-rays is correlated. For this, the samples need to be mounted in the PFIB without any material behind it, so the electrons can pass freely through it. Direct transmission measurements are not possible for geometric reasons. However, the brightness of the milled area, when imaging with the secondary electron detector of the SEM, directly relates to its thickness. This is because, in addition to secondary electrons from the top surface, electrons from the bottom surface can be extracted and reach the detector once the sample is thin enough for the primary electrons to pass through.

To demonstrate this correlation, several windows with slightly different depths were milled into a 50 µm thick STO substrate as shown in the SEM image at 30 kV in Fig. 3.6a. The bright halos around the windows are a result of charging where the conductive coating on the non-conductive substrate has been removed by the halo of the PFIB beam. For STO, the milling rate is determined to be approximately $0.25\,\mu m^3/nC$. This means that milling of one of these individual windows of 80 µm × 80 µm lateral size, using a 600 nA Xe^+ ion beam, takes less than 40 minutes. These SEM images were taken at normal incidence to the surface to be able to fully image the inside of the milled windows. After the milling, the transmission of 1 keV x-rays was measured through each window. By doing so, relative x-ray transmission rates are obtained, which range from 100 % (corresponding to a hole) to about 1 % for the thickest window.

In the following, we focus on two windows which appear bright and are indicated with the red and blue boxes in Fig. 3.6. The window in the red box transmits approximately 2.5 times more x-rays than the window in the blue box. While this difference is hard to infer from this SEM image at 30 kV, the correlation with the electron transparency becomes apparent for SEM images at lower electron energies. For a 20 kV acceleration voltage (Fig. 3.6b), a difference in brightness between the two windows is visible. This becomes even more distinct at a lower energy of 15 kV (Fig. 3.6c), where a bright-spot is seen for the red-framed window, whereas the blue-framed window is no longer transparent to the electrons.

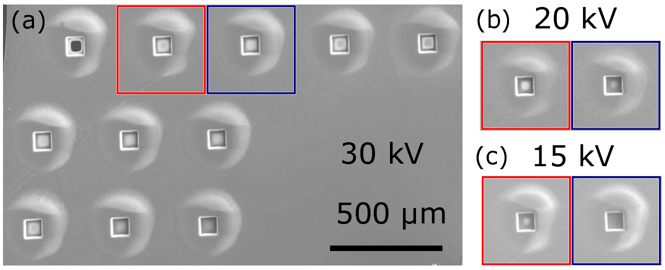

Figure 3.6: SEM images of windows with varying transparency in a 50 µm thick STO substrate at different electron acceleration voltages. (a) Overview of windows at 30 kV. The windows in the red and blue boxes are additionally shown for 20 kV (b) and 15 kV (c). Taken from [77]. Published under CC BY 4.0.

Although the correlation between electron and x-ray transparency cannot be directly generalized to other substrates and thin film systems, they serve as a guide and can be adapted to specific samples. This is demonstrated with of a second sample system whose investigation in reported in Chapter 6, namely a Ga-doped $Y_3Fe_5O_{12}$ (YIG) film of 150 nm thickness on a GGG bulk substrate. This sample was first lapped to a thickness of approximately 120 µm. Subsequently, a window was milled into the substrate using the Xe PFIB. The initial lateral size of the window was 100 µm × 100 µm, which was reduced to about 50 µm × 50 µm during the milling process. Starting with a larger than required window size reduces redeposition effects during the final milling steps on such thick substrates. An approximate milling rate of 0.3 μm^3/nC for GGG was found so that a window similar to the previously shown STO ones (80 µm × 80 µm size into a 50 µm thick substrate) requires approximately 30 minutes of milling time using a 600 nA

Xe$^+$ ion beam. The SEM image of the final window taken with the secondary electron detector at 10 kV is shown in Fig. 3.7a.

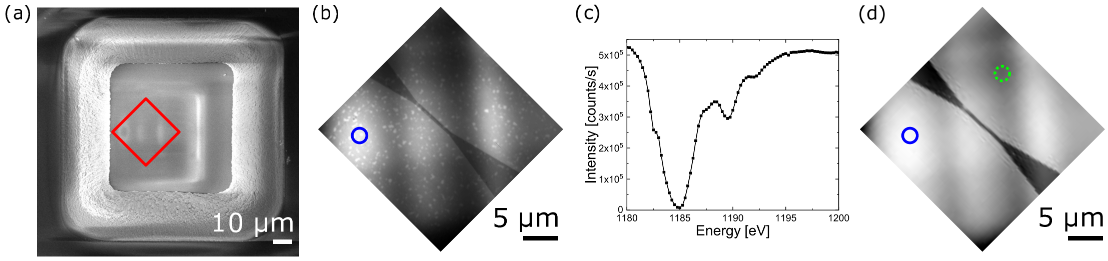

Figure 3.7: Comparison of transmissivity between electrons and soft x-rays of a Ga-doped YIG film grown on GGG (a) Scanning electron micrograph at 10 kV. (b) STXM image of the detail indicated by the red square in (a) taken at the Fe L_3 edge. (c) X-ray transmission spectrum at the Gd M_5 edge taken at the thinnest position indicated by the blue circle in (b). (d) Logarithmic transmittance of the window taken at 1150 eV. The blue and dotted green circle indicate the points for the thickness calculation. Adapted from [77]. Published under CC BY 4.0.

The milled window in the second sample was then imaged using STXM. At the thinnest region, an area of at least 25 µm × 25 µm is transparent for x-rays at the Fe L_3 absorption edge at $\approx$ 708 eV (Fig. 3.7b). The STXM image corresponds to the area marked in red in the SEM image. When comparing the two images, one sees that areas of bright grey level exist in the SEM image, which also appear as bright regions in the STXM image. This means that they are thinner than the surrounding parts. Nevertheless, with spectroscopy measurements at the Gd M_5 edge (Fig. 3.7c), a reduced transmitted intensity, corresponding to an increased absorption of the Gd, confirms that, even in these thinnest regions, Gd is still present, which means that there is GGG substrate remaining everywhere. The absolute thickness of the remaining substrate can be estimated using the Beer-Lambert law $I_t = I_0 \times e^{-d/\lambda}$ [87–89]. For this purpose, the incoming (I_0) and transmitted beam (I_t) at a photon energy of 1150 eV were measured. A corresponding logarithmic transmittance image is shown in Fig. 3.7d. The 150 nm thick Ga-doped YIG film transmits approximately 71% of the incoming beam and the GGG substrate has an absorption length λ of 0.335 µm [90]. This leads to a GGG thickness of approximately 100 nm at the thinnest point and of approximately 500 nm at a thicker point, marked in Fig. 3.7d by the blue and dotted green circle, respectively. These calculations additionally confirm that the remaining substrate is sufficiently thick so that the Xe$^+$ ions and subsequently generated charged particles do not penetrate into the thin film. Here another advantage of using Xe$^+$ ions for the milling becomes obvious: They have a lower penetration depth than conventionally used Ga$^+$ ions at the same energy. For the case of GGG, the penetration depth is 11 nm for

Xe^+ ions compared to 14 nm for Ga^+ ions, as calculated by Monte-Carlo simulations using the SRIM code [91]. The white spots in the STXM image are Fe depleted areas of the film which is inferred from spectroscopic measurements at a different energy where they are not visible (Fig. 3.7d) and, therefore, they do not originate from the PFIB milling. The tapered diagonal dark contrast structure in the STXM image is a microwave antenna, which was lithographically patterned onto the Ga:YIG film after the PFIB milling step and which is therefore not present in the corresponding SEM image. The comparison between the SEM and STXM images shows that even though a large area of the window is suitable for soft x-ray transmission measurements, there are small variations in thickness, which can be observed already in the SEM image during fabrication so that the milling could be adapted in situ.

The use of a Xe PFIB for milling soft x-ray transparent windows is widely applicable to materials that cannot be grown on amorphous Si_3N_4 membrane substrates, especially for situations where large areas or multiple windows are needed. The windows in the samples in Chapters 6 and 7 were fabricated using the method described here and sample specific details are given in the respective chapters.

4 Spin-Wave Emission from Vortex Cores under Static Magnetic Bias Fields

The content of this chapter has been published in Mayr et al., Nano Letters 21(4) p. 1584-1590 (2021) [30]. My contribution to this work is fabricating the single ferromagnetic layer sample (sample #2), performing the STXM measurements as part of a beamtime team, analysing and interpreting the experimental data, directing the simulations and writing the manuscript with input from the other authors.

As introduced in Section 2.4.2, natural internal magnetic field-inhomogeneities such as magnetic vortex cores can be employed to excite spin waves with short wavelengths. Driven by alternating magnetic fields and, in the absence of magnetic anisotropies, these spin waves propagate away from the vortex core radially [9, 49–53]. However, for long-distance signal transmission, a directional rather than radial emission and propagation of spin waves would be highly beneficial to reduce the effects of geometrical damping. Such geometrical damping occurs for a radial spin-wave emission from a point-like source into an extended medium in addition to magnetic damping. A directional emission in a confined element can e.g. be achieved in a synthetic ferrimagnet (SFi) by introducing an intrinsic magnetic anisotropy to the system. Thus a one-dimensional (1D) magnetic domain wall is formed in addition to the zero-dimensional (0D) vortex core [54] as shown in Figure 2.2. This additional dimensionality results in a directional plane-wave emission, which is characteristic for spin waves excited by driven magnetic domain walls [55, 92, 93]. Despite these examples of permanently formed domain wall spin-wave emitters, a source of short-wavelength spin waves, whose position and directionality can be continuously controlled by external stimuli such as a magnetic bias field, is highly desired.

In this chapter, it is demonstrated that magnetic vortex cores under the influence of a static magnetic bias field can be used as manipulable spin-wave emitters. It is shown that one can continuously displace a vortex core from its equilibrium position in the centre of a patterned structure in a controlled and reproducible way while sustaining its driven spin-wave emission. The extent of this displacement is controlled by an external magnetic bias field and is fully reversible. In contrast to spin waves in unpatterned thin films, the dispersion relation of these emitted waves in the experimentally observed frequency range is not noticeably affected by the applied magnetic bias field. Furthermore, it is shown that, in a single ferromagnetic layer, a transformation of the vortex core from a point source to an extended object occurs at higher applied fields. This transformation effectively changes the vortex core from a 0D to a 1D spin-wave source. The 1D character of the emitter leads to a directional emission and propagation of spin waves. The shape of the core depends on the magnitude of the applied magnetic field, making it a controllable source for planar, propagating spin waves. Finally, with micromagnetic simulations it is shown that, by changing the excitation frequency and the shape of the vortex core, spin-wave focusing effects can be achieved.

4.1 Sample Properties

Two different sample systems consisting of disks of ferromagnetic layers were analysed. Sample #1 is a SFi consisting of disks patterned from a Co/Ru/$Ni_{81}Fe_{19}$ trilayer where the thickness of the Ru (nominally 0.8 nm) is chosen such that it mediates antiferromagnetic interlayer exchange coupling between the 45 nm thick $Ni_{81}Fe_{19}$ (referred to as NiFe) and the 48 nm thick Co layer [94]. Sample #2 consists of disks patterned from a single, nominally 100 nm thick ferromagnetic (FM) NiFe film.

The ground state of the Co and NiFe structures in sample #1 are magnetic vortices with an in-plane flux-closure of the magnetization and the central cores pointing perpendicular to the film plane [21, 22]. Due to the antiferromagnetic interlayer coupling, the vortices in the two layers have opposite in-plane circulations whereas, due to dipolar coupling, their polarities are parallel (see Fig. 4.1a). The ground state of sample #2, consisting only of a single ferromagnetic layer, is similarly a magnetic vortex with an in-plane flux-closure of the magnetization and its central core pointing perpendicular to the film plane as shown in Figure 4.1b.

Both of the sample systems investigated are similar to samples where the emission of spin waves from vortex cores without the presence of magnetic bias fields has been reported in the past [9, 49].

4.2 Sample Fabrication

The films for both samples were deposited on 200 nm thick Si_3N_4 membranes by dc magnetron sputtering. In contrast to sample #1, where all lithography steps were performed on the front side of the Si_3N_4 membrane, the films for sample #2 were deposited on the back side of the membrane. As the sputter deposition rate is lower onto the depth-confined membrane on the back than onto a flat substrate, the NiFe film is presumably thinner than the nominal 100 nm. For both samples, the magnetic thin

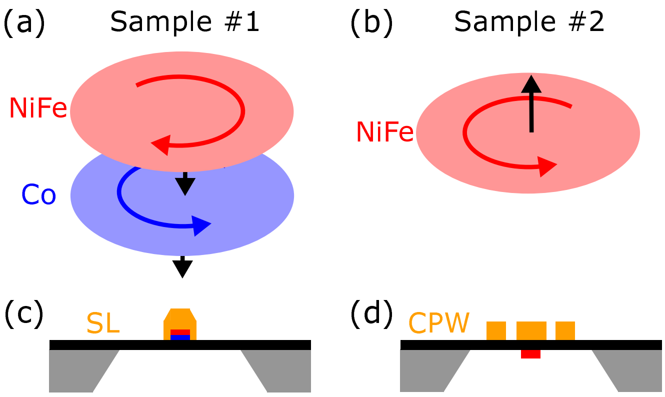

Figure 4.1: Schematics of the samples. (a,b) The vortex structure of the two samples with their in-plane flux closure and the central core pointing perpendicular to the plane is shown. (c,d) Details of the sample structures. (c) Sample #1 where the lithography was performed on the front of the membrane and the microstripline (SL) was patterned on top of the magnetic structures. (d) The magnetic structures of sample #2 were fabricated on the back of the membrane, while the coplanar waveguide (CPW) was patterned on the front of the membrane.

films were capped with a 5 nm Al layer for protection against oxidation. Out of these continuous films, disk structures of approximately 3 µm in diameter were defined by electron beam lithography (EBL) and Ar ion beam etching. This process was performed differently for the two samples: For sample #1, after an initial oxygen plasma treatment to improve the adhesion of the resist, a negative resist (MA-N 2910) was spin-coated onto the Co/Ru/$Ni_{81}Fe_{19}$ multilayer films. Then the microelements were exposed by an electron beam writer. The samples were then developed in MA-D 525 for 300 s and rinsed in deionized water. To physically etch the structures, the samples were exposed to an Ar ion beam at two different angles (85° and 5°). The remaining resist was removed by acetone and an additional oxygen plasma treatment. For sample #2, a hard mask was used, which was patterned using a standard lift-off process as described in 3.1 with a 1 nA electron beam with a voltage of 100 kV and a dose of 1600 $\mu C/cm^2$. The etch mask itself consists of 85 nm Ta, which was again deposited by dc magnetron sputtering. Subsequently, the samples were etched with Ar ions at an angle of 30°.

On top of the structures, a conductive, 200 nm thick, 5 µm wide Cu microstrip (sample #1, directly on top) or 5 µm wide coplanar waveguide with a 4 µm gap (sample #2, Si_3N_4 in between) was patterned via electron beam lithography and lift-off processing as described in 3.1. For sample #1, the Cu was deposited by electron beam evaporation. For sample #2, the Cu for the coplanar waveguide was thermally evaporated. The lithographical structures of sample #1 and sample #2 are shown schematically in Figures 4.1c and 4.1d, respectively. This illustrates the advantage of fabricating the magnetic microstructures on the opposite side of the membrane to the conductive stripline, which is to achieve a continuously flat stripline even at the location of the structures.

4.3 Synthetic Ferrimagnet

4.3.1 Radial Emission of Spin Waves from Displaced Vortex Cores

When a static in-plane magnetic bias field is applied to the vortex structures in sample #1, the cores of these vortices are displaced from the disk centre congruently in both layers as can be seen for an applied magnetic field of 5 mT in the absolute absorption image in Fig. 4.2a. This means that the region of the vortex pair, where the dominant magnetization (in the Co layer) is aligned parallel with the applied field, expands to minimize the Zeeman energy. This behaviour is in agreement with previous findings for vortices in single layers [95] as well as for coupled vortices [96]. For the strictly antiferromagnetically coupled vortices studied here, in one of the ferromagnetic layers, the field-unfavourable domain, which is oriented antiparallel to the applied field, has to expand. This is the case for the NiFe layer here, due to its lower magnetic moment per unit area [96]. When now an rf excitation is applied to the stripline, generating an oscillating in-plane magnetic field, spin waves are emitted from the displaced vortex cores. The mechanism behind this emission of short-wavelength spin waves lies in the strongly enhanced local effective magnetic fields and, hence, torques that are present near the vortex core, which couple to the spin-wave continuum. These torques stem from the small oscillating motion that the vortex core performs upon its excitation [9]. A radial emission from the displaced cores is observed, in a very similar way to a radial emission when no static field was applied. An example of such an isotropic emission and radial propagation for an excitation frequency of 1.1 GHz is shown in the normalized snapshot of a time-resolved STXM image in Fig. 4.2b.

A higher magnetic field (10 mT) leads to a larger core displacement, further away from the centre as depicted in Fig. 4.2c, where the vortex core approaches the edge of the disk. As shown in the normalized view in Fig. 4.2d, the spin-wave emission remains mainly radial from the source. This becomes more visible in the time-resolved movies. The deviations from the radial emission presumably originate from imperfections in the sample. From the normalized images, the wavelengths of the spin waves can be determined to be 348 nm ± 12 nm and 348 nm ± 8 nm for bias fields of 5 mT and 10 mT, respectively. This demonstrates that the wavelength and, hence the dispersion relation of the collective Damon-Eshbach waves, is not noticeably affected by the static magnetic bias field in the experimentally observed range of magnetic fields and

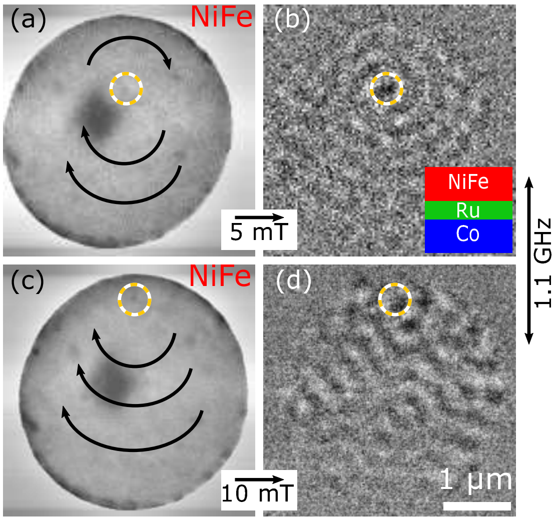

Figure 4.2: TR-STXM of sample #1 (SFi), acquired with out-of-plane magnetic sensitivity at the Fe L_3 edge at two different static magnetic fields (5 mT and 10 mT). (a,c) Absolute absorption images (snapshots of time-resolved measurements) showing the position of the vortex core visible as a black dot (corresponding to the magnetization pointing into the disk plane), which is indicated by a yellow dashed circle. The dark contrast in the centre of the disk is topographic. Black arrows represent the in-plane magnetization orientation of the top layer (NiFe) in the disk, where the unfavourable domain expands. (b,d) Normalized contrast snapshots displaying the radial spin-wave emission from the core for an excitation frequency of 1.1 GHz. The inset is a schematic of the SFi trilayer stack. Taken from [30]. Published under CC BY 4.0.

excitation frequencies. This is because the internal magnetostatic field, as a result of the core displacement, compensates the external magnetic field and therefore in most of the vortex structure, the effective magnetic field remains almost the same as in the zero-field configuration. For the applied fields of 5 mT and 10 mT, the cores in both layers, NiFe and Co, shift together without decoupling due to the strong interlayer exchange coupling with a bilinear coupling constant of the order of $\approx -0.3\,\mathrm{mJ/m^2}$ [49]. When higher magnetic fields are applied, the cores in the two layers can decouple [96] before the vortices are expelled.

4.3.2 Properties of the Emitted Spin Waves

To show that the spin waves observed in the SFi sample #1 are layer-collective Damon-Eshbach waves and that the vortex cores are displaced together without decoupling within a certain field range, the dynamics of the two ferromagnetic layers were imaged separately. Hence, by tuning the x-ray energy to the L_3 absorption edge of either Fe or Co, sensitivity to the magnetization of only the NiFe or Co layer is achieved, respectively.

The response to an excitation with a frequency of 1.1 GHz is shown in the snapshots at the same delay time in Fig. 4.3a for the NiFe and in Fig. 4.3b for the Co layer. The applied magnetic bias field is 5 mT. Even though the dynamics is more visible in the NiFe layer, spin-wave emission can also be observed in the Co layer with the same pattern and phase. The signal difference most likely is a result of the lower spin-wave amplitude in the Co layer. Furthermore, it can be observed from the dynamics that the vortex cores are located at the same position for both layers, meaning that they are displaced together without lateral decoupling. Additionally, measurements at different frequencies were performed to demonstrate that the wavelengths of the spin waves can be tuned by varying the excitation frequency as is also the case without a magnetic bias field applied as shown in Fig. 4.3a and c. It can be seen that, for an excitation frequency of 1.1 GHz, the resulting wavelength is 348 nm ± 12 nm and that it reduces to 193 nm ± 7 nm at 2.1 GHz. This demonstrates that the wavelengths of the emitted spin waves can be tuned by with the driving frequency even in the presence of static magnetic bias fields.

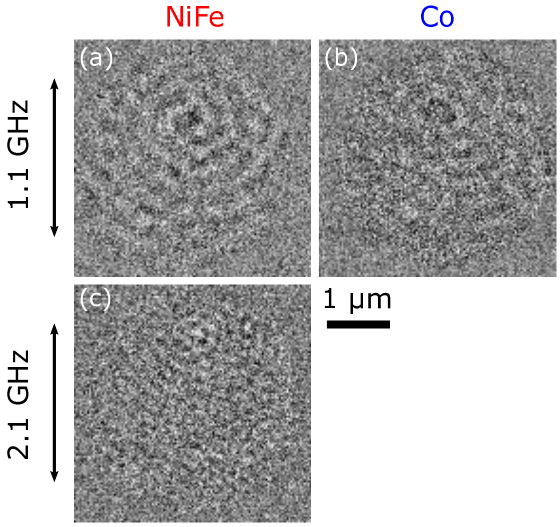

Figure 4.3: Normalized time-resolved STXM images of SFi sample #1, taken with out-of-plane magnetic sensitivity at an in-plane magnetic bias field of 5 mT. Top row: Images recorded at an excitation frequency of 1.1 GHz at the (a) Fe and (b) Co L_3 absorption edges, displaying separately the dynamics in the NiFe and Co layer, respectively. Left column: Images taken at the Fe absorption edge at frequencies of (a) 1.1 GHz and (c) 2.1 GHz, illustrating that the wavelength can be tuned with the excitation frequency. Taken from [30]. Published under CC BY 4.0.

4.4 Single Ferromagnetic Layer

4.4.1 Expansion of the Vortex Core and Influence on the Emission

The behaviour of sample #2, which consists of a single NiFe layer, is similar to the SFi sample for small magnetic fields of below approximately 15 mT. These small fields lead to a moderate displacement of the vortex core from the centre and a radial spin-wave emission is observed from the core as shown in Figure 4.4a. As for the case without a magnetic bias field applied, the emission occurs at higher frequencies than for the SFi, and the observed spin waves correspond to the first higher-order mode of the single-layer Damon-Eshbach geometry with a non-homogeneous precession profile over the film thickness [9]. When a higher magnetic bias field is applied, which moves the core closer to the edge of the disk, an expansion of the vortex core is observed [97–103], as shown in the absolute image in Figure 4.4b. The closer the vortex core gets to the edge, the further it expands (see Fig. 4.4c). This core expansion is a consequence of the energetically driven tendency of the magnetization to align parallel to the edge of the disk. Here, the expanded core resembles a 180° Bloch domain wall, following the curvature of the rim of the disk.

It should be noted that the expanded core exhibits a non-trivial three-dimensional (3D) structure, where the magnetization at each lateral point is not necessarily fully perpendicular to the plane along the thickness cross-section [101]. In fact, the fully perpendicular fraction of the cross-section connects, in a tubular way, the separated lateral surface points of fully perpendicular magnetization at the top- and bottom surface of the film (see Fig. 4.5). For the ground state, the combination of core polarity (up or down) and external field direction defines which surface point (top or bottom) is shifted to which end of the expanded core (left or right). In the STXM measurements, where the signal is averaged over the thickness of the film, these slight 3D variations are not visible and one can simply consider that the vortex core changes from an effective 0D point source to an extended 1D object [97, 104–106]. As a consequence of the expansion of the spin-wave emitter, the emission pattern of the spin waves changes. This change can be seen in the normalized STXM images in the right-hand column of Fig. 4.4.

The emission of spin waves from an expanded vortex core is examined in more detail as shown in Fig. 4.6. Shown in Fig. 4.6a is the expanded core for a magnetic bias field of 22.5 mT, corresponding to Figure 4.4b. The spin-wave emission from this core can be seen in the normalized snapshot shown in Fig. 4.6b for an excitation frequency of 8.6 GHz. Mostly planar waves propagate away from the expanded core in both directions perpendicular to the long axis of the core. This propagation is highlighted in Fig. 4.6c, showing the intensity profile along the yellow arrows in Fig. 4.6b for

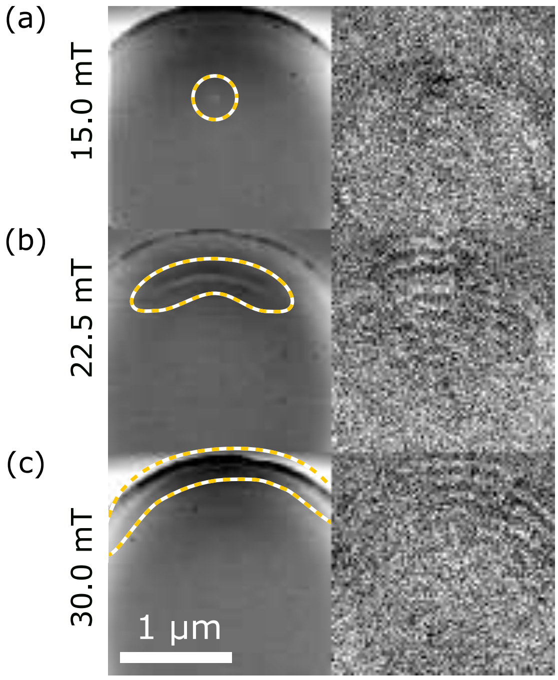

Figure 4.4: STXM images of the vortex core at static magnetic bias fields of (a) 15.0 mT, (b) 22.5 mT and (c) 30.0 mT. Left column: Absolute absorption images depicting the expansion of the core (white contrast, indicated with yellow dashed frames) as it moves closer to the disk edge for higher magnetic fields. Right column: Normalized images where the influence on the emission of the spin waves becomes visible for an excitation frequency of 8.6 GHz. Adapted from [30]. Published under CC BY 4.0.

two snapshots with a relative time delay of 33 ps. From such intensity profiles, the wavelength can be extracted to be 146 nm ± 9 nm. A comparison to the case without a static magnetic field, where the wavelength is 143 nm ± 8 nm (not shown), confirms that, even for the situation of a field-expanded vortex core, the wavelength of the spin waves remains almost unaffected by the external field. This is again due to the effective field compensation, as already discussed for the SFi system in Section 4.3.

To gain further insight into the spin-wave emission from a 1D expanded vortex core, micromagnetic simulations were performed with MuMax3 [28]. The result of such a simulation is shown as a STXM-comparable snapshot in Fig. 4.6d for an excitation frequency of 8.5 GHz and a magnetic bias field of 20 mT, similar to the experiments. For these simulations, the disk diameter was 3.1 µm, the thickness 72 nm and an initial magnetization of a vortex with anticlockwise circulation and polarity pointing upwards was set. To reproduce the experiment, the simulated thickness of 72 nm is significantly smaller than the nominal experimental thickness of 100 nm, which may result from a reduced sputter deposition rate onto the depth-confined back of the membrane com-

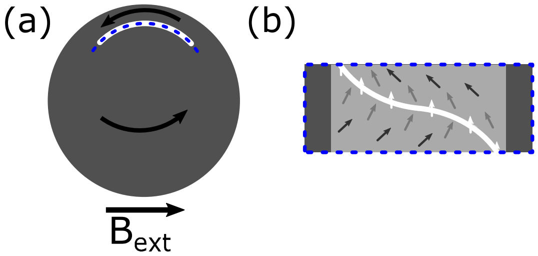

Figure 4.5: Schematics of the expanded vortex core. (a) Top view. Black arrows represent the in-plane orientation of the magnetization. (b) Cross-sectional view along the dashed blue line in (a) depicting the 3D structure of the expanded core over the film thickness, where the core (white contrast) shifts to opposite sides when going from the top to the bottom of the film. The grayscale of the arrows indicates the magnetization component pointing out of plane with white indicating upward pointing magnetization, which transitions to black for horizontal magnetization. Taken from [30]. Published under CC BY 4.0.

pared to that onto a flat substrate. A cell size of 3 nm × 3 nm × 3 nm was chosen for the simulation. The static bias field and the dynamic excitation field $B_{dyn} = 1\,\mathrm{mT}$ were simulated to be in the film plane but perpendicular to each other, as for the experiments. A saturation magnetization of $M_s = 800\,\mathrm{kA/m}$, an exchange constant of $A = 8 \times 10^{-12}\,\mathrm{J/m}$, a gyromagnetic ratio $\gamma = 1.854 \times 10^{11}\,\mathrm{rad/(sT)}$ and a Gilbert damping $\alpha = 0.01$ were used, which leads to a wavelength of 136 nm ± 5 nm. Note that the value for the exchange constant A is smaller than that typically utilized to simulate NiFe thin films, yet this value is in good agreement with previously investigated NiFe films of similar thickness [9].

Besides the spin-wave emission pattern from the centre of the expanded core, the simulations show an equally strong spin-wave emission from its outer parts, which only occurs at a much weaker level in the experiments. This difference cannot be fully explained at present, but it is speculated that the outer parts are more difficult to excite in the experiment due to the influence of material and fabrication imperfections.

4.4.2 Focusing of Spin Waves

The shape and extent of the vortex-core expansion can be controlled by the magnetic bias field to influence the emission pattern of the spin waves. The spin waves are not emitted as fully planar waves from the curved core, which leads to a geometrical focusing effect [107–110], an indication of which can be seen in the experimental data shown in Fig. 4.6b. This effect can also be seen in the micromagnetic simulation shown in Fig. 4.6d. While these focusing effects are weaker in the experiments, which is presumably due to an insufficient spin-wave propagation length resulting from damping. Therefore,

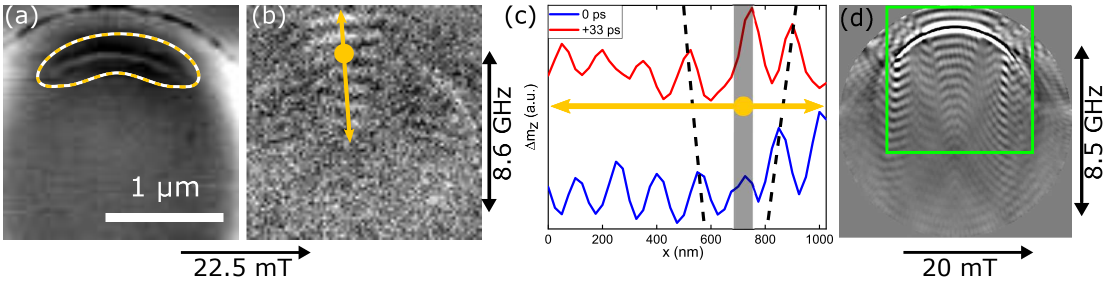

Figure 4.6: Spin-wave emission from an expanded vortex core. (a,b) TR-STXM with out-of-plane sensitivity displaying the response of the vortex in sample #2 to an in-plane static magnetic field of 22.5 mT and an alternating field excitation of 8.6 GHz frequency. (a) Absolute absorption image depicting the expanded vortex core displaced from the center (white contrast indicated by yellow dashed frame). (b) Normalized snapshot image showing only the temporal changes with respect to the average magnetization, displaying the emitted spin waves. (c) Intensity profiles along the yellow arrows in (b) at a relative time delay of 33 ps illustrating wave propagation away from the vortex core (grey area) in both directions as indicated by the dashed lines. (d) Micromagnetic simulation showing the directional spin-wave emission and subsequent focusing. The green box indicates the region of interest used in the STXM shown in (a,b). Taken from [30]. Published under CC BY 4.0.

the influence of the magnetic field and excitation frequency are further studied via simulations. Exemplary simulations performed using MuMax3 [28] are shown in Fig. 4.7 for frequencies of 8.5 GHz and 9.5 GHz and static magnetic fields of 20 mT and 25 mT. These simulations confirm the experimental finding that the wavelength of the spin waves is independent of external bias fields and instead can be tuned with the excitation frequency, i.e shorter wavelengths can be achieved for higher frequencies. For a magnetic field of 20 mT (top row in Fig. 4.7), the wavelength changes from 136 nm ± 5 nm at 8.5 GHz to 110 nm ± 5 nm at 9.5 GHz. Additionally, a further expansion of the core at 25 mT coincides with a broader spin-wave emission pattern from the central core region, which then leads to a less pronounced focusing of the emitted waves. This shows that the extent to which focusing occurs depends on both the applied field bias and the excitation frequency, therefore making the vortex core not only an emitter of short-wavelength spin waves, but also a controllable lens for the spin waves [111–114].

Typically, for a focusing effect, an increase in the spin-wave amplitude is expected towards the focal point. Such an amplitude increase is neither observed in these experiments nor in the corresponding simulations (see simulation in Fig. 4.8a). However, this lack of amplitude gain is mainly a result of the magnetic damping of the present material ($\alpha = 0.01$). For a simulation assuming a lower magnetic damping of $\alpha = 0.0001$, which corresponds to a material such as yttrium iron garnet, an increasing amplitude

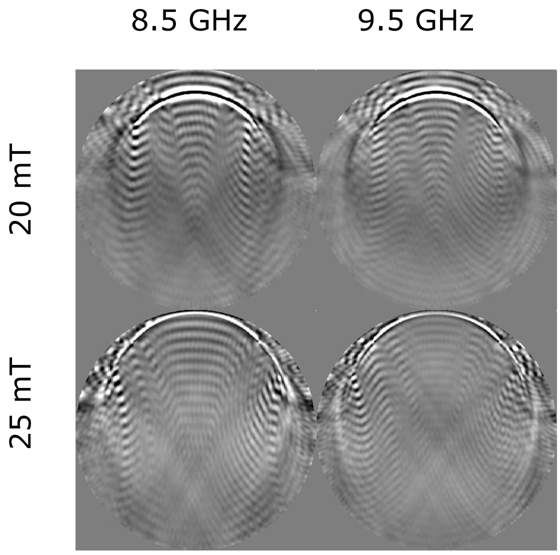

Figure 4.7: Normalized micromagnetic simulations for static magnetic fields of 20 mT and 25 mT, and excitation frequencies of 8.5 GHz and 9.5 GHz. Taken from [30]. Published under CC BY 4.0.

can indeed be observed towards the focal point (Fig. 4.8b). This becomes evident from intensity profiles taken along the yellow arrows in the corresponding simulation images.

4.5 Conclusions

It was demonstrated with direct TR-STXM imaging that a static in-plane magnetic bias field can be used to continuously displace the position of vortex core spin-wave emitters. These emitters are driven by alternating magnetic fields and they act as coherent sources for spin waves with nanoscale wavelengths. In a synthetic ferrimagnetic trilayer structure, it is possible to congruently displace the coupled vortex cores while maintaining their radial spin-wave emission pattern. For a relatively thick single-layer film, higher magnetic fields lead to an expansion of the vortex core from an effective point source to an extended 1D object. This expansion changes the emission pattern of the spin waves from circular to rather planar waves that propagate away from the core in both directions perpendicular to the axis of expansion. It is observed that the external magnetic field and the corresponding expansion of the core do not noticeably change the spin-wave dispersion relation within the vortex structure as a result of internal field compensation. Furthermore, micromagnetic simulations confirm these experimental findings and predict that for certain static magnetic fields - and thus core shapes - spin-wave focusing effects occur. These results show that magnetic vortex cores can be used as continuously displaceable, reshapeable and controllable spin-wave sources

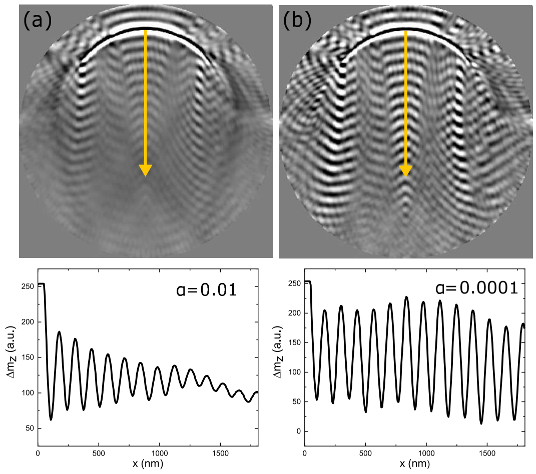

Figure 4.8: Comparison of simulations with different magnetic damping constants. Normalized micromagnetic simulation images for a static magnetic field of 20 mT and an excitation frequency of 8.5 GHz, with a Gilbert damping constant of (a) $\alpha = 0.01$ and (b) $\alpha = 0.0001$. Intensity profiles along the corresponding yellow lines are shown below each respective image. Taken from [30]. Published under CC BY 4.0.

where a directional emission and focusing of spin waves is achieved by applying a static magnetic field without the need for additional waveguide patterning.

5 High-Frequency Spin Waves with Short Wavelengths in Metallic Thin-Film Samples

The content of this chapter is in preparation for publication as Mayr et al., "Time-resolved x-ray imaging of spin dynamics at tens of GHz *using low-alpha synchrotron operation" [115]. My contribution to this article is fabricating several of the single ferromagnetic layer samples, participating in the STXM measurements of the single ferromagnet layer samples, partially analysing the experimental data of both sample systems, applying an analytical model for fitting of the dispersion relations for the single ferromagnetic layer samples and co-writing the manuscript.*

The computational speed of prospective spin-wave based devices scales with their operation frequency. Therefore, high intrinsic spin precession frequencies of the used materials are an important prerequisite. However, the intrinsic resonances of ferromagnets are typically in the low GHz regime. A way to increase their frequencies is to introduce precessional nodes into the otherwise uniform precession through the thickness of the film. These nodes are caused by vertical confinement due to a finite film thickness and coincide with an antiphase precession. This antiphase precession adds strong exchange and dipolar energy contributions, which typically lead to an increase in frequency. Such precession nodes can be introduced into ferromagnetic layers by stacking two layers with a non-ferromagnetic interlayer in-between [49, 54, 93], where a quasi-node forms, and they intrinsically occur in single layers as spin waves of higher order through the thickness, which are also referred to as perpendicular standing spin waves [9, 116–124].

In this chapter, it is demonstrated that STXM can be used to image several short-wavelength spin-wave modes with wavelengths down to 70 nm at frequencies up to 30 GHz by utilising the low-alpha optics operation mode at the Bessy II synchrotron. In a ferromagnetic bilayer system, where the two ferromagnetic layers are aligned antiparallel to each other, non-reciprocal spin waves of both acoustic and optical modes are observed. In single ferromagnetic layer systems, possibilities to tune the dispersion relation by material properties, by altering the layer thickness and through the application of an external magnetic bias field are shown. Spin waves of the fundamental quasi-uniform mode in the Damon-Eshbach geometry as well as higher order modes, which possess precessional nodes along the thickness of the film, are imaged up to the fourth order.

5.1 Sample Properties

The first sample system investigated was a trilayer stack consisting of two ferromagnetic layers [Co and $Ni_{81}Fe_{19}$(referred to as NiFe)], each with a thickness of 50 nm thickness, and separated by a 10 nm thick Cu interlayer (see Fig. 5.1a, all thicknesses are nominal). From this stack, micrometre sized elements were patterned.

Upon subsequent demagnetization, the disks were found to exhibit two different, non-deterministic sets of remanent states, namely vortex pairs with either opposite or equal vortex circulations, as shown for an exemplary 2 µm disk in Figure 5.1b and c [96, 125, 126]. Such a bistable behaviour can be expected for laterally confined, dipolar coupled layers, where the Cu thickness is above the range for which interlayer exchange coupling is mediated [126].

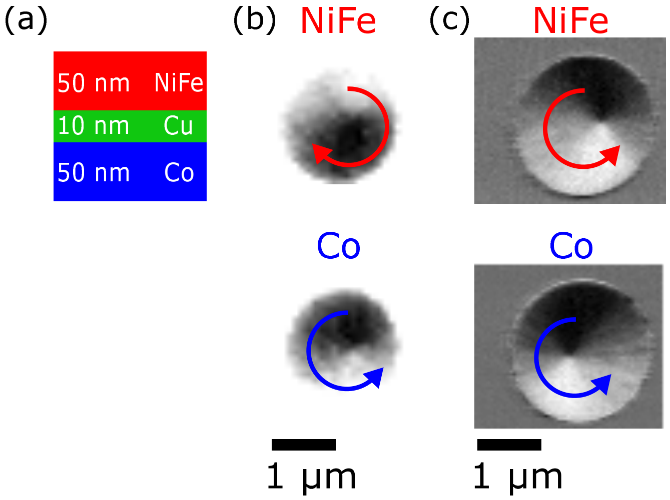

Figure 5.1: Overview of the trilayer stack. a) Schematics of the two ferromagnetic layers separated by a Cu interlayer. b,c) STXM images depicting the two studied remanent states of the two ferromagnetic layers taken at a tilt angle of 30° to the x-ray beam for sensitivity to the in-plane magnetic contrast . The arrows indicate the vortex circulation. b) Opposite vortex circulations in the two layers imaged with a single x-ray polarisation. c) XMCD images of the parallel circulations of the ferromagnetic layers.

The case of opposite vortex circulations is shown in Fig. 5.1b, where the m_x-components and, thereby, the vortex in-plane states were imaged separately for Co and NiFe by STXM using a single x-ray polarisation. While opposite vortex circulations can be identified, it was found that the vortex core positions were not always identical in both layers, i.e. the cores exhibited a relative lateral shift to each other, while the core polarisations were not directly resolved. Such core shifts occurred with varying magnitude for both static and magnetically excited cases. Possible reasons for these shifts could lie in a potential thickness gradient in one or both of the magnetic layers, a repulsive coupling between antiparallel vortex core polarisations [127], or the dynamic excitation of the cores.

The case of parallel vortex circulations in the ferromagnetic layers of the disk is shown in Figure 5.1c. Both circular x-ray polarisations were imaged with in-plane sensitivity separately for Co and NiFe to form XMCD images revealing pure magnetic contrast. Here, both vortices are in the same circulation state with off-centred cores that are laterally separated by 500 nm. This leaves the area between them where the magnetization in the layers is aligned antiparallel while in the other parts of the sample the layer magnetizations are aligned parallel. The possible reasons for this relative core shift are the same as for the case of antiparallel circulations. However, the separation can be higher for parallel circulations as here the reduction of energy obtained by separating the cores is almost self-compensating from a magneto-dipolar point of view.

The second sample system consists of patterned disks of single ferromagnetic layers [NiFe and $Co_{40}Fe_{40}B_{20}$(referred to as CoFeB)] of several different thicknesses. NiFe samples with thicknesses of 25 nm (NiFe25), 50 nm (NiFe50) and 100 nm (NiFe100) as well as CoFeB samples with thicknesses of 50 nm (samples CoFeB50a and CoFeB50b) and 100 nm (CoFeB100) were investigated. The ground state of each sample is a magnetic vortex.

5.2 Sample Fabrication

All studied samples were fabricated on 200 nm thick x-ray transparent Si_3N_4 membranes. The thin films for the trilayer sample were deposited by electron beam evaporation, whereas the films for the single ferromagnetic layers were deposited by dc magnetron sputtering or thermal evaporation. For most samples, all lithography steps were performed on the front side of the Si_3N_4 membrane, only the film for sample CoFeB50b was deposited on the back of the membrane. As the sputter deposition rate is lower onto the membrane on the back of the chips than onto a flat substrate, this CoFeB film is presumably thinner than the nominal 50 nm.

The patterning of the disk and ellipse structures with diameters between 2 µm and 7.5 µm was performed by electron beam lithography and lift-off processing for all samples. First a bilayer of the positive resists methyl methacrylate(MMA)/poly(methyl methacrylate) (PMMA) was spincoated onto the membranes. The structures were defined by electron beam lithography, subsequently developed in a methyl isobutyl ketone:isopropyl alcohol (MIBK:IPA) mixture and then rinsed in IPA. After deposition of the materials, the lift-off was performed in acetone.

On top of the patterned structures, an electrically conductive coplanar waveguide (sample CoFeB50b, on the opposite side of the Si_3N_4) or microstrip (all other samples, directly on top) was patterned via electron beam lithography and lift-off processing. The material for the 200 nm thick Cu conductors was deposited by electron beam evaporation for the trilayer sample and by thermal evaporation for the single-layer samples.

5.3 Trilayer Stack

5.3.1 Antiparallel Vortex Circulations

When the disk element with opposite vortex-circulation state is excited by an alternating, quasi-uniform magnetic field, spin waves with sub-micrometre wavelengths are excited at the vortex cores in both layers and subsequently propagate to the edge of the disk. This is exemplarily shown in the normalised dynamic STXM snapshots for an excitation with a frequency of 4.29 GHz and a magnitude of approximately 1 mT in Fig. 5.2a for the NiFe and Co layers. The wavelength of the spin waves is determined to be 320 nm ± 27 nm. By comparing the spin-wave response of the two different layers, it becomes obvious that they locally exhibit the same phase in their dynamic m_z component. This means that the waves correspond to the layer-collective acoustic mode of antiparallel ferromagnetic bilayers in the Damon-Eshbach geometry, as was already discussed earlier in Chapter 4. In other works, this kind of mode was found to be strongly non-reciprocal, in the sense that waves of the same frequency propagating in opposite directions exhibit substantially different wavelengths [49].

In contrast to earlier findings, the spin-wave emission pattern in the present experiment is notably asymmetric as the waves are mainly emitted towards the bottom half of the disk, while there are almost no waves present in its upper half. Assuming that one of the cores was more dynamically susceptible, this asymmetry could be a consequence of the relative lateral shift between the vortex cores, causing a local region to be in the parallel magnetic state, which in turn leads to a mismatch in the dispersion relation.

In the past, vortex-based spin-wave emission in antiparallel magnetic bilayers was observed by TR-STXM mainly for frequencies below 5 GHz [30, 49, 93]. Exploiting the improved time-resolution of the low-alpha operation mode of Bessy II and the particular sample properties, this range was substantially extended as it will be shown in the following.

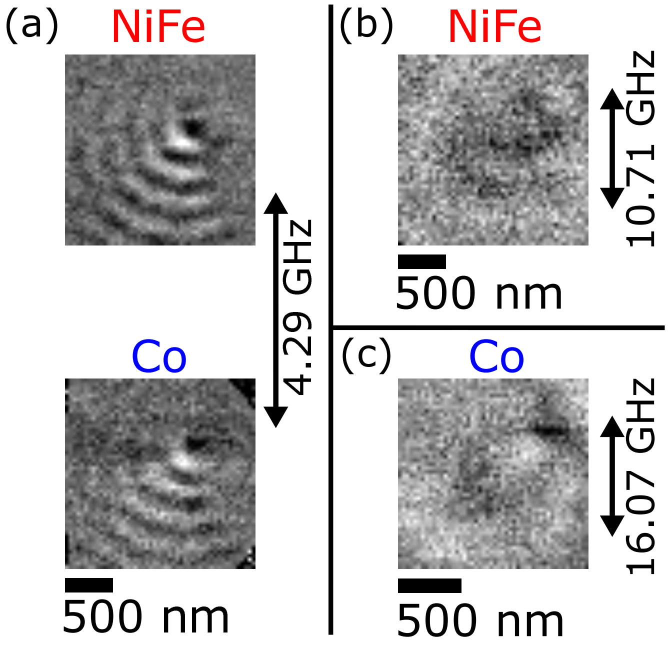

Figure 5.2: Normalised dynamic STXM snapshots of the sample in the antiparallel vortex configuration taken with out-of-plane magnetic sensitivity. a) Spin waves emitted from the vortex cores propagating outwards in the NiFe and Co layer at an excitation with a frequency of 4.29 GHz. b) Response of the NiFe layer to an excitation of 10.71 GHz displaying spin waves propagating inwards as part of the long-wavelength branch of the acoustic mode. c) Optical mode in the Co layer at an excitation with a frequency of 16.71 GHz.

Whereas the wavelength of the spin waves emitted from the vortex cores can be continuously tuned with the driving frequency, as in Chapter 4, at a frequency of 10.71 GHz, at once longer waves with a wavelength of 454 nm ± 114 nm and opposite phase propagation direction (inwards) appear in the dynamic images (Fig. 5.2b). The propagation direction can be determined from the time-resolved movies. Given the strong non-reciprocity of the system, this situation suggests that the outwards propagating waves belong to the short-wavelength branch of the collective acoustic mode of the antiparallel bilayer, while the inwards propagating waves are part of the long-wavelength branch which also fits to the relative equilibrium circulation configuration [49, 54]. Finally, for a frequency of 16.07 GHz, inwards propagating waves of even longer wavelength 932 nm ± 233 nm appear (Fig. 5.2c), which presumably belong to the collective optical mode of the antiparallel system.

5.3.2 Parallel Vortex Circulations with Shifted Cores

When the sample in the state with parallel vortex circulation is excited by alternating magnetic fields, the same kind of acoustic collective spin-wave mode as before is observed propagating within the region between the laterally shifted vortex cores, where the magnetic orientation of the two ferromagnetic layers is antiparallel. This is shown in the absolute and normalised snapshots of TR-STXM measurements with perpendicular magnetic sensitivity for the NiFe layer to an excitation of 4.29 GHz in Fig. 5.3a. Within the region between the cores, waves are propagating from the position of the Co core to that of the NiFe core at a wavelength of 290 nm ± 80 nm. As described before, the spin waves can be excited continuously for increasing frequencies as shown in the normalised TR-STXM snaphots for the NiFe layer for an excitations of 8.14 GHz resulting in a wavelength of 148 nm ± 16 nm (Fig. 5.3b) and 12.14 GHz with a wavelength of 89 nm ± 9 nm (Fig. 5.3c). As before, the waves in the Co layer are in phase with the NiFe layer with respect to m_z.

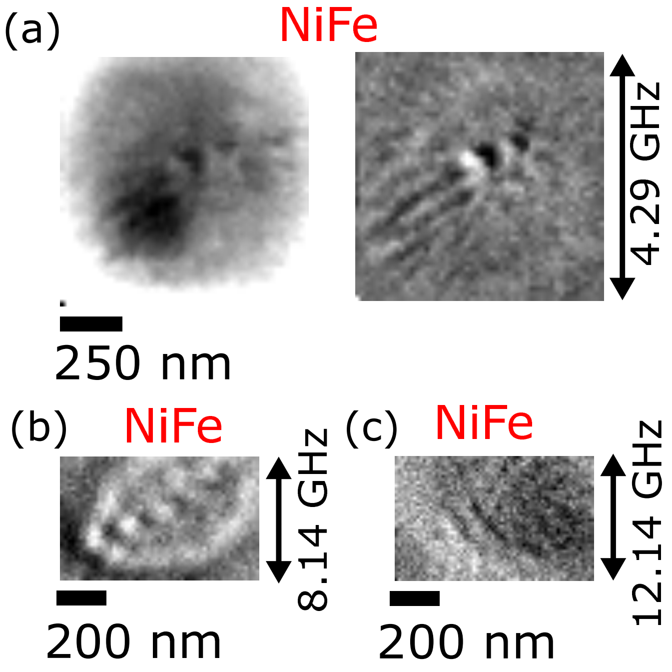

Figure 5.3: Dynamic STXM snapshots of the sample in the parallel vortex configuration taken with magnetic out-of-plane sensitivity. a) Absolute (left hand side) and normalised (right hand side) absorption images of the NiFe layer at an excitation with a frequency of 4.29 GHz, displaying spin waves in the region with local antiparallel orientation. b) Response of the NiFe layer to an excitation of 8.14 GHz. c) Response of the NiFe layer to an excitation of 12.14 GHz.

Furthermore, at excitation frequencies of 14.29 GHz and 15.14 GHz, non-reciprocal waves were observed simultaneously in the time-resolved movies, propagating with opposing phase directions. The waves with propagation direction from the Co to the NiFe core presumably belong to the short-wavelength branch (80 nm ± 7 nm and 71 nm ± 8 nm), while the ones propagating from the NiFe to the Co core belong to the long-wavelength branch (280 nm ± 20 nm and 175 nm ± 17 nm) of the acoustic mode.

5.3.3 Spin-Wave Dispersion in Antiparallel Magnetic Systems

To gain further insight into the relevant spin-wave dispersion relations $f(k)$ of the present antiparallel magnetic bilayer system in the Damon-Eshbach geometry, the experimental data points were plotted as solid dots (antiparallel vortex circulations) and solid squares (parallel vortex circulations) as shown in Figure 5.4.

On the side of positive wavevectors $+k$, all data points (approximately 2 GHz to 15 GHz with wavevectors from 10 rad/µm to 90 rad/µm) are mainly on a diagonal line with positive slope, originating approximately at 0. This situation corresponds to a linear spin wave dispersion, where the phase velocity is equal to the group velocity meaning that waves of all different wavelengths propagate with the same velocity. From the fact that dots and squares follow the same line, it can be concluded that the overall relative vortex circulation configuration (antiparallel or parallel) does not significantly influence the spin-wave dispersion relation as long as the relative layer orientation is locally antiparallel.

At the negative k-branch, the data points span a smaller frequency range between approximately 10 GHz and 16 GHz at wavevectors between 5 rad/µm and 40 rad/µm, meaning that, for the same frequency, the wavelengths along $+k$ are shorter than along $-k$ (short-wavelength vs. long-wavelength branch). This kind of dispersion non-reciprocity is in line with earlier findings [49] for the m_z-acoustic layer-collective Damon-Eshbach mode of antiparallel bilayers. While the red-coloured $-k$ data points below 16 GHz exhibit a monotonous increase of f over k, the one at 16 GHz (depicted in yellow) falls out of this sequence and it will be shown in the following that this is an instance of the higher-energetic m_z-optical mode of the system.

To substantiate the above interpretations, an analytic micromagnetic model was applied to calculate the spin-wave dispersion relations of the system, considering plane spin waves and sublayer discretisation while omitting electromagnetic effects and retardation [54]. The problem is then solved numerically, allowing for a reasonable variation of nominal magnetic and material property parameters for an improved matching with the experimental data points (manual fit). The parameters used were film thicknesses of $d_{NiFe} = 50\,\mathrm{nm}$ and $d_{Co} = 50\,\mathrm{nm}$, exchange constants of $A_{NiFe} = 8.5\,\mathrm{pJ/m}$ and

$A_{Co} = 15\,\mathrm{pJ/m}$ and saturation magnetizations of $M_{s,NiFe} = 740\,\mathrm{kA/m}$ and $M_{s,Co} = 1270\,\mathrm{kA/m}$. It should be noted that the values for the exchange constants are lower than those typically assumed but are at the same time in line with earlier findings of a reduced exchange value in such systems [9, 30]

The four lowest-energy dispersion relations resulting from these calculations are shown as lines in Fig. 5.4 together with the experimental data points. The colour/type line coding is as follows: Colours (red, yellow, blue, green) correspond to specific spin-wave modes, which refers to the distinct character or precession profile of magnetization dynamics, e.g. m_z-acoustic (red) or m_z-optical (yellow). However, these modes are not necessarily continuous in the dispersion plane, but they may hop between continuous spin-wave bands, as indicated by line type, at their avoided crossing points.

From these results it can be seen that the experimental data points are in excellent agreement with the short-wavelength branch of the collective m_z-acoustic mode (red lines) for positive wavevectors and are in reasonable agreement with the long-wavelength branch for negative wavevectors. Moreover, as mentioned above, the experimental data point at around 16 GHz matches the calculated dispersion of the m_z-optical mode, which allows to conclude that this mode was in fact directly observed.

In addition to the experimental results, one can deduce the following from the calculated results: The m_z-acoustic mode has a spin-wave gap of approximately 500 MHz, below which propagating spin waves do not exist. This minimum is not located at $k = 0$ but slightly shifted to positive k values, meaning that there is a k-range with opposing phase and group velocities. In contrast to the short-wavelength branch of the m_z-acoustic mode, its long-wavelength branch intersects with two additional modes at around 9 GHz (mode #3, blue) and at 12 GHz (mode #4, green).

The m_z-optical mode has a spin-wave gap of approximately 1.5 GHz which appears to be close to $k = 0$. These branches with steep slopes are also non-reciprocal, although with an inverted sense and less pronounced than in the m_z-acoustic case. Intersections with modes #3 and #4 occur in both k directions of the m_z-optical mode.

Whereas there are no experimental data points for modes #3 and #4, the calculations indicate that they can be characterised by rather individual magnetic precessions of the different magnetic layers NiFe (blue) and Co (green), respectively. They appear at higher frequencies (NiFe: 9 GHz, Co: 12 GHz) and exhibit parabolic-like precession branches that are almost symmetric in k.

5.4 Single Ferromagnetic Layer Systems

The second sample system consists of single ferromagnetic layers of different thicknesses patterned into disks and ellipses. Unlike the previously described trilayers, single layers typically do not exhibit any spin-wave non-reciprocity in k and, therefore, it is sufficient to focus on positive wavevectors.

5.4.1 Multimode Dispersion

Several spin-wave modes were measured by STXM for a particular material and thickness combination as exemplarily shown for a 100 nm thick CoFeB disk with a diameter of 2 µm (sample CoFeB100) together with their theoretical dispersion curves in Fig. 5.5. The theoretical curves were calculated with the same model as for the trilayers. The parameters found from the manual fit are a saturation magnetization of $M_s = 1050\,\mathrm{kA/m}$, an exchange constant of $A = 18\,\mathrm{pJ/m}$ and a uniaxial anisotropy of $K_u = 200\,\mathrm{J/m^3}$.

The experimental results show that, with TR-STXM, spin waves of the first higher order mode of the Damon Eshbach geometry, which exhibits an inhomogeneous precession profile comprising a node over the film thickness [9], were measured in a frequency range from 9.1 GHz to 17.1 GHz with wavevectors of 19.7 rad/µm to 77.2 rad/µm. This corresponds to wavelengths down to 81 nm ± 40 nm. For frequencies from 16.3 GHz to 20.3 GHz with wavevectors of 5.0 rad/µm to 21.4 rad/µm, spin waves of the standard quasi-uniform mode were imaged.

The first and second order modes occur at frequencies below the quasi-uniform mode leading to points of avoided crossing at approximately 8 GHz and $k = 1\,\mathrm{rad/µm}$ as well as 14 GHz and $k = 3\,\mathrm{rad/µm}$, respectively. At 22.3 GHz, spin waves with wavevectors of 19.1 rad/µm to 20.8 rad/µm were observed, which correspond to the third higher order mode. One data point cannot be unambiguously attributed to the fundamental quasi-uniform mode or the third higher order mode. Spin waves at 30.3 GHz were observed with a wavevector of 29.6 rad/µm, corresponding to a wavelength of 212 nm ± 53 nm, which fits with the calculated dispersion of the fourth higher order mode.

Exemplary normalised STXM snapshots of three different modes are shown in the top part of the figure with the arrows indicating the corresponding data point.

5.4.2 Thickness Dependence

The influence of the film thickness on the spin-wave modes is shown in Fig. 5.6 for disks with a diameter of 5 µm consisting of NiFe with a thickness of 25 nm (NiFe25), 50 nm (NiFe50) and 100 nm (NiFe100). In Fig. 5.6a, the calculated and measured spin-wave dispersions in the Damon-Eshbach geometry are shown for the 25 nm thick film. The parameters found from the fit are a thickness of 30 nm, a saturation magnetization of $M_s = 800\,\mathrm{kA/m}$, an exchange constant of $A = 6\,\mathrm{pJ/m}$ and a uniaxial anisotropy of $K_u = 200\,\mathrm{J/m^3}$. In the considered frequency range from 0 GHz to 20 GHz, only the quasi-uniform and first higher order mode exist. In the STXM experiments, only spin waves belonging to the standard quasi-uniform mode were observed for frequencies from approximately 6 GHz to 13 GHz with wavevectors from 6.0 rad/µm to 17.5 rad/µm.

For a doubled film thickness of 50 nm, the higher order modes shift towards lower frequencies as can be seen for the calculated dispersion relations (Fig. 5.6b). The parameters determined from the manual fit of the experimental data are a thickness of 50 nm, a saturation magnetization of $M_s = 800\,\mathrm{kA/m}$, an exchange constant of $A = 6\,\mathrm{pJ/m}$ and a uniaxial anisotropy of $K_u = 350\,\mathrm{J/m^3}$. The higher order modes shift partially below the quasi-uniform mode, which leads to an avoided crossing between the quasi uniform and first higher order mode at approximately 9.5 GHz and $k = 3.5\,\mathrm{rad/\mu m}$. Experimentally, spin waves corresponding to both modes were observed. For the quasi-uniform Damon-Eshbach mode, they are located at wavevectors between 1.7 rad/µm and 36.2 rad/µm corresponding to frequencies ranging from 7.1 GHz to 17.1 GHz. The spin waves belonging to the first higher order mode occurred at frequencies from 10.1 GHz to 12.1 GHz with wavevectors of 53.2 rad/µm to 61.9 rad/µm. The latter corresponds to wavelengths down to 102 nm ± 30 nm.

When the film thickness is doubled again to 100 nm, modes of even higher order appear in the considered frequency range in the calculations, as all higher order modes shift towards lower frequencies (Fig. 5.6c). The sample parameters determined from the manual fit are a thickness of 100 nm, a saturation magnetization of $M_s = 800\,\mathrm{kA/m}$, an exchange constant of $A = 5\,\mathrm{pJ/m}$ and a uniaxial anisotropy of $K_u = 5\,\mathrm{J/m^3}$. The shift of the modes leads to more points of avoided crossing between the quasi-uniform mode and the modes of higher order. These are located at approximately 3.4 GHz and $k = 0.5\,\mathrm{rad/\mu m}$ for the first, at 6.8 GHz and $k = 1.0\,\mathrm{rad/\mu m}$ for the second, at 10.4 GHz and $k = 3.5\,\mathrm{rad/\mu m}$ for the third and at 14.6 GHz and $k = 13.0\,\mathrm{rad/\mu m}$ for the fourth higher order mode. For the experimentally observed spin waves with low wavevectors from 2.7 rad/µm to 22.7 rad/µm at frequencies from 10.1 GHz to 15.1 GHz, some experimental data points cannot unambiguously be attributed to the quasi uniform, third or fourth higher order mode in the vicinity of avoided crossing. However, in the short-wavelength regime, the waves belonging to the first higher order mode can be clearly identified in a frequency range from 5.1 GHz to 9.1 GHz with wavevectors from 33.5 rad/µm to 93.4 rad/µm. This means that spin waves with wavelengths down to 67 nm ± 20 nm were measured.

These measurements and calculations demonstrate that for thinner films with a stronger vertical confinement, the higher order spin-wave modes appear at higher frequencies. When the film thickness is increased, the frequency of these modes decreases. At the same time, the fundamental quasi-uniform spin-wave mode is only mildly affected by the film thickness.

While an influence of the sample thickness on the anisotropy can be expected, the discrepancy of the values for different NiFe samples could also be because the samples were fabricated at different times. The low values for the exchange constant are in line with earlier findings, as mentioned above.

A comparison between Figs. 5.5 and 5.6c additionally illustrates the influence of different materials on the dispersion relations. For CoFeB, which has a higher saturation magnetization and, more importantly, a higher exchange constant than NiFe, higher order spin-wave modes appear at higher frequencies in the TR-STXM measurements, as supported by the calculations.

5.4.3 Influence of a Magnetic Bias Field

One possibility to alter and control the dispersion relation for a given material and thickness is by applying a static magnetic bias field to the sample. As shown in Chapter 4, small magnetic bias fields lead to the displacement and expansion of the vortex core without influencing the dispersion relation of the emitted spin waves. However, the application of a larger magnetic field of 250 mT in the film plane expels the vortex from the disk and leads to a single-domain state of quasi-uniform magnetic orientation. In this case, the excited spin waves at similar wavelengths appear at higher frequencies compared to the vortex state without any magnetic bias field applied as shown in Fig. 5.7 for 50 nm thick CoFeB disks (samples CoFeB50a and CoFeB50b for measurements without and with a field, respectively). The structures are an ellipse with dimensions of 7.5 µm × 5 µm for sample CoFeB50a and a disk with a diameter of 3 µm for sample CoFeB50b. For the highest wavevector of the experimentally observed spin waves of approximately 9.5 rad/µm the difference between no field applied and the application of 250 mT corresponds to a change in frequency from 16.1 GHz to 25.1 GHz. The calculations indicate that this increase in frequency occurs for both the fundamental and first higher order modes. The parameters found from the fit are a thickness of 50 nm, a saturation magnetization of $M_s = 1100\,\mathrm{kA/m}$, an exchange constant of $A = 15\,\mathrm{pJ/m}$ and a uniaxial anisotropy of $K_u = 5\,\mathrm{J/m^3}$ for sample CoFeB50a and a thickness of 42.5 nm, a saturation magnetization of $M_s = 1200\,\mathrm{kA/m}$, an exchange constant of $A = 15\,\mathrm{pJ/m}$ and a uniaxial anisotropy of $K_u = 25\,\mathrm{J/m^3}$ for sample CoFeB50b. The reduced thickness of sample CoFeB50b presumably comes from the reduced sputter rate onto the back of the membrane as explained earlier. From the calculated dispersion curves, it can additionally be seen that their slopes become less steep when a magnetic field is applied. This coincides with a shift in the ferromagnetic resonance ($k = 0$) from approximately 1 GHz for 0 mT to 19 GHz for 250 mT. To the right hand side of the dispersion, exemplary normalised TR-STXM snapshots are shown of the quasi-uniform mode for the cases with and without the magnetic field applied.

5.5 Conclusions

It was demonstrated that TR-STXM is able to image spin-wave dynamics up to 30 GHz and with wavelengths down to 70 nm by using a low-alpha optics synchrotron operation mode with an increased time resolution. This provides a means to measure spin waves in a frequency and wavelength range that is not accessible by other measurements methods. Several spin-wave modes were imaged in patterned disks of both coupled ferromagnetic bilayers with antiparallel alignment and single ferromagnetic layers. For coupled ferromagnetic bilayers, it was shown that the collective acoustic modes for local antiparallel magnetization orientation are identical, regardless of the vortex circulation states of the disk element. The frequency range of the experiments was extended compared to previous measurements and acoustic modes of both the short- and long-wavelength branch, as well as an instance of an optical mode, were observed. In single ferromagnetic layer systems, it was demonstrated that spin waves of the standard quasi-uniform precession mode as well as of modes of higher order in the Damon-Eshbach geometry can be imaged. Due to the extended frequency range, spin waves up to the fourth order were observed. Furthermore, it was shown how the dispersion relations in single-layer systems can be tuned by the material properties, tuning the film thickness and applying a magnetic field. For both sample systems, it was confirmed that the theoretical predictions are valid even in this extended frequency range. These measurements demonstrate that, by introducing precession nodes over the sample thickness, the frequencies of spin-wave dynamics in ferromagnetic systems can be significantly increased.

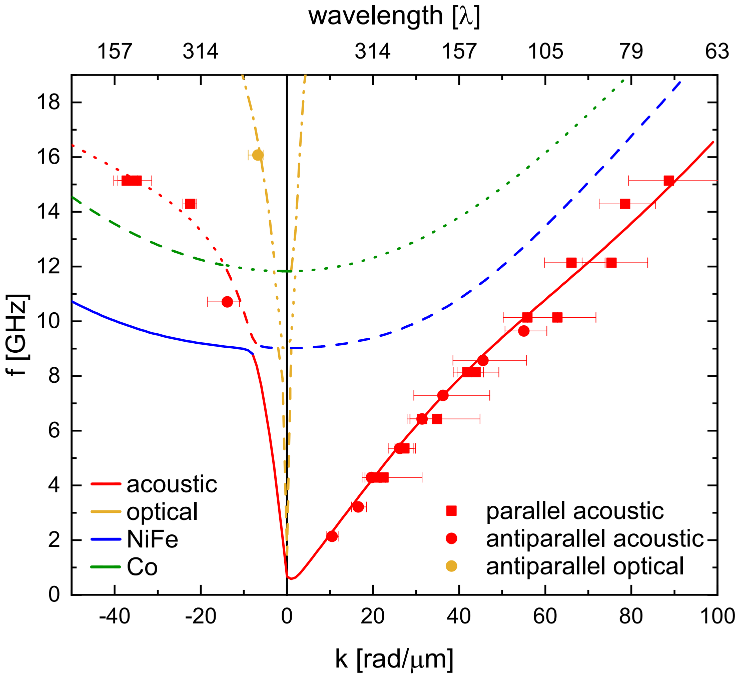

Figure 5.4: Spin-wave dispersions $f(k)$ of the Damon-Eshbach geometry in the Co/Cu/NiFe sample with antiparallel ferromagnetic layers. Experimental data points from TR-STXM of the disk element are shown as dots (antiparallel vortex circulations) and squares (parallel circulations). Red data points correspond to the m_z-acoustic collective mode, while the yellow point is part of the m_z-optical mode. Calculated spin-wave dispersion relations are shown as lines where the colours refer to the characteristic spin-wave modes: m_z-acoustic (red), m_z-optical (yellow), NiFe (blue), Co (green) and the line styles denote the continuous spin-wave bands.

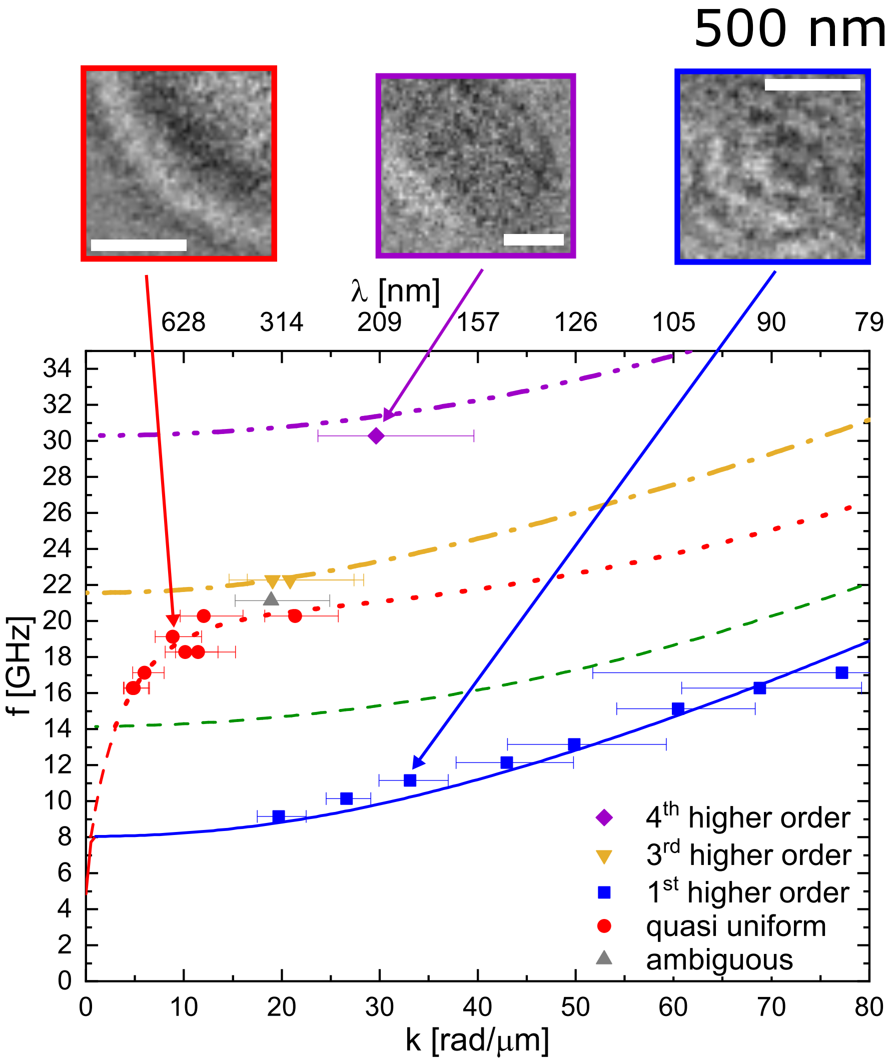

Figure 5.5: Measured and calculated spin-wave dispersion relations in the Damon-Eshbach geometry in a 100 nm thick CoFeB sample. Symbols correspond to experimentally measured data and lines are calculated dispersion curves. The colours denote the spin-wave mode, the line styles denote the spin-wave band. The error bars represent the uncertainty in determining the wavelength. Normalised STXM images are shown of the selected data points indicated by the coloured arrows for different modes.

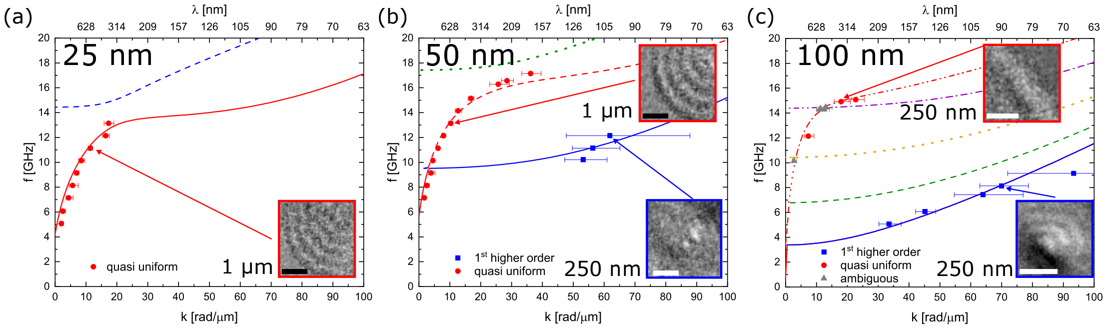

Figure 5.6: Influence of the film thickness on measured and calculated dispersion relations for spin waves in the Damon-Eshbach geometry in NiFe samples. The thicknesses are a) 25 nm, b) 50 nm and c) 100 nm. Symbols correspond to experimentally measured data and lines to calculated dispersion curves. The colours denote the spin-wave mode and the line styles denote the spin-wave band. The error bars represent the uncertainty of the wavelength. Shown in the insets are normalised TR-STXM snapshots of selected data points for different modes as indicated by the arrows.

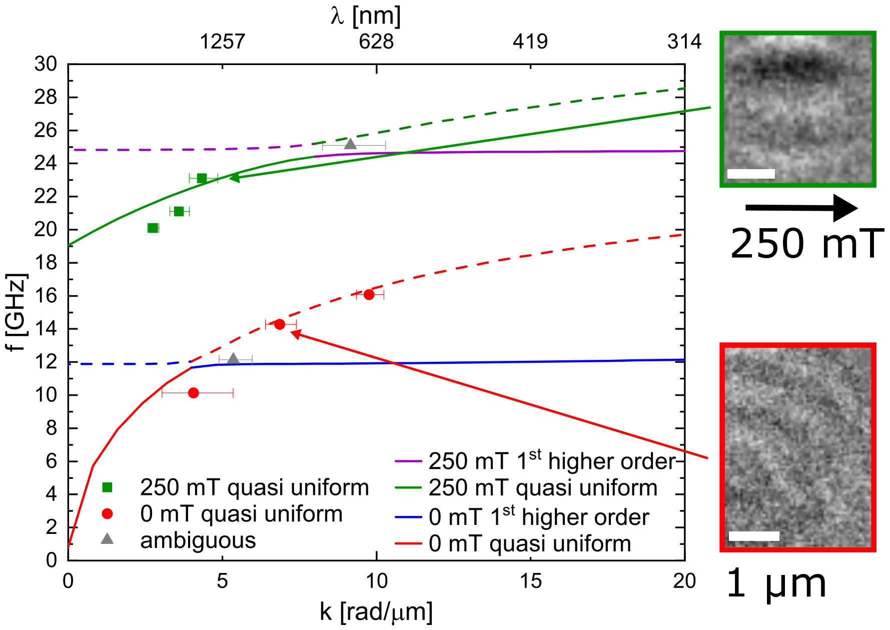

Figure 5.7: Influence of a static magnetic bias field on the measured and calculated dispersion relations in the Damon-Eshbach geometry in 50 nm thick CoFeB samples. Symbols correspond to TR-STXM data and lines to calculated dispersion curves of the quasi uniform and first higher-order mode. The colours denote the spin-wave mode and the line styles denote the spin-wave band. The error bars indicate the uncertainty in determining the wavelength. Normalised snapshots of TR-STXM measurements are depicted with and without the external magnetic bias field applied as indicated by the arrows.

6 Dynamics in Ga-doped YIG

My contribution to the work presented in this chapter is adapting and establishing the Xe PFIB window milling process for the present material in combination with the mechanical grinding, fabricating the actual windows with lapping and PFIB, assisting with the lithography process, participating in the STXM measurements, analysing the experimental data and providing input for the micromagnetic simulations.

Ferrimagnets in many aspects are often treated like ferromagnets with a lower saturation magnetization [16]. The most prominent ferrimagnet in the field of magnonics is yttrium iron garnet ($Y_3Fe_5O_{12}$), typically simply referred to as YIG. It exhibits the lowest known magnetic damping, making it a model system for studying spin-wave dynamics. Spin waves in ferrimagnets, such as YIG, can be seen as a step towards magnonic phenomena in antiferromagnets as ferrimagnets already consist of antiferromagnetically coupled sublattices. Therefore, they also exhibit modes with sublattice canting, which lead to high spin-wave frequencies similar to antiferromagnets. For a better comparison with antiferromagnets, the net magnetization of a ferrimagnet at a certain temperature can be further reduced with some ferrimagnets exhibiting a magnetization compensation. For ferrimagnets that consist of different species of magnetic elements, such as GdCo, the stoichiometry of the material can be changed [8]. For ferrimagnets with a single magnetic element at different crystallographic sites, the material can be doped with a non-ferromagnetic element that preferably occupies the positions of the ferromagnetic element at certain sites. This has been demonstrated for single crystals of YIG, where doping with Ga ions (Ga:YIG) has been used to reduce the net magnetization [128, 129].

In this chapter, different spin-wave phenomena are shown in Ga:YIG thin films, which have a reduced magnetization of approximately 5 % to 20 % when compared with pure YIG. Selected measurements displaying the different effects for exemplary samples are presented. Due to the low magnetization, the observed spin waves are already exchange dominated despite their relatively long wavelengths. This leads to an isotropic emission and propagation of waves. Furthermore, a non-linear excitation effect is observed, which leads to an unprecedented large spin-wave precession angle of more than 20°. These findings are confirmed by micromagnetic simulations. In addition, spin waves in the forward-volume geometry as well as domain-wall and domain dynamics are observed.

6.1 YIG in Magnonics

The insulating ferrimagnet YIG is the material with the lowest known magnon damping, which can be orders of magnitudes lower than that of other materials such as NiFe or CoFeB [130]. The crystalline structure of YIG is shown in Fig. 6.1. The Fe^{3+} ions occupy two different lattice sites with opposite orientations leading to the ferrimagnetic nature of the material [14]. YIG was first synthesised as a bulk crystal in 1957 [131] and its low damping lead to a multitude of experimental investigations into its magnetic resonance and spin-wave behaviour in the following years. These experiments were predominantly performed in spheres, disks and rods polished from single crystals (see e.g. [132–135]).

Since then, the high-quality growth of thin films with thicknesses below 100 nm and damping values of $\alpha = 1 \times 10^{-4}$ has been established [61]. Due to this low damping, which allows the propagation of spin waves over centimetres, YIG is a model system for both fundamental studies as well as applications [17]. For example a Bose-Einstein condensate of magnons at room temperature has been observed in YIG films [136], while on the path towards spin-wave applications, magnon transistors [137], logic elements such as a majority gate [138], and a directional coupler [139], have been demonstrated in YIG thin films. Typical values of magnetic parameters for YIG are a Curie temperature of $T_C = 559\,\mathrm{K}$ [16], a saturation magnetization $M_S = 140\,\mathrm{kA/m}$ to $143\,\mathrm{kA/m}$ [61, 130] and an exchange constant $A = 3.7\,\mathrm{pJ/m}$ [140]. Thin YIG films with thicknesses on the order of 100 nm exhibit an in-plane anisotropy.

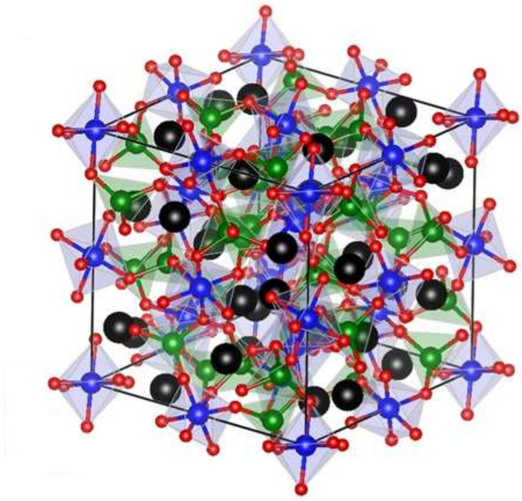

Figure 6.1: Structure of YIG with the majority tetrahedral Fe sites (green), the minority octahedral Fe sites (blue) as well as the Y sites (black) and the O sites (red). Adapted from [17]. Published under CC BY 4.0.

6.2 Sample Fabrication

6.2.1 Growth and Pre-Characterisation

The Ga:YIG thin films with different Ga concentrations were grown by liquid-phase-epitaxy (LPE) by INNOVENT Technologieentwicklung Jena, where the growth of high-quality, low-damping nanometre-thick YIG films had been established [61]. The films were grown on $Gd_3Ga_5O_{12}$ (GGG) wafers with either (100) or (111) orientation. The thickness of the films was determined by means of a prism coupler and the saturation magnetization of the samples was measured using a vibrating-sample magnetometer (VSM) by INNOVENT. From these magnetization measurements it was observed that the anisotropy changed from in-plane, as usual for YIG thin films, to out-of-plane with increasing Ga-doping. Table 6.1 gives an overview of the samples investigated in this project, with their thicknesses, saturation magnetizations as well as the orientation of the GGG substrates. After the thin-film growth and pre-characterisation, the wafers were cut into rectangular and square pieces with side lengths ranging from 2 mm to 5 mm for further processing.

Table 6.1: Overview of the Ga:YIG samples and their properties. The saturation magnetization of all samples is reduced compared to undoped YIG (~ 140 kA/m).

Sample	Thickness [nm]	M_S [kA/m]	GGG orientation
A10	200	31.8	(100)
A14	150	14.0	(100)
6-02	150	<8.0	(111)

6.2.2 Window Fabrication and Lithography

The GGG substrates were 500 µm thick, which means that the samples needed to be thinned for STXM measurements as described in Section 3.3. Because GGG has a relatively fast PFIB milling speed, prior to milling, the samples were lapped to thicknesses of 100 µm and 130 µm. Afterwards, the samples were mechanically polished to obtain a smooth surface. This step is required, as an insufficiently smooth surface can cause unwanted step-like features in the PFIB milling process. After the mechanical processing, windows were milled into the samples with a Xe PFIB. To aid the alignment of the samples for lithography, holes were milled into the samples by PFIB in addition to the windows.

After the windows were fabricated, a stripline was lithographically patterned onto each window on the Ga:YIG film side of the sample. The EBL process utilised lift-off for pattern transfer as described in Section 3.1 with a few adaptations due to the properties of the material. Because Ga:YIG and GGG are highly insulating, a 10 nm thick Al layer was deposited onto the resist by thermal evaporation after the spin coating. These films help to reduce charging effects during the electron beam exposure. The samples were aligned in the electron beam writer using the additionally milled holes, which can be identified by the electron beam. The lateral size of the exposed stripline was 6.5 µm by 500 nm. After the exposure, the Al film was removed by tetramethylammonium hydroxide (TMAH). The samples were subsequently developed in MIBK/IPA for approximately 30 s and rinsed in IPA. Then 200 nm of Cu, together with a 5 nm thick Cr adhesion layer, were deposited for the stripline by thermal evaporation. Finally, the samples were immersed in acetone for lift-off.

6.3 TR-STXM Imaging

6.3.1 Spin Waves

The dynamics in the Ga:YIG samples were imaged using TR-STXM at the Fe L_3 edge with a single circular polarisation. The measurements were performed at the Maxymus beamline at the Bessy II synchrotron.

In Fig. 6.2a, a window in sample A14 is shown as a snapshot of a time-resolved absolute absorption image. The diagonal contrast variation stems from substrate thickness differences due to the ion milling. At a horizontally applied magnetic in-plane field of 169 mT, the sample is saturated in the film plane. In the centre of the image, the stripline is visible as dark horizontal contrast. The white spots are Fe depleted areas in the film as explained in Section 3.3.

When an exemplary ac excitation of 3.57 GHz is applied across the stripline leading to an oscillatory Oersted field of approximately 4 mT, spin waves are locally emitted and propagate away from the source. Their propagation is not noticeably affected by the white Fe depleted areas. Even though the spin waves are already visible in the absolute absorption image, they become even more prominent in the normalized snapshot shown in Fig. 6.2b. The spin waves propagate in an almost radially isotropic manner away from an elliptically shaped source, which forms at the stripline. This means that the dispersion relations for waves in the Damon-Eshbach and backward-volume geometry are rather similar, which is only the case for the exchange-dominated regime.

Intensity profiles taken along the yellow arrow for two snapshots with a time delay of 80 ps confirm that the observed spin waves are propagating (Fig. 6.2c). The wavelength of the spin waves can be determined from the intensity profiles to be 683 nm ± 17 nm. In addition, the intensity profiles confirm the low magnetic damping of the material, as the waves propagate over distances of more than 10 times the wavelength with low loss in amplitude despite their circular wavefronts. After 10 wavelengths, the spin-wave angle is reduced to approximately half its original value. This low damping is confirmed by ferromagnetic resonance measurements, where a damping of $\alpha = 5 \times 10^{-4}$ was found for this sample.

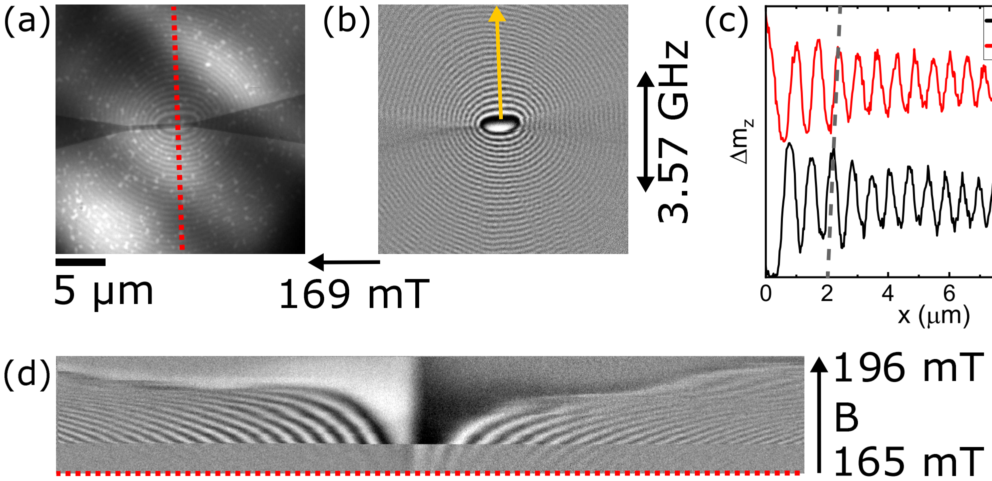

Figure 6.2: Propagating spin waves in Ga:YIG sample A14. a,b) Snapshots of TR-STXM data taken with out-of-plane magnetic sensitivity at an external magnetic in-plane field of 169 mT and an excitation frequency of 3.57 GHz. a) Absolute absorption image depicting the thinned window and the emission of spin waves at the stripline that is visible as dark contrast in the centre. The diagonal variation of contrast stems from gradients in the substrate thickness, while the white spots are Fe depleted areas. b) Normalized view highlighting the emitted spin waves. c) Intensity profiles at different delay times along the yellow arrow in b) confirm the propagating character of the waves, indicated by the dashed grey line. d) Magnetic-field line-scans along the red dashed line in a). The magnetic field is increased by 0.2 mT every time the line is scanned, in the range from 165 mT to 196 mT, showing a spontaneous increase in contrast above a magnetic field of approximately 173 mT.

To study the effect of the static magnetic field on the spin waves, magnetic field line scans were performed. For this, instead of taking a two-dimensional image, only a one-dimensional line is scanned repeatedly, the position of which is indicated by the red dashed line in Figure 6.2a. For each line scan, the magnetic field is increased, here from 165 mT to 196 mT in steps of 0.2 mT, as depicted in Figure 6.2d. While spin waves are already visible in the lower part, corresponding to lower magnetic fields, a spontaneous substantial increase in contrast appears at a magnetic field of approximately 173 mT. The change of contrast coincides with a phase jump of the emitted spin waves, which is visible in Fig. 6.2d at the stripline where, for the low-field region, there is a dark contrast to the left hand side of the stripline and a bright contrast towards the right hand side, which inverts as the contrast increases. The spontaneaous increase in contrast appears at 173 mT in the magnetic field line scan, whereas the images in Figures 6.2a and 6.2b show the increased contrast at a lower magnetic field of 169 mT. This is due to an amplitude hysteresis, meaning that this non-linear excitation effect persists to lower magnetic fields if the field is decreased instead of increased.

A strong contrast means that there is a large spin-wave precession angle. This angle, i.e. here the magnetization tilt out of the film plane, can be calculated by comparing the contrast of the waves with static images of the fully saturated out-of-plane state. The angles are found to exceed 20° close to the centre of the emission, which is significantly higher than usual spin-wave angles which are on the order of 1° as found, for example, in permalloy [141].

To gain a better understanding of this non-linear excitation effect that leads to such large spin-wave angles, micromagnetic simulations were performed with Mumax3. A snapshot of the simulated images is depicted in Figure 6.3. The size of the simulations was chosen to be similar to the experimental image (25 µm × 25 µm) with 512 × 512 × 1 cells with a cell size of 50 nm × 50 nm × 150 nm. A saturation magnetization similar to that of the sample of 15 kA/m and uniaxial anisotropy in the z-direction (out-of-plane) of 950 J/m^3 was used. The anisotropy was determined from the saturation magnetization and the magnetic field that is needed to turn the magnetization into the film plane. A fit to the wavelength observed in the experiment leads to an exchange constant of $A = 0.9\,\mathrm{pJ/m}$, which is approximately a quarter of the one of undoped YIG. The damping constant of $\alpha = 5\times10^{-4}$ was increased at the edges to prevent reflections of spin waves due to the finite simulation size. An ac current with a frequency of 3.57 GHz and with a maximum current of $J = 3.8\,\mathrm{mA}$ was used to excite the spin waves. The localisation of the spin-wave emission at the right hand side of the stripline is achieved by a small diagonal variation of the saturation magnetization, which resembles the thickness gradient of the substrate. This thickness variation of the substrate is suspected to lead to a small variation of the temperature of the sample leading to a slight change in the saturation magnetization. From the simulation parameters an exchange length of $l_{ex} = 80\,\mathrm{nm}$ can be calculated, which confirms the experimental finding that the observed spin waves with wavelengths on the order of 700 nm are exchange dominated.

The simulations confirm the excitation non-linearity observed in the experiments, which also coincides with a phase shift of 180° of the spin-wave emission. An analysis of the amplitude of the oscillation yields spin-wave angles of up to 40°, exceeding even those measured experimentally. Furthermore, the hysteresis in the magnetic field of the onset of this non-linear effect was confirmed. Similar hysteresis effects were also found for both the excitation amplitude and frequency. This suggests that the observed effect is similar to a Duffing oscillator, where amplitude jumps occur due to a bistable non-linear frequency response, as recently observed in similar Ga:YIG films [142]. The foldover accompanying such a bistable behaviour can lead to an abrupt increase in the spin-wave amplitude. Such non-linear effects typically occur for high excitation amplitudes [143, 144]. However, the detailed reasons and prerequisites for such giant spin-wave excitation angles need to be further investigated.

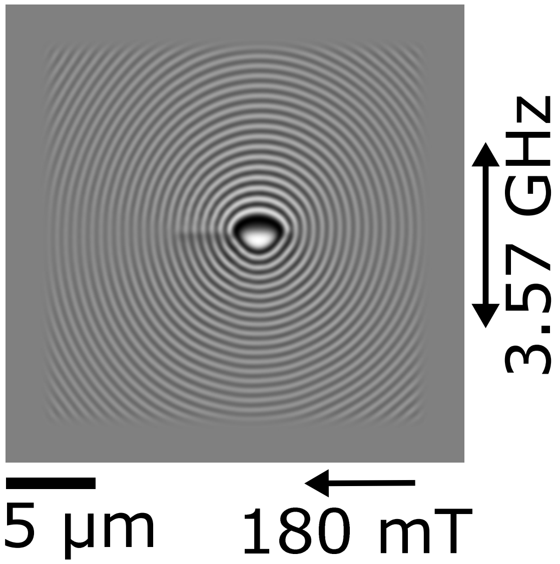

Figure 6.3: Micromagnetic simulation depicting high-amplitude spin waves similar to those observed in the experiment at an external magnetic in-plane field of 180 mT and an excitation frequency of 3.57 GHz.

It can be observed in the experiment (Fig. 6.2d) that the wavelength, i.e. the dispersion relation, is not substantially affected by the nonlinear increase in contrast and, hence, the spin-wave angle, which is confirmed by the micromagnetic simulations. Therefore, calculated dispersion relations should be valid in the entire observed range.

Sample 6-02, which has the highest doping of all investigated samples and exhibits a compensation point slightly below room temperature, has a stronger out-of-plane anisotropy than sample A14. Therefore, the available magnetic field of 250 mT is not sufficient to tilt the magnetization in-plane at room temperature, whereas this is possible for higher temperatures. However, no increased spin-wave angles or other non-linearities were observed in this sample. Instead of tilting the magnetization in-plane, it was attempted to excite forward-volume waves where the magnetization is perpendicular to the film. To be able to image such waves with circular light, the sample was mounted with an angle of 30° between the surface normal and the photon beam, which is typically used for sensitivity to the in-plane component of the magnetization. However, no spin waves were emitted and only a driven oscillation is visible at the stripline, as shown in Fig. 6.4a for an exemplary excitation of 10.07 GHz with a magnetic field of 50 mT applied out-of-plane at 50 K. To verify the validity of the set-up, sample A14 was mounted at a tilt angle and a magnetic field of 30 mT applied mainly perpendicular to the sample plane. Due to geometric restrictions from the milling, the sample could not be mounted at the standard 30° but only at approximately 25°. The response of the sample to a dynamic excitation with a frequency of 3.57 GHz is shown in Fig. 6.4b. Propagating spin waves with a wavelength of 600 nm ± 67 nm were observed. This confirms that, in general, forward-volume spin waves can be excited in the Ga:YIG samples and that it is possible to measure such waves with circularly polarised x-rays. The reason why no spin waves in the forward-volume geometry were observed in sample 6-02 is possibly a strong damping that also hindered the long propagation of spin waves for the in-plane magnetized state.

6.3.2 Domain and Domain-Wall Dynamics

In addition to the previously shown spin waves in fully saturated single-domain states, dynamics are also observed in the presence of domains. To stabilise a domain wall between inclined domains, an in-plane magnetic field of 100 mT was applied to sample A14. This can be seen in the absolute absorption images in the top row of Fig. 6.5a and b, where a domain wall separates regions of bright and dark contrast with opposite magnetization directions towards the left and right hand side, respectively. When an excitation with a frequency of 118 MHz is applied through the stripline, the domain changes its size (Fig. 6.5a). This can be especially observed in the normalised view, where regions of domain expansion and shrinkage correspond to the areas with black and white contrast within the grey area. At an excitation frequency of 265 MHz, the size change is restricted to the domain wall that leads to an oscillatory motion of the domain wall, which propagates along the wall as shown in Figure 6.5b.

In Ga:YIG sample A10, which already exhibits a domain structure at fields close to remanence, here with a nominal out-of-plane magnetic field of 3 mT, it can be seen that stripe domains are stabilised as seen in the absolute image in Figure 6.5c. Dynamics in the domain walls can be excited at a frequency of 71 MHz, which can be seen in the normalised snapshot. These domain wall dynamics occur at much lower frequencies compared to the spin waves within the domains.

6.4 Conclusions

It was shown that high-quality YIG films can be doped with Ga to reduce their saturation magnetization to reach compensation. For moderate doping, the samples exhibit

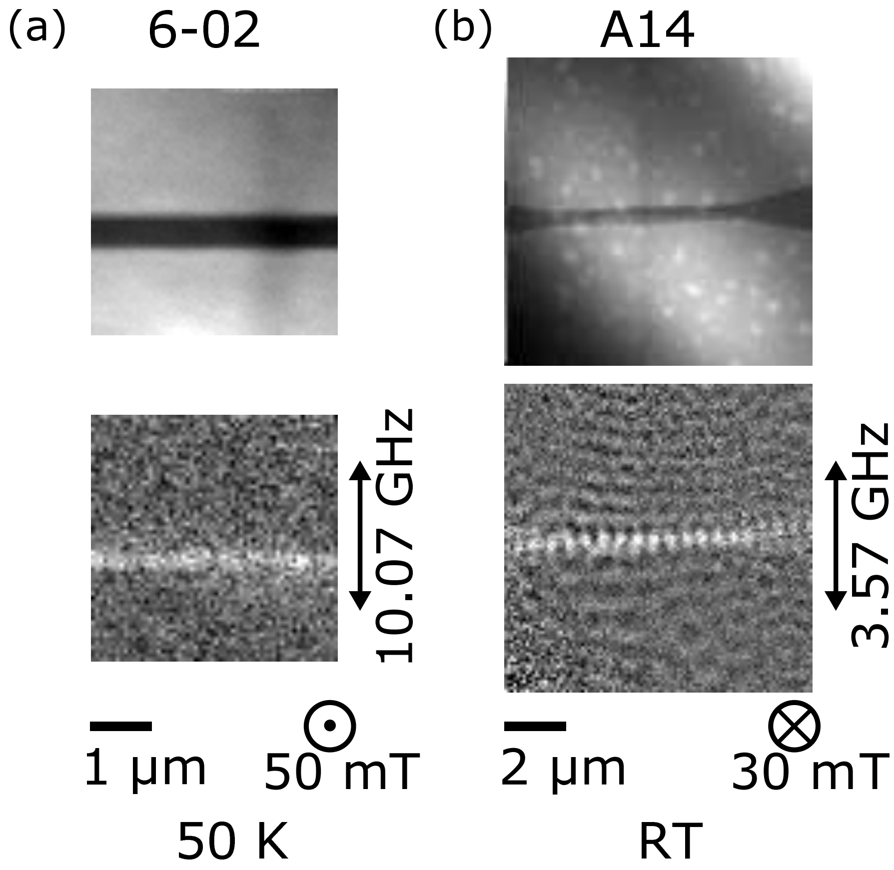

Figure 6.4: Spin waves in the forward-volume geometry. Absolute (top row) and normalised (bottom row) STXM images taken with the sample normal at an angle of approximately 30° to the photon beam. a) Driven oscillation under the stripline in sample A-02 at an external magnetic out-of-plane field of 50 mT and an excitation frequency of 10.07 GHz at 50 K. b) Spin waves emitted in sample A14 at an external magnetic out-of-plane field of 30 mT and an excitation frequency of 3.57 GHz at room temperature (RT).

the characteristic low damping of YIG with long spin-wave propagation lengths, whereas only short propagation lengths were observed for the sample with the highest doping. The low magnetization leads to an exchange length on the order of 80 nm in sample A14, which means that the observed spin waves with wavelengths of several hundreds of nm are exchange dominated, which manifests as an isotropic emission and propagation of the waves. A non-linear effect in the excitation can lead to unprecedented large spin-wave amplitudes exceeding 20°, which coincide with a phase jump of the emitted spin waves. Micromagnetic simulations reproduce and confirm these effects. Furthermore, spin waves in the forward-volume geometry were observed as well as domain and domain-wall dynamics. Despite the need for detailed calculations and additional sys-

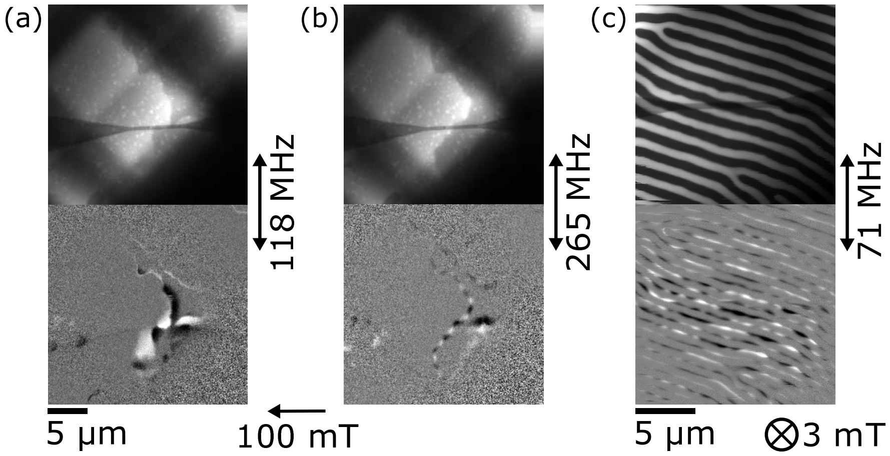

Figure 6.5: Domain and Domain-wall dynamics at low frequencies. Snapshots of TR-STXM data taken with out-of-plane sensitivity. The top row shows absolute absorption images, the bottom row the normalized view. a,b) Dynamics in sample A14 at an external magnetic in-plane field of 100 mT. a) At an excitation frequency of 118 MHz the entire domain is changing its size. b) At an excitation with a higher frequency of 265 MHz, a directional oscillatory motion of the domain wall is visible. c) Dynamics in sample A10 at an external magnetic out-of-plane field of 3 mT. The sample hosts stripe domains as visible in the absolute absorption image. An excitation frequency of 71 MHz leads to a directional oscillatory motion along the domain walls.

tematic experiments to fully understand the system, the results show that, by reducing the magnetization of a ferrimagnet, a rich dynamic behaviour can be excited.

7 Imaging of Spin Waves in Antiferromagnetic Hematite

My contribution to the work presented in this chapter is the adaptation of the Xe PFIB window milling process with a F_2 *precursor gas, the actual fabrication of the window, assistance with the lithography process, participation in the STXM measurements and analysis of the experimental data.*

Despite having been discovered more than 70 years ago and already being used as a passive element in technologically relevant devices, such as read-heads of computer hard drives, antiferromagnets as an active part in magnetic systems have only recently become a focus of research. The reasons for this include the fact that antiferromagnets are stable towards moderate external magnetic fields and do not produce magnetic stray fields themselves. This means that antiferromagnets are insensitive to magnetic perturbations and cross-talk with neighbouring magnetic devices. However, this makes it not only difficult to manipulate the state of an antiferromagnet but to read it out or measure it [3]. The main advantage over ferromagnetic systems with respect to magnonics are the expected fast antiferromagnetic dynamics, where even the fundamental resonances are governed by the exchange interaction, which facilitates an increase of the computational speed of future magnonic devices [2].

Hematite (α-Fe_2O_3) has long been known as an antiferromagnet (AFM), which has no net magnetization at low temperatures. At higher temperatures above the so-called Morin temperature T_M [145], but below the Néel temperature T_N, there is nevertheless a small magnetic moment, the origin of which was controversly discussed [146, 147]. Sample defects and even parasitic influences from Fe_3O_4 (magnetite) defects were considered as a source [146]. However, this controversy eventually led to the discovery of the Dzyaloshinsky-Moriya interaction (DMI) [18, 19], whose influence leads to a slight canting of the antiferromagnetically ordered moments. This means that hematite is a canted AFM in this phase. The occurrence of these two different antiferromagnetic phases that are accessible by varying the temperature also makes hematite a model system to study different antiferromagnetic behaviours in a single material.

In this chapter, it is described how hematite is imaged using TR-STXM. For this, x-ray transparent windows were milled into a bulk single crystal of hematite using a revised adaptation of the Xe PFIB milling technique described in Section 3.3. It is shown that the spin reorientation at the Morin temperature can be observed in this sample using the XMLD effect. This reorientation is found to be non-uniform over the visible sample region, presumably due to a gradient in the sample thickness. Furthermore, at room temperature in the canted antiferromagnetic state, antiferromagnetic dynamics can be coherently excited. The observed spin waves propagate at frequencies of approximately 20 GHz to 25 GHz.

7.1 Properties of Hematite

Hematite crystallises in a hexagonal structure as schematically depicted in Figure 7.1. It is antiferromagnetic with a Néel temperature of 948 K, above which it is paramagnetic [147]. A special property of hematite is that it has two different antiferromagnetic phases. Above the Morin temperature T_M, which typically occurs between 250 K and 263 K[145, 148, 149], the magnetic moments lie in the plane of the hexagonal structure, which is referred to as the C-plane (see Figure 7.1a). Due to the DMI that points along the c-axis, the two sublattices cant with an angle of less than $0.1°$ within the C-plane, leading to a small net magnetization and making it a canted AFM [149]. Below T_M, the moments are aligned perpendicular to the C-plane, i.e. along the c-axis as shown in Fig. 7.1b. In this configuration, hematite is fully antiferromagnetic with no remanent net magnetization. This spin reorientation at the Morin temperature is caused by a change of sign of the anisotropy field [150]. Hematite can be classified as an easy-plane AFM above T_M and as an easy-axis AFM below it [151]. The value of the Morin temperature can depend on the sample size and crystal quality. Therefore often thin films do not have a spin reorientation and are in the easy-plane state at all temperatures [152, 153], whereas it is possible to have a Morin transition for sufficiently thick films [12].

Calculations of the antiferromagnetic resonance (AFMR) show the existence of a low-frequency and a high-frequency mode, which correspond to a precession around and a vibration along the applied magnetic field, respectively [155]. The low-frequency mode is found at a frequency of approximately 11 GHz at room temperature at remanence [149]. In addition, this mode is reported to exhibit a low magnetic damping on the order of $\alpha = 10^{-5}$ at room temperature that is the same order of magnitude as for YIG [148], which is the material with the lowest reported magnon damping.

7.2 Sample Fabrication

A double-side polished, naturally sourced hematite single crystal with a crystal cut along the C-plane was purchased from Surface Net GmbH. The sample has a lateral

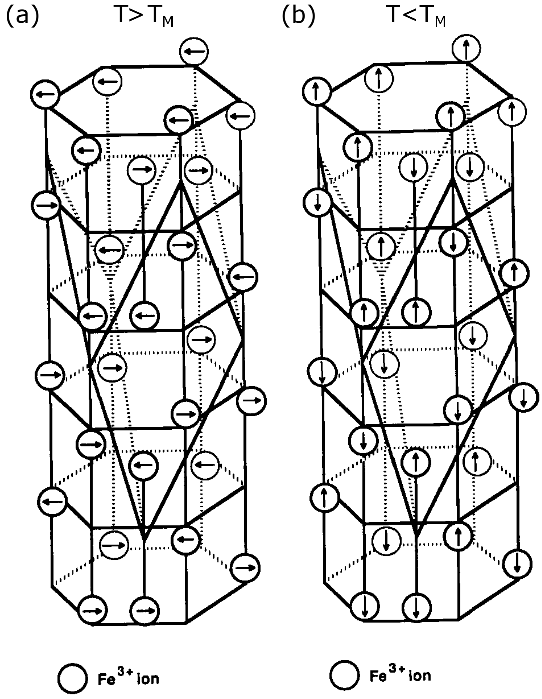

Figure 7.1: Structure of hematite. The arrows represent the magnetic moments of the Fe^{3+} ions. a) Magnetic structure above the Morin transition in the canted antiferromagnetic phase with the magnetic moments in the C-plane. b) Structure below the Morin transition in the purely antiferromagnetic phase with the magnetic moments pointing along the c-axis. Adapted from [154] with permission from Elsevier.

size of 5 mm × 5 mm and a thickness of 100 µm, which means that it could be directly processed with the PFIB as described in Section 3.3 without any mechanical grinding. However, it was found that standard Xe PFIB milling as used previously led to a non-even surface with steps and holes (see Fig. 7.2a). It was found that the use of a F_2 precursor gas during the milling leads to an even surface with smoothed out edges as shown in Figure 7.2b. Nevertheless, after being exposed to air, the window oxidised further, which led to its collapse as depicted in Fig. 7.2c. To prevent such oxidation, a thin layer (5 nm to 10 nm) of C was deposited in situ on the next window, directly after milling, with the use of a C precursor gas and electron deposition. This deposition was performed under different angles to cover the bottom as well as the sides of the window. After taking out the sample from the PFIB, it was immediately transferred to an evaporator, where additionally 20 nm of C were deposited. This combination of deposition processes prevented the oxidation and the window remained intact (Fig. 7.3a). To enable the alignment of the samples in the lithography step, one hole was milled in addition to the window without the precursor gas.

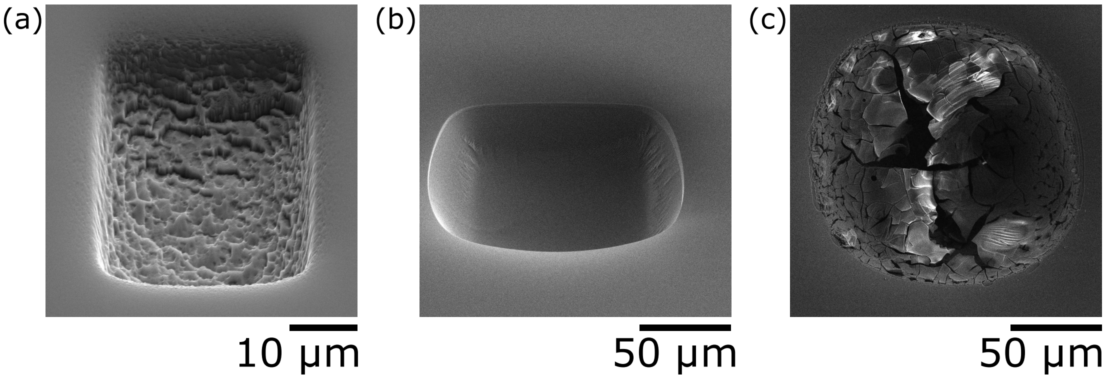

Figure 7.2: SEM images of windows milled into hematite. a) Window milled without the use of the F_2 precursor gas, taken at an electron energy of 15 kV with a stage tilt of 55°. b) Window milled with the F_2 precursor gas, taken at an electron energy of 15 kV with a stage tilt of 55°. c) Collapsed window due to oxidation, taken at an electron energy of 10 kV with a stage tilt of 0°.

Unlike the samples described in the previous chapters, the hematite is a bulk single crystal and not a thin film on a substrate. This means that the Xe^+ ions directly penetrate into the material of interest and may damage it. To minimise these effects, the acceleration voltage of the ions was decreased from 30 kV to 10 kV and eventually 5 kV towards the end of the milling process. This reduces the ion penetration depth from a mean range of 12 nm to 4 nm with no ions penetrating further than 10 nm according to Monte-Carlo simulations performed with the SRIM software package [91].

The fact that a single crystal is investigated, means that the thickness of the material is not constant after the milling. This thickness is determined by STXM measurements. Figure 7.3b shows the milled window at an x-ray energy of 1150 eV. The dark contrast stems from a lithographically patterned coplanar waveguide (see below). The thickness was determined by the use of the Beer-Lambert law and comparing the incident and transmitted beam intensities, using a similar method to that reported in Section 3.3. Hematite has a density of 5.26 g/cm^3 [156], which corresponds to an absorption length λ of 0.347 µm at 1150 eV [90]. The incident beam intensity I_0 is measured via an additionally milled alignment hole. In the thinnest region, indicated by the blue circle in Fig. 7.3b, a thickness of 305 nm was found. Several micrometres away, in the green dotted circle, the thickness is determined to be 580 nm. This difference indicates a moderate thickness gradient of the milled sample window.

After the window was fabricated, a coplanar waveguide (CPW) was lithographically patterned onto the side of the sample that had not been milled. The EBL process utilised lift-off for pattern transfer as described in 3.1 with a few adaptations due to the properties of the material. In particular, because Fe_2O_3 is insulating, after the spin

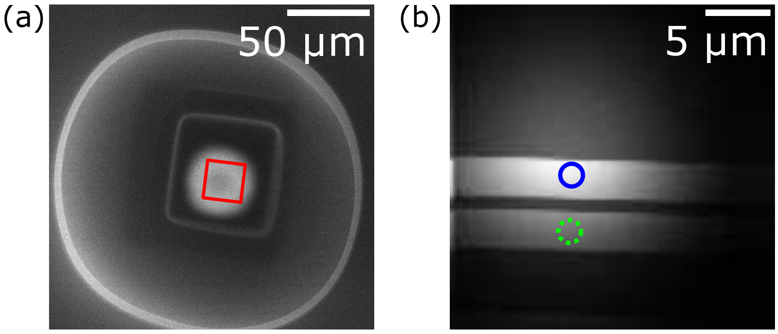

Figure 7.3: a) SEM image of the final window after the C deposition, taken at an electron energy of 30 kV with a stage tilt of 0°. b) STXM image of the window detail indicated by the red square in (a) taken at an x-ray energy of 1150 eV. The blue and green dotted circles indicate the positions of the evaluated thickness of 305 nm and 580 nm, respectively.

coating, a 10 nm thick Al layer was deposited onto the resist by thermal evaporation. This film reduces the charging during the electron beam exposure. The sample was aligned in the electron beam writer by using an additionally milled hole, which can be detected by the electron beam. Then the 70 µm long and 1 µm wide CPW with a 3 µm wide gap was exposed. After the exposure, the Al was removed by tetramethylammonium hydroxide (TMAH) and the sample was subsequently developed in MIBK/IPA for approximately 60 s and then rinsed in IPA. Then 200 nm of Cu for the waveguide, together with a 5 nm thick Cr adhesion layer, were deposited by thermal evaporation.

7.3 Static Imaging in the Vicinity of the Morin Temperature

Due to the thickness of the sample, the measurements were performed at the Fe L_2 edge to ensure sufficient transmission of x-rays. At first, the sample was cooled to below T_M, the temperature, at which a spin reorientation is expected, which for this sample lies between approximately 250 K and 255 K. Then static images were taken with vertically polarised light in the vicinity of T_M, by increasing the sample temperature. The state of the sample window at 253.0 K is depicted in Figure 7.4a. As the sample surface is collinear to the C-plane, the spin axes pointing perpendicular to the sample plane corresponds to the fully AFM phase below T_M whereas the spin axes in the sample plane corresponds to the canted AFM phase above T_M. As the sample region below the CPW has a different thermal behaviour due to its contact with the conductor, the following focuses on the region in between the CPW lines as indicated by the red rectangle in Figure 7.4. A region of dark contrast is visible in the centre, next to an area with bright contrast. From images with different orientations of the linearly polarised x-rays and at different temperatures, it can be inferred that the dark contrast corresponds to the region above T_M, where the magnetic moments are oriented in the sample plane. At the same time, the bright contrast corresponds to the sample being in the easy-axis state with the spin axis perpendicular to the sample plane below T_M. These results show that T_M varies across the sample as it is influenced by local sample properties such as the thickness. When the temperature is increased to 253.6 K, the area of dark contrast expands (Fig. 7.4b). With a further increase in temperature to 253.8 K, the dark region expands to cover almost the whole sample window (Fig. 7.4c).

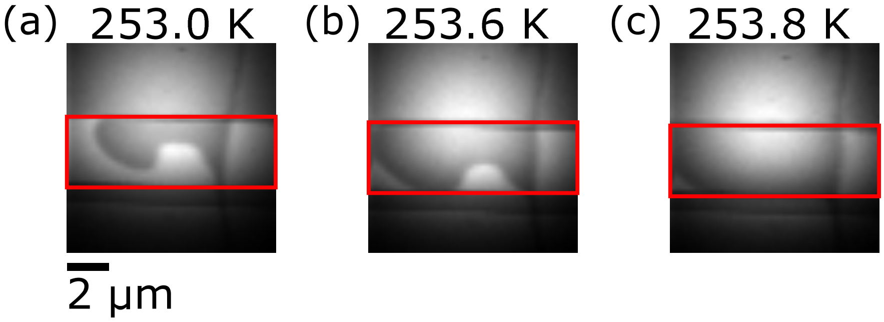

Figure 7.4: Static STXM images in the vicinity of the Morin temperature acquired with linear vertical light. The red rectangles indicate the region of interest between the CPW lines. (a) Image taken at 253.0 K. The bright contrast is the region with magnetic moments pointing out of the film plane, which corresponds to the easy-axis state below the Morin temperature. The dark contrast is the area that has transitioned to the canted antiferromagnetic state, meaning the magnetic moments are oriented in the plane. (b) With an increase in temperature to 253.6 K, the area of dark contrast expands. (c) At 253.8 K, the darker area expands further, covering almost the whole visible sample region.

It has to be noted that the temperature is measured by an adjacent Si diode attached to the sample holder and, therefore, is not measured at the exact sample position. Therefore, the nominally measured temperature is not accurate and potentially lower than the actual sample temperature. Especially when the temperature is changed, it may take time until the sample temperature is the same as the sensor temperature. When an excitation is applied to the sample, the additional heat has to be taken into account. Therefore, for dynamic measurements at T_M, the temperature is stabilised with the excitation turned on.

7.4 Dynamics at Room Temperature

In order to image dynamic effects at frequencies exceeding 10 GHz, the measurements were performed in the low-alpha operation mode of the Bessy II synchrotron. At room temperature, the sample is in the canted antiferromagnetic state. Shown in Fig. 7.5a is the window region at the Fe L_2 absorption edge imaged with circularly polarised x-rays. The horizontal lines of dark contrast correspond to the central conductor (bottom part of the image) and one of the ground lines (top part of the image) of the CPW. A static magnetic field of 180 mT is applied out of the sample plane. Then an RF current with 20.07 GHz frequency is sent through the central conductor of the CPW, leading to oscillating magnetic Oersted fields on the order of 1 mT, which is calculated from the measured output power. These fields excite spin waves that propagate away from the central conductor towards the direction of the ground line as seen in the normalised view in Fig. 7.5b. The imaging of the dynamics with circularly polarised x-rays is enabled by the dynamical sublattice canting of the antiferromagnet, which can be probed. To highlight the propagating character of the antiferromagnetic spin waves, intensity profiles were taken along the yellow arrow in Fig. 7.5b at three different times as shown in Fig. 7.5c. From these profiles, the wavelengths of the spin waves can be determined to be 1.92 µm ± 0.17 µm, which corresponds to a phase velocity $v_p = 38.53$ km/s. The value for the phase velocity agrees well with neutron scattering experiments that report velocities of $v = 31$ km/s [157] to $v = 38$ km/s [158] for hematite below and above T_M, respectively. At a frequency of 20 GHz, the measured wavelength, which corresponds to a wavevector of approximately $k = 3$ rad/µm, is in agreement with calculated dispersion relations above the Morin temperature based on a phase velocity of $v_{ph} = 50$ km/s [148]. The measurements presented here also confirm that it is possible to directly image antiferromagnetic spin waves in hematite.

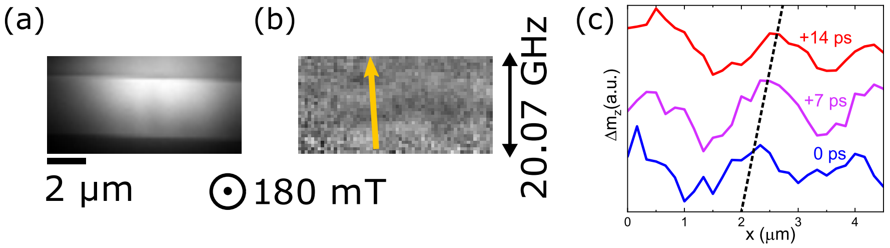

Figure 7.5: Spin-wave dynamics in hematite at room temperature (a,b) TR-STXM taken with circularly right polarised light displaying the response of the sample to an alternating field excitation of 20.07 GHz frequency with an out-of-plane static magnetic field of 180 mT applied. (a) Absolute absorption image. The dark horizontal contrasts originate from the CPW. (b) Normalized snapshot image showing only the temporal changes with respect to the average state, displaying the spin waves. (c) Intensity profiles along the yellow arrow in (b) at a relative time delay of 7 ps illustrating wave propagation as indicated by the dashed line.

In addition to the external field applied perpendicular to the sample plane, spin waves can be excited for fields with in-plane orientation. This is demonstrated for an external field of 100 mT in Fig. 7.6a and an excitation of 19.07 GHz. The wavelength of the resulting spin waves is determined to be 2.83 µm ± 0.33 µm in this case, which corresponds to a phase velocity of $v_p = 53.97\,\mathrm{km/s}$. At an in-plane field of 220 mT and a driving frequency of 26.14 GHz, propagating spin waves with a wavelength of 2.50 µm ± 0.33 µm and a phase velocity of $v_p = 65.35\,\mathrm{km/s}$ are observed (Fig. 7.6b). The fact that these dynamics with varying wavelengths occur at different magnetic fields and excitation frequencies shows that the dynamics in a canted antiferromagnet such as hematite can be influenced both by the external magnetic field and the driving frequency, as expected.

It can be seen that the dynamics in Fig. 7.6a is primarily located at the left hand side of the window, while the dynamics in Fig. 7.6b occur mainly on the right hand side of the visible window as indicated by the yellow dashed circles. This different behaviour could be caused by the different thicknesses, thickness gradients, a resulting temperature gradient or by other structural or magnetic inhomogeneities in the sample. However, as depicted by the images acquired with linear horizontal (LH) and vertical (LV) x-rays in FIg. 7.6c, no magnetic features are visible.

7.5 Conclusions

It was demonstrated that an x-ray transparent window can be fabricated out of a hematite single crystal without noticeably damaging the material. To achieve this, a Xe PFIB with a F_2 precursor gas was utilized for the milling. With STXM, the spin reorientation from an easy-axis to an easy-plane antiferromagnet at the Morin temperature was imaged. This transition appeared to be non-uniform but influenced by the sample thickness. Furthermore, spin-wave dynamics could be observed at room temperature for both in-plane and out-of-plane magnetic bias fields applied. These dynamics occur at frequencies exceeding 20 GHz, which is faster than the dynamics of typical ferromagnetic systems. While additional measurements and detailed calculations are necessary to get a better understanding of the dynamic processes involved, these results show that the direct imaging of coherently excited propagating spin waves is possible in antiferromagnetic systems.

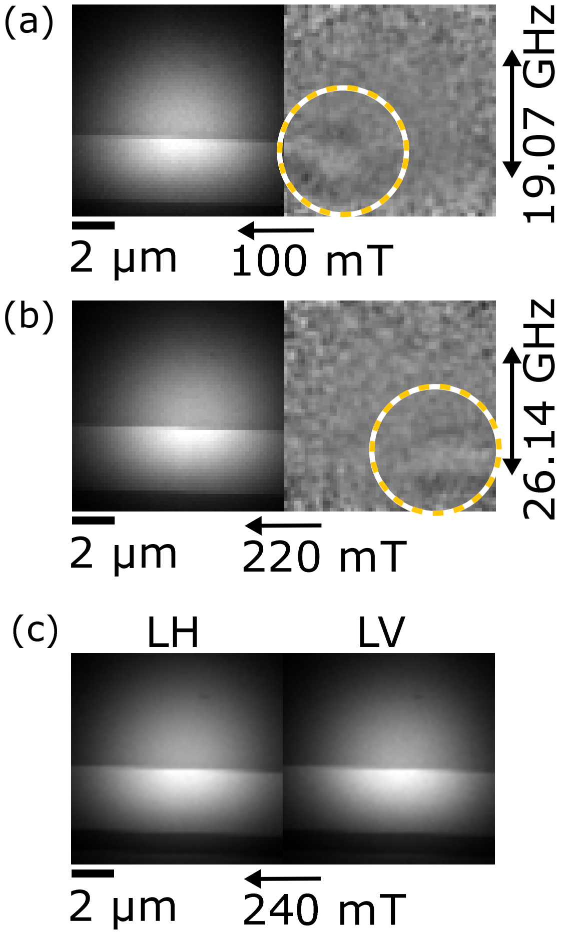

Figure 7.6: (a,b) Spin waves in hematite at room temperature and static external in-plane magnetic fields applied, imaged by TR-STXM with circularly positive polarised x-rays. Absolute absorption images are depicted on the left hand side, time normalized snapshots on the right hand side. Spin-wave dynamics indicated by the yellow dashed circles. a) Alternating field excitation with a frequency of 19.07 GHz and a static in-plane field of 100 mT applied. b) Alternating field excitation of 26.14 GHz with an in-plane field of 220 mT. c) Absolute absoption images taken with linear horizontal (LH) and vertical (LV) x-rays.

8 Conclusions and Outlook

The aim of this thesis was to directly image and understand different characteristics of spin waves in ferromagnetic, ferrimagnetic and antiferromagnetic systems by using x-ray microscopy. Time-resolved scanning transmission x-ray microscopy proved to be an ideal tool to image the fast dynamics at the nanoscale in all of the studied systems.

At first, single ferromagnetic layers as well as synthetic ferrimagnets were characterised. In particular, a way to utilise static magnetic bias field to control and manipulate short-wavelength spin waves emitted from a vortex core. It was found that the magnetic field displaced the spin-wave emitting vortex core from the equilibrium central position of a structure, while maintaining the spin-wave emission and without influencing the dispersion relation. It was further observed that, via field-induced expansion of the vortex core in a single layer system, the core became a source for the directional emission of spin waves and even allowed for focusing effects. These findings were corroborated by micromagnetic simulations [30].

Moreover, in such single and coupled ferromagnetic systems, the direct imaging of spin waves at frequencies exceeding 30 GHz and of wavelengths below 70 nm was demonstrated. In a trilayer system with antiparallel orientation of the two ferromagnetic layers, acoustic and optical modes were observed. In single-layer systems, higher order perpendicular standing spin waves up to the fourth order were imaged and the influence of material properties, film thickness and external magnetic bias fields on the spin-wave dispersion relation were analysed. The experimental findings were compared with and supported by theoretical predictions [115].

In addition, systems with antiferromagnetically coupled sublattices were studied, which could not be grown on x-ray transparent Si_3N_4 membranes. In order to perform STXM measurements on these systems, a technique to fabricate soft x-ray transparent windows into bulk substrates and samples was developed. This technique is based on the use of a Xe Plasma Focused Ion Beam milling process, that can be combined with mechanical grinding if required. The developed process can be used for a variety of materials and, hence, can facilitate a wide range of investigations otherwise not possible [77].

Using this thinning process, spin-wave dynamics in ferrimagnetic YIG systems, which were doped with Ga to lower their magnetization and to reach magnetization compensation, were studied. For moderate doping, resulting in approximately 10 % of the magnetization of undoped YIG, the material exhibited a damping close to the low values characteristic for YIG. At the same time, exchange-dominated spin waves at long wavelengths were observed due to the large exchange length of the material. Furthermore, non-linear effects lead to an unexpectedly high spin-wave precession angle of more than 20°. These findings were reproduced by micromagnetic simulations. Additionally, spin waves in the forward volume geometry as well as domain-wall and domain dynamics were excited and imaged in the system.

Finally, an antiferromagnet was characterised, namely single-crystalline hematite. The spin reorientation transition from an easy-axis to an easy-plane antiferromagnet at the Morin temperature was directly imaged. Furthermore, spin-wave dynamics were coherently excited and observed in the canted antiferromagnetic state at room temperature at frequencies exceeding 20 GHz.

Even though possibilities to tune the frequencies in ferromagnetic systems were shown in this thesis, the most-promising path to increase the frequencies in magnonics is to utilise ferrimagnets and antiferromagnets. This requires a better understanding of the dynamics in such systems and thus further studies of antiferromagnetic as well as low-damping ferrimagnetic systems are needed.

Regarding the Ga:YIG system, detailed calculations and simulations will be needed to understand the non-linear excitation phenomenon leading to the observed giant spin-wave amplitudes. In addition, the strong contrast of the samples allows for short measurement times with STXM exploiting sublattice imaging. This could be used to an advantage in other investigations as well, for example in the phase-resolved observation of Bose-Einstein condensation of magnons. The strong contrast might prove particularly useful for studies that typically suffer from long integration times in STXM such as domain-wall propagation. However, in order to confine the domain walls and guide their propagation, a patterning process for the Ga:YIG films might have to be developed.

Furthermore, for studying magnons in vicinity of the compensation temperature, samples with lower Ga doping, which exhibit compensation points at lower temperatures, may still exhibit sufficiently low damping to enable the observation of propagating spin waves. However, due to the nature of compensated ferrimagnets and antiferromagnets, different excitation mechanisms, e.g. based on spin torques, might be required for efficient spin-wave excitation. This is true in particular for the excitation of spin waves in hematite, where the finite-wavelength dynamics in the low temperature, fully antiferromagnetic phase remains to be observed. Moreover, a direct observation of its high-frequency mode would be interesting in comparison. However, these measurements might require even better time-resolution than currently offered by the low-alpha optics operation modes but could be achieved at x-ray free electron lasers. An improved time resolution will also be necessary for the study of other antiferromagnetic materials, where the resonance frequencies are even higher than in hematite. In particular, in connection with hematite, the study of other canted antiferromagnets such as orthoferrites, could help to gain a better understanding of spin-wave dynamics in such canted antiferromagnetic systems.

In conclusion, this thesis displays the state-of-the-art imaging of spin-wave dynamics in ferromagnetic, ferrimagnetic and antiferromagnetic systems, and the techniques and studies presented offer a highly promising basis for further investigations into spin waves in these systems.

Bibliography

[1] A. V. Chumak, V. I. Vasyuchka, A. A. Serga, and B. Hillebrands. “Magnon spintronics”. *Nature Physics* 11.6 (2015), pp. 453–461. ISSN: 1745-2473 1745-2481. DOI: `10.1038/nphys3347`.

[2] T. Jungwirth, X. Marti, P. Wadley, and J. Wunderlich. “Antiferromagnetic spintronics”. *Nature Nanotechnology* 11 (2016), p. 231. DOI: `10.1038/nnano.2016.18`.

[3] V. Baltz, A. Manchon, M. Tsoi, T. Moriyama, T. Ono, and Y. Tserkovnyak. “Antiferromagnetic spintronics”. *Reviews of Modern Physics* 90.1 (2018), p. 015005. DOI: `10.1103/RevModPhys.90.015005`.

[4] C. Kittel. “Theory of Antiferromagnetic Resonance”. *Physical Review* 82.4 (1951), pp. 565–565. DOI: `10.1103/PhysRev.82.565`.

[5] F. M. Johnson and A. H. Nethercot. “Antiferromagnetic Resonance in $\mathrm{MnF_2}$”. *Physical Review* 114.3 (1959), pp. 705–716. DOI: `10.1103/PhysRev.114.705`.

[6] T. Kampfrath, A. Sell, G. Klatt, A. Pashkin, S. Mährlein, T. Dekorsy, M. Wolf, M. Fiebig, A. Leitenstorfer, and R. Huber. “Coherent terahertz control of antiferromagnetic spin waves”. *Nature Photonics* 5.1 (2011), pp. 31–34. ISSN: 1749-4893. DOI: `10.1038/nphoton.2010.259`.

[7] J. R. Hortensius, D. Afanasiev, M. Matthiesen, R. Leenders, R. Citro, A. V. Kimel, R. V. Mikhaylovskiy, B. A. Ivanov, and A. D. Caviglia. “Coherent spin-wave transport in an antiferromagnet”. *Nature Physics* 17.9 (2021), pp. 1001–1006. ISSN: 1745-2481. DOI: `10.1038/s41567-021-01290-4`.

[8] C. Kim, S. Lee, H.-G. Kim, J.-H. Park, K.-W. Moon, J. Y. Park, J. M. Yuk, K.-J. Lee, B.-G. Park, S. K. Kim, K.-J. Kim, and C. Hwang. “Distinct handedness of spin wave across the compensation temperatures of ferrimagnets”. *Nature Materials* 19.9 (2020), pp. 980–985. ISSN: 1476-4660. DOI: `10.1038/s41563-020-0722-8`.

[9] G. Dieterle, J. Förster, H. Stoll, A. S. Semisalova, S. Finizio, A. Gangwar, M. Weigand, M. Noske, M. Fähnle, I. Bykova, J. Gräfe, D. A. Bozhko, H. Y. Musiienko-Shmarova, V. Tiberkevich, A. N. Slavin, C. H. Back, J. Raabe, G. Schütz, and S. Wintz. "Coherent Excitation of Heterosymmetric Spin Waves with Ultrashort Wavelengths". *Physical Review Letters* 122.11 (2019), p. 117202. DOI: `10.1103/PhysRevLett.122.117202`.

[10] J. Förster, J. Gräfe, J. Bailey, S. Finizio, N. Träger, F. Groß, S. Mayr, H. Stoll, C. Dubs, O. Surzhenko, N. Liebing, G. Woltersdorf, J. Raabe, M. Weigand, G. Schütz, and S. Wintz. "Direct observation of coherent magnons with suboptical wavelengths in a single-crystalline ferrimagnetic insulator". *Physical Review B* 100.21 (2019), p. 214416. DOI: `10.1103/PhysRevB.100.214416`.

[11] F. Nolting, A. Scholl, J. Stöhr, J. W. Seo, J. Fompeyrine, H. Siegwart, J. P. Locquet, S. Anders, J. Lüning, E. E. Fullerton, M. F. Toney, M. R. Scheinfein, and H. A. Padmore. "Direct observation of the alignment of ferromagnetic spins by antiferromagnetic spins". *Nature* 405.6788 (2000), pp. 767–769. ISSN: 1476-4687. DOI: `10.1038/35015515`.

[12] H. Jani, J.-C. Lin, J. Chen, J. Harrison, F. Maccherozzi, J. Schad, S. Prakash, C.-B. Eom, A. Ariando, T. Venkatesan, and P. G. Radaelli. "Antiferromagnetic half-skyrmions and bimerons at room temperature". *Nature* 590.7844 (2021), pp. 74–79. ISSN: 1476-4687. DOI: `10.1038/s41586-021-03219-6`.

[13] A. V. Chumak et al. *Roadmap on Spin-Wave Computing.* Electronic Article. 2021.

[14] R. Gross and A. Marx. *Festkörperphysik.* De Gruyter Oldenbourg, 2014. DOI: `10.1524/9783110358704`.

[15] S. Blundell. *Magnetism in Condensed Matter.* Oxford Master Series in Condensed Matter Physics. New York: Oxford University Press, 2001. ISBN: 9780198505914.

[16] S. M. Rezende. *Fundamentals of Magnonics.* Lecture Notes in Physics. Springer, 2020. DOI: `10.1007/978-3-030-41317-0`.

[17] A. J. Princep, R. A. Ewings, S. Ward, S. Tóth, C. Dubs, D. Prabhakaran, and A. T. Boothroyd. "The full magnon spectrum of yttrium iron garnet". *npj Quantum Materials* 2.1 (2017), p. 63. ISSN: 2397-4648. DOI: `10.1038/s41535-017-0067-y`.

[18] I. Dzyaloshinsky. "A thermodynamic theory of "weak" ferromagnetism of antiferromagnetics". *Journal of Physics and Chemistry of Solids* 4.4 (1958), pp. 241–255. ISSN: 0022-3697. DOI: `https://doi.org/10.1016/0022-3697(58)90076-3`.

[19] T. Moriya. “Anisotropic Superexchange Interaction and Weak Ferromagnetism”. *Physical Review* 120.1 (1960), pp. 91–98. DOI: `10.1103/PhysRev.120.91`.

[20] A. Hubert and R. Schäfer. *Magnetic Domains - The Analysis of Magnetic Microstructures.* Vol. 1. Berlin Heidelberg: Springer, 1998. DOI: `10.1007/978-3-540-85054-0`.

[21] J. Raabe, R. Pulwey, R. Sattler, T. Schweinböck, J. Zweck, and D. Weiss. “Magnetization pattern of ferromagnetic nanodisks”. *Journal of Applied Physics* 88.7 (2000), pp. 4437–4439. DOI: `10.1063/1.1289216`.

[22] T. Shinjo, T. Okuno, R. Hassdorf, †. K. Shigeto, and T. Ono. “Magnetic Vortex Core Observation in Circular Dots of Permalloy”. *Science* 289.5481 (2000), pp. 930–932. DOI: `10.1126/science.289.5481.930`.

[23] O. A. Tretiakov and O. Tchernyshyov. “Vortices in thin ferromagnetic films and the skyrmion number”. *Physical Review B* 75.1 (2007), p. 012408. DOI: `10.1103/PhysRevB.75.012408`.

[24] L. D. Landau and E. Lifshitz. “On the theory of the dispersion of magnetic permeability in ferromagnetic bodies”. *Phys. Z. Sowjet.* 8 (1935), p. 153.

[25] J. C. Slonczewski. “Current-driven excitation of magnetic multilayers”. *Journal of Magnetism and Magnetic Materials* 159.1 (1996), pp. L1–L7. ISSN: 0304-8853. DOI: `https://doi.org/10.1016/0304-8853(96)00062-5`.

[26] S. Zhang and Z. Li. “Roles of Nonequilibrium Conduction Electrons on the Magnetization Dynamics of Ferromagnets”. *Physical Review Letters* 93.12 (2004), p. 127204. DOI: `10.1103/PhysRevLett.93.127204`.

[27] A. Thiaville, Y. Nakatani, J. Miltat, and Y. Suzuki. “Micromagnetic understanding of current-driven domain wall motion in patterned nanowires”. *Europhysics Letters (EPL)* 69.6 (2005), pp. 990–996. ISSN: 0295-5075 1286-4854. DOI: `10.1209/epl/i2004-10452-6`.

[28] A. Vansteenkiste, J. Leliaert, M. Dvornik, M. Helsen, F. Garcia-Sanchez, and B. van Waeyenberge. “The design and verification of MuMax3”. *AIP Advances* 4.10 (2014), p. 107133. DOI: `10.1063/1.4899186`.

[29] H. Kronmüller. “Mikromagnetische Berechnung der Magnetisierung in der Umgebung unmagnetischer Einschlüsse in Ferromagnetika”. *Zeitschrift für Physik* 168.5 (1962), pp. 478–494. ISSN: 0044-3328. DOI: `10.1007/BF01378144`.

[30] S. Mayr, L. Flajšman, S. Finizio, A. Hrabec, M. Weigand, J. Förster, H. Stoll, L. J. Heyderman, M. Urbánek, S. Wintz, and J. Raabe. "Spin-Wave Emission from Vortex Cores under Static Magnetic Bias Fields". *Nano Letters* 21.4 (2021), pp. 1584–1590. ISSN: 1530-6984. DOI: `10.1021/acs.nanolett.0c03740`.

[31] R. W. Damon and J. R. Eshbach. "Magnetostatic modes of a ferromagnet slab". *Journal of Physics and Chemistry of Solids* 19.3 (1961), pp. 308–320. ISSN: 0022-3697. DOI: `10.1016/0022-3697(61)90041-5`.

[32] B. A. Kalinikos and A. N. Slavin. "Theory of dipole-exchange spin wave spectrum for ferromagnetic films with mixed exchange boundary conditions". *Journal of Physics C: Solid State Physics* 19.35 (1986), pp. 7013–7033. ISSN: 0022-3719. DOI: `10.1088/0022-3719/19/35/014`.

[33] J. Förster, S. Wintz, J. Bailey, S. Finizio, E. Josten, C. Dubs, D. A. Bozhko, H. Stoll, G. Dieterle, N. Träger, J. Raabe, A. N. Slavin, M. Weigand, J. Gräfe, and G. Schütz. "Nanoscale X-ray imaging of spin dynamics in yttrium iron garnet". *Journal of Applied Physics* 126.17 (2019), p. 173909. ISSN: 0021-8979. DOI: `10.1063/1.5121013`.

[34] B. A. Kalinikos, M. P. Kostylev, N. V. Kozhus, and A. N. Slavin. "The dipole-exchange spin wave spectrum for anisotropic ferromagnetic films with mixed exchange boundary conditions". *Journal of Physics: Condensed Matter* 2.49 (1990), pp. 9861–9877. ISSN: 0953-8984 1361-648X. DOI: `10.1088/0953-8984/2/49/012`.

[35] O. Gomonay, V. Baltz, A. Brataas, and Y. Tserkovnyak. "Antiferromagnetic spin textures and dynamics". *Nature Physics* 14.3 (2018), pp. 213–216. ISSN: 1745-2481. DOI: `10.1038/s41567-018-0049-4`.

[36] S. M. Rezende, A. Azevedo, and R. L. Rodríguez-Suárez. "Introduction to antiferromagnetic magnons". *Journal of Applied Physics* 126.15 (2019), p. 151101. ISSN: 0021-8979. DOI: `10.1063/1.5109132`.

[37] H. B. Nielsen and S. Chadha. "On how to count Goldstone bosons". *Nuclear Physics B* 105.3 (1976), pp. 445–453. ISSN: 0550-3213. DOI: `https://doi.org/10.1016/0550-3213(76)90025-0`.

[38] H. Watanabe and H. Murayama. "Unified Description of Nambu-Goldstone Bosons without Lorentz Invariance". *Physical Review Letters* 108.25 (2012), p. 251602. DOI: `10.1103/PhysRevLett.108.251602`.

[39] A. G. Gurevich and G. A. Melkov. *Magnetization Oscillations and Waves.* Vol. 1. Boca Raton: CRC Press, 1996. ISBN: 9780849394607.

[40] B. Divinskiy, V. E. Demidov, S. Urazhdin, R. Freeman, A. B. Rinkevich, and S. O. Demokritov. “Excitation and Amplification of Spin Waves by Spin–Orbit Torque”. *Advanced Materials* 30.33 (2018), p. 1802837. ISSN: 0935-9648. DOI: `https://doi.org/10.1002/adma.201802837`.

[41] H. Fulara, M. Zahedinejad, R. Khymyn, A. A. Awad, S. Muralidhar, M. Dvornik, and J. Åkerman. “Spin-orbit torque–driven propagating spin waves”. *Science Advances* 5.9 (2019), eaax8467. DOI: `10.1126/sciadv.aax8467`.

[42] V. E. Demidov, S. Urazhdin, A. Anane, V. Cros, and S. O. Demokritov. “Spin–orbit-torque magnonics”. *Journal of Applied Physics* 127.17 (2020), p. 170901. DOI: `10.1063/5.0007095`.

[43] M. Madami, S. Bonetti, G. Consolo, S. Tacchi, G. Carlotti, G. Gubbiotti, F. B. Mancoff, M. A. Yar, and J. Åkerman. “Direct observation of a propagating spin wave induced by spin-transfer torque”. *Nature Nanotechnology* 6 (2011), p. 635. DOI: `10.1038/nnano.2011.140`.

[44] S. Urazhdin, V. E. Demidov, H. Ulrichs, T. Kendziorczyk, T. Kuhn, J. Leuthold, G. Wilde, and S. O. Demokritov. “Nanomagnonic devices based on the spin-transfer torque”. *Nature Nanotechnology* 9.7 (2014), pp. 509–513. ISSN: 1748-3395. DOI: `10.1038/nnano.2014.88`.

[45] H. Yu, O. d’Allivy Kelly, V. Cros, R. Bernard, P. Bortolotti, A. Anane, F. Brandl, F. Heimbach, and D. Grundler. “Approaching soft X-ray wavelengths in nanomagnet-based microwave technology”. *Nature Communications* 7.1 (2016), p. 11255. ISSN: 2041-1723. DOI: `10.1038/ncomms11255`.

[46] C. Liu, J. Chen, T. Liu, F. Heimbach, H. Yu, Y. Xiao, J. Hu, M. Liu, H. Chang, T. Stueckler, S. Tu, Y. Zhang, Y. Zhang, P. Gao, Z. Liao, D. Yu, K. Xia, N. Lei, W. Zhao, and M. Wu. “Long-distance propagation of short-wavelength spin waves”. *Nature Communications* 9.1 (2018), p. 738. ISSN: 2041-1723. DOI: `10.1038/s41467-018-03199-8`.

[47] E. Schlömann. “Generation of Spin Waves in Nonuniform Magnetic Fields. I. Conversion of Electromagnetic Power into Spin-Wave Power and Vice Versa”. *Journal of Applied Physics* 35.1 (1964), pp. 159–166. DOI: `10.1063/1.1713058`.

[48] C. S. Davies and V. V. Kruglyak. “Graded-index magnonics”. *Low Temperature Physics* 41.10 (2015), pp. 760–766. DOI: `10.1063/1.4932349`.

[49] S. Wintz, V. Tiberkevich, M. Weigand, J. Raabe, J. Lindner, A. Erbe, A. Slavin, and J. Fassbender. “Magnetic vortex cores as tunable spin-wave emitters”. *Nature Nanotechnology* 11.11 (2016), pp. 948–953. DOI: `10.1038/nnano.2016.117`.

[50] C. S. Davies, V. D. Poimanov, and V. V. Kruglyak. “Mapping the magnonic landscape in patterned magnetic structures”. *Physical Review B* 96.9 (2017), p. 094430. DOI: `10.1103/PhysRevB.96.094430`.

[51] C. Behncke, C. F. Adolff, N. Lenzing, M. Hänze, B. Schulte, M. Weigand, G. Schütz, and G. Meier. “Spin-wave interference in magnetic vortex stacks”. *Communications Physics* 1.1 (2018), p. 50. ISSN: 2399-3650. DOI: `10.1038/s42005-018-0052-1`.

[52] D. Osuna Ruiz, E. B. Parra, N. Bukin, M. Heath, A. Lara, F. G. Aliev, A. P. Hibbins, and F. Y. Ogrin. “Dynamics of spiral spin waves in magnetic nanopatches: Influence of thickness and shape”. *Physical Review B* 100.21 (2019), p. 214437. DOI: `10.1103/PhysRevB.100.214437`.

[53] L.-J. Chang, J. Chen, D. Qu, L.-Z. Tsai, Y.-F. Liu, M.-Y. Kao, J.-Z. Liang, T.-S. Wu, T.-M. Chuang, H. Yu, and S.-F. Lee. “Spin Wave Injection and Propagation in a Magnetic Nanochannel from a Vortex Core”. *Nano Letters* 20.5 (2020), pp. 3140–3146. ISSN: 1530-6984. DOI: `10.1021/acs.nanolett.9b05133`.

[54] V. Sluka, T. Schneider, R. A. Gallardo, A. Kákay, M. Weigand, T. Warnatz, R. Mattheis, A. Roldán-Molina, P. Landeros, V. Tiberkevich, A. Slavin, G. Schütz, A. Erbe, A. Deac, J. Lindner, J. Raabe, J. Fassbender, and S. Wintz. “Emission and propagation of 1D and 2D spin waves with nanoscale wavelengths in anisotropic spin textures”. *Nature Nanotechnology* 14.4 (2019), pp. 328–333. ISSN: 1748-3395. DOI: `10.1038/s41565-019-0383-4`.

[55] E. Albisetti, D. Petti, G. Sala, R. Silvani, S. Tacchi, S. Finizio, S. Wintz, A. Calò, X. Zheng, J. Raabe, E. Riedo, and R. Bertacco. “Nanoscale spin-wave circuits based on engineered reconfigurable spin-textures”. *Communications Physics* 1.1 (2018), p. 56. ISSN: 2399-3650. DOI: `10.1038/s42005-018-0056-x`.

[56] T. Brächer, M. Fabre, T. Meyer, T. Fischer, S. Auffret, O. Boulle, U. Ebels, P. Pirro, and G. Gaudin. “Detection of Short-Waved Spin Waves in Individual Microscopic Spin-Wave Waveguides Using the Inverse Spin Hall Effect”. *Nano Letters* 17.12 (2017), pp. 7234–7241. ISSN: 1530-6984. DOI: `10.1021/acs.nanolett.7b02458`.

[57] F. Ciubotaru, T. Devolder, M. Manfrini, C. Adelmann, and I. P. Radu. “All electrical propagating spin wave spectroscopy with broadband wavevector capability”. *Applied Physics Letters* 109.1 (2016), p. 012403. DOI: `10.1063/1.4955030`.

[58] J. Hamrle, J. Pištora, B. Hillebrands, B. Lenk, and M. Münzenberg. “Analytical expression of the magneto-optical Kerr effect and Brillouin light scattering intensity arising from dynamic magnetization”. *Journal of Physics*

D: Applied Physics 43.32 (2010), p. 325004. ISSN: 0022-3727 1361-6463. DOI: `10.1088/0022-3727/43/32/325004`.

[59] B. Hillebrands. *Spindynamik in magnetischen Schichten und Vielfachschichten.* Electronic Article. 1999.

[60] E. A. Giess, J. D. Kuptsis, and E. A. D. White. "Liquid phase epitaxial growth of magnetic garnet films by isothermal dipping in a horizontal plane with axial rotation". *Journal of Crystal Growth* 16.1 (1972), pp. 36–42. ISSN: 0022-0248. DOI: `https://doi.org/10.1016/0022-0248(72)90083-8`.

[61] C. Dubs, O. Surzhenko, R. Linke, A. Danilewsky, U. Brückner, and J. Dellith. "Sub-micrometer yttrium iron garnet LPE films with low ferromagnetic resonance losses". *Journal of Physics D: Applied Physics* 50.20 (2017). DOI: `https://doi.org/10.1088/1361-6463/aa6b1c`.

[62] P. Willmott. *Introduction to Synchrotron Radiation: Techniques and Applications.* Vol. 2. Chichester: John Wiley & Sons, 2019. ISBN: 9781119280392.

[63] D. Cocco and M. Zangrando. "Synchrotron Radiation Sources and Optical Devices". In: *Magnetism and Synchrotron Radiation.* Ed. by E. Beaurepaire, H. Bulou, F. Scheurer, and J.-P. Kappler. 1st ed. Berlin Heidelberg: Springer, 2010. DOI: `10.1007/978-3-642-04498-4`.

[64] G. Schütz, W. Wagner, W. Wilhelm, P. Kienle, R. Zeller, R. Frahm, and G. Materlik. "Absorption of circularly polarized x rays in iron". *Phys Rev Lett* 58.7 (1987), pp. 737–740. ISSN: 1079-7114 (Electronic) 0031-9007 (Linking). DOI: `10.1103/PhysRevLett.58.737`.

[65] J. Als-Nielsen and D. McMorrow. *Elements of Modern X-ray Physics.* Vol. 2. New York: Wiley, 2011, pp. 305–342. DOI: `10.1002/9781119998365`.

[66] H. Wende and C. Antoniak. "X-Ray Magnetic Dichroism". In: *Magnetism and Synchrotron Radiation.* Ed. by E. Beaurepaire, H. Bulou, F. Scheurer, and J.-P. Kappler. 1st ed. Berlin Heidelberg: Springer, 2010. DOI: `10.1007/978-3-642-04498-4`.

[67] M. Buess, J. Raabe, C. Quitmann, J. Stahl, and C. H. Back. "Imaging excitations in magnetic thin film microstructures". *Surface Science* 601.22 (2007), pp. 5246–5253. ISSN: 0039-6028. DOI: `10.1016/j.susc.2007.04.217`.

[68] B. T. Thole, P. Carra, F. Sette, and G. van der Laan. "X-ray circular dichroism as a probe of orbital magnetization". *Physical Review Letters* 68.12 (1992), pp. 1943–1946. DOI: `10.1103/PhysRevLett.68.1943`.

[69] P. Carra, B. T. Thole, M. Altarelli, and X. Wang. “X-ray circular dichroism and local magnetic fields”. *Physical Review Letters* 70.5 (1993), pp. 694–697. DOI: `10.1103/PhysRevLett.70.694`.

[70] C. T. Chen, Y. U. Idzerda, H. J. Lin, N. V. Smith, G. Meigs, E. Chaban, G. H. Ho, E. Pellegrin, and F. Sette. “Experimental Confirmation of the X-Ray Magnetic Circular Dichroism Sum Rules for Iron and Cobalt”. *Physical Review Letters* 75.1 (1995), pp. 152–155. DOI: `10.1103/PhysRevLett.75.152`.

[71] G. van der Laan, B. T. Thole, G. A. Sawatzky, J. B. Goedkoop, J. C. Fuggle, J.-M. Esteva, R. Karnatak, J. P. Remeika, and H. A. Dabkowska. “Experimental proof of magnetic x-ray dichroism”. *Physical Review B* 34.9 (1986), pp. 6529–6531. DOI: `10.1103/PhysRevB.34.6529`.

[72] C. M. Schneider. “Element-Specific Probes of Magnetism”. In: *Handbook of Surface Science*. Ed. by R. E. Camley, Z. Celinski, and R. L. Stamps. Vol. 5. North-Holland, 2015. Chap. 2, pp. 43–112. ISBN: 1573-4331. DOI: `10.1016/B978-0-444-62634-9.00002-3`.

[73] J. Raabe, G. Tzvetkov, U. Flechsig, M. Boge, A. Jaggi, B. Sarafimov, M. G. Vernooij, T. Huthwelker, H. Ade, D. Kilcoyne, T. Tyliszczak, R. H. Fink, and C. Quitmann. “PolLux: a new facility for soft x-ray spectromicroscopy at the Swiss Light Source”. *Rev Sci Instrum* 79.11 (2008), p. 113704. ISSN: 1089-7623 (Electronic) 0034-6748 (Linking). DOI: `10.1063/1.3021472`.

[74] D. Nolle, M. Weigand, P. Audehm, E. Goering, U. Wiesemann, C. Wolter, E. Nolle, and G. Schütz. “Note: Unique characterization possibilities in the ultra high vacuum scanning transmission x-ray microscope (UHV-STXM) “MAXYMUS” using a rotatable permanent magnetic field up to 0.22 T”. *Review of Scientific Instruments* 83.4 (2012), p. 046112. ISSN: 0034-6748. DOI: `10.1063/1.4707747`.

[75] A. Puzic, T. Korhonen, B. Kalantari, J. Raabe, C. Quitmann, P. Jüllig, L. Bommer, D. Goll, G. Schütz, S. Wintz, T. Strache, M. Körner, D. Markó, C. Bunce, and J. Fassbender. “Photon Counting System for Time-resolved Experiments in Multibunch Mode”. *Synchrotron Radiation News* 23.2 (2010), pp. 26–32. ISSN: 0894-0886 1931-7344. DOI: `10.1080/08940881003702056`.

[76] S. Finizio, S. Mayr, and J. Raabe. “Time-of-arrival detection for time-resolved scanning transmission X-ray microscopy imaging”. *Journal of Synchrotron Radiation* 27.5 (2020). ISSN: 1600-5775. DOI: `10.1107/S1600577520007262`.

[77] S. Mayr, S. Finizio, J. Reuteler, S. Stutz, C. Dubs, M. Weigand, A. Hrabec, J. Raabe, and S. Wintz. “Xenon Plasma Focused Ion Beam Milling for Obtaining Soft X-ray Transparent Samples”. *Crystals* 11.5 (2021), p. 546. ISSN: 2073-4352. DOI: `10.3390/cryst11050546`.

[78] H. Seidel, L. Csepregi, A. Heuberger, and H. Baumgärtel. “Anisotropic Etching of Crystalline Silicon in Alkaline Solutions: I . Orientation Dependence and Behavior of Passivation Layers”. *Journal of The Electrochemical Society* 137.11 (1990), pp. 3612–3626. ISSN: 0013-4651 1945-7111. DOI: `10.1149/1.2086277`.

[79] W. P. Gomes. “Wet etching of III–V semiconductors”. In: *Handbook of Advanced Electronic and Photonic Materials and Devices*. Ed. by H. S. Nalwa. San Diego, CA: Academic Press, 2001. Chap. 6, pp. 221–256. ISBN: 978-0-12-513745-4. DOI: `https://doi.org/10.1016/B978-012513745-4/50018-4`.

[80] E. Digernes, J. Leliaert, M. Weigand, E. Folven, and B. Van Waeyenberge. “Direct observation of temperature dependent vortex dynamics in a La0.7Sr0.3MnO3 micromagnet”. *Physical Review Research* 2.4 (2020), p. 043429. DOI: `10.1103/PhysRevResearch.2.043429`.

[81] M. Fohler, S. Frömmel, M. Schneider, B. Pfau, C. M. Günther, M. Hennecke, E. Guehrs, L. Shemilt, D. Mishra, D. Berger, S. Selve, D. Mitin, M. Albrecht, and S. Eisebitt. “A general approach to obtain soft x-ray transparency for thin films grown on bulk substrates”. *Review of Scientific Instruments* 88.10 (2017), p. 103701. DOI: `10.1063/1.5006522`.

[82] J. Simmendinger, S. Ruoss, C. Stahl, M. Weigand, J. Gräfe, G. Schütz, and J. Albrecht. “Transmission x-ray microscopy at low temperatures: Irregular supercurrent flow at small length scales”. *Physical Review B* 97.13 (2018), p. 134515. DOI: `10.1103/PhysRevB.97.134515`.

[83] K. Baumgaertl, J. Gräfe, P. Che, A. Mucchietto, J. Förster, N. Träger, M. Bechtel, M. Weigand, G. Schütz, and D. Grundler. “Nanoimaging of Ultrashort Magnon Emission by Ferromagnetic Grating Couplers at GHz Frequencies”. *Nano Letters* (2020). ISSN: 1530-6984. DOI: `10.1021/acs.nanolett.0c02645`.

[84] F. Büttner, M. A. Mawass, J. Bauer, E. Rosenberg, L. Caretta, C. O. Avci, J. Gräfe, S. Finizio, C. A. F. Vaz, N. Novakovic, M. Weigand, K. Litzius, J. Förster, N. Träger, F. Groß, D. Suzuki, M. Huang, J. Bartell, F. Kronast, J. Raabe, G. Schütz, C. A. Ross, and G. S. D. Beach. “Thermal nucleation and high-resolution imaging of submicrometer magnetic bubbles in thin thulium iron garnet films with perpendicular anisotropy”. *Physical Review Materials* 4.1 (2020), p. 011401. DOI: `10.1103/PhysRevMaterials.4.011401`.

[85] N. Träger, F. Groß, J. Förster, K. Baumgaertl, H. Stoll, M. Weigand, G. Schütz, D. Grundler, and J. Gräfe. "Single shot acquisition of spatially resolved spin wave dispersion relations using X-ray microscopy". *Scientific Reports* 10.1 (2020), p. 18146. ISSN: 2045-2322. DOI: `10.1038/s41598-020-74785-4`.

[86] T. L. Burnett, R. Kelley, B. Winiarski, L. Contreras, M. Daly, A. Gholinia, M. G. Burke, and P. J. Withers. "Large volume serial section tomography by Xe Plasma FIB dual beam microscopy". *Ultramicroscopy* 161 (2016), pp. 119–129. ISSN: 0304-3991. DOI: `https://doi.org/10.1016/j.ultramic.2015.11.001`.

[87] P. Bouguer. *Essai d'optique, Sur la gradation de la lumière*. Paris: Claude Jombert, 1729.

[88] J. H. Lambert. *Photometria, sive de mensura et gradibus luminis, colorum et umbrae*. Augsburg: Eberhard Klett, 1760.

[89] A. Beer. "Bestimmung der Absorption des rothen Lichts in farbigen Flüssigkeiten". *Annalen der Physik* 162.5 (1852), pp. 78–88. ISSN: 0003-3804. DOI: `https://doi.org/10.1002/andp.18521620505`.

[90] E. Gullikson. *X-Ray Interactions With Matter*. Online Database.

[91] J. F. Ziegler, M. D. Ziegler, and J. P. Biersack. "SRIM – The stopping and range of ions in matter (2010)". *Nuclear Instruments and Methods in Physics Research Section B: Beam Interactions with Materials and Atoms* 268.11 (2010), pp. 1818–1823. ISSN: 0168-583X. DOI: `https://doi.org/10.1016/j.nimb.2010.02.091`.

[92] S. J. Hermsdoerfer, H. Schultheiss, C. Rausch, S. Schäfer, B. Leven, S.-K. Kim, and B. Hillebrands. "A spin-wave frequency doubler by domain wall oscillation". *Applied Physics Letters* 94.22 (2009), p. 223510. DOI: `10.1063/1.3143225`.

[93] E. Albisetti, S. Tacchi, R. Silvani, G. Scaramuzzi, S. Finizio, S. Wintz, C. Rinaldi, M. Cantoni, J. Raabe, G. Carlotti, R. Bertacco, E. Riedo, and D. Petti. "Optically Inspired Nanomagnonics with Nonreciprocal Spin Waves in Synthetic Antiferromagnets". *Advanced Materials* 32.9 (2020), p. 1906439. ISSN: 0935-9648. DOI: `10.1002/adma.201906439`.

[94] P. Grünberg, R. Schreiber, Y. Pang, M. B. Brodsky, and H. Sowers. "Layered Magnetic Structures: Evidence for Antiferromagnetic Coupling of Fe Layers across Cr Interlayers". *Physical Review Letters* 57.19 (1986), pp. 2442–2445. DOI: `10.1103/PhysRevLett.57.2442`.

[95] K. Y. Guslienko, V. Novosad, Y. Otani, H. Shima, and K. Fukamichi. "Magnetization reversal due to vortex nucleation, displacement, and annihilation in submicron ferromagnetic dot arrays". *Physical Review B* 65.2 (2001), p. 024414. DOI: `10.1103/PhysRevB.65.024414`.

[96] S. Wintz, C. Bunce, A. Banholzer, M. Körner, T. Strache, R. Mattheis, J. McCord, J. Raabe, C. Quitmann, A. Erbe, and J. Fassbender. "Interlayer-coupled spin vortex pairs and their response to external magnetic fields". *Physical Review B* 85.22 (2012), p. 224420. DOI: `10.1103/PhysRevB.85.224420`.

[97] M.-Y. Im, H.-S. Han, M.-S. Jung, Y.-S. Yu, S. Lee, S. Yoon, W. Chao, P. Fischer, J.-I. Hong, and K.-S. Lee. "Dynamics of the Bloch point in an asymmetric permalloy disk". *Nature Communications* 10.1 (2019), p. 593. ISSN: 2041-1723. DOI: `10.1038/s41467-019-08327-6`.

[98] F. G. Aliev, J. F. Sierra, A. A. Awad, G. N. Kakazei, D.-S. Han, S.-K. Kim, V. Metlushko, B. Ilic, and K. Y. Guslienko. "Spin waves in circular soft magnetic dots at the crossover between vortex and single domain state". *Physical Review B* 79.17 (2009), p. 174433. DOI: `10.1103/PhysRevB.79.174433`.

[99] M. Vaňatka, M. Urbánek, R. Jíra, L. Flajšman, M. Dhankhar, M.-Y. Im, J. Michalička, V. Uhlíř, and T. Šikola. "Magnetic vortex nucleation modes in static magnetic fields". *AIP Advances* 7.10 (2017), p. 105103. DOI: `10.1063/1.5006235`.

[100] K. Kuepper, L. Bischoff, C. Akhmadaliev, J. Fassbender, H. Stoll, K. W. Chou, A. Puzic, K. Fauth, D. Dolgos, G. Schütz, B. Van Waeyenberge, T. Tyliszczak, I. Neudecker, G. Woltersdorf, and C. H. Back. "Vortex dynamics in Permalloy disks with artificial defects: Suppression of the gyrotropic mode". *Applied Physics Letters* 90.6 (2007), p. 062506. ISSN: 0003-6951. DOI: `10.1063/1.2437710`.

[101] J. Graf, H. Pfeifer, F. Marquardt, and S. Viola Kusminskiy. "Cavity optomagnonics with magnetic textures: Coupling a magnetic vortex to light". *Physical Review B* 98.24 (2018), p. 241406. DOI: `10.1103/PhysRevB.98.241406`.

[102] P. Bryant and H. Suhl. "Magnetization and domain structure of cylinders and spheres in subsaturating fields". *Applied Physics Letters* 54.1 (1989), pp. 78–80. DOI: `10.1063/1.100838`.

[103] J. F. Pulecio, S. D. Pollard, P. Warnicke, D. A. Arena, and Y. Zhu. "Symmetry breaking of magnetic vortices before annihilation". *Applied Physics Letters* 105.13 (2014), p. 132403. DOI: `10.1063/1.4893422`.

[104] P.-O. Jubert, J.-C. Toussaint, O. Fruchart, C. Meyer, and Y. Samson. "Flux-closure-domain states and demagnetizing energy determination in sub-micron size magnetic dots". *Europhys. Lett.* 63.1 (2003), pp. 132–138.

[105] A. Masseboeuf, O. Fruchart, J. C. Toussaint, E. Kritsikis, L. Buda-Prejbeanu, F. Cheynis, P. Bayle-Guillemaud, and A. Marty. "Dimensionality Crossover in Magnetism: From Domain Walls (2D) to Vortices (1D)". *Physical Review Letters* 104.12 (2010). PRL, p. 127204. DOI: `10.1103/PhysRevLett.104.127204`.

[106] R. Hertel and H. Kronmüller. "Computation of the magnetic domain structure in bulk permalloy". *Physical Review B* 60.10 (1999), pp. 7366–7378. DOI: `10.1103/PhysRevB.60.7366`.

[107] V. E. Demidov, S. O. Demokritov, K. Rott, P. Krzysteczko, and G. Reiss. "Self-focusing of spin waves in Permalloy microstripes". *Applied Physics Letters* 91.25 (2007), p. 252504. ISSN: 0003-6951 1077-3118. DOI: `10.1063/1.2825421`.

[108] T. Schneider, A. A. Serga, A. V. Chumak, C. W. Sandweg, S. Trudel, S. Wolff, M. P. Kostylev, V. S. Tiberkevich, A. N. Slavin, and B. Hillebrands. "Non-diffractive subwavelength wave beams in a medium with externally controlled anisotropy". *Phys Rev Lett* 104.19 (2010), p. 197203. ISSN: 1079-7114 (Electronic) 0031-9007 (Linking). DOI: `10.1103/PhysRevLett.104.197203`.

[109] J. V. Kim, R. L. Stamps, and R. E. Camley. "Spin Wave Power Flow and Caustics in Ultrathin Ferromagnets with the Dzyaloshinskii-Moriya Interaction". *Phys Rev Lett* 117.19 (2016), p. 197204. ISSN: 1079-7114 (Electronic) 0031-9007 (Linking). DOI: `10.1103/PhysRevLett.117.197204`.

[110] V. Veerakumar and R. E. Camley. "Magnon focusing in thin ferromagnetic films". *Physical Review B* 74.21 (2006), p. 214401. DOI: `10.1103/PhysRevB.74.214401`.

[111] N. J. Whitehead, S. A. R. Horsley, T. G. Philbin, and V. V. Kruglyak. "A Luneburg lens for spin waves". *Applied Physics Letters* 113.21 (2018), p. 212404. DOI: `10.1063/1.5049470`.

[112] O. Dzyapko, I. V. Borisenko, V. E. Demidov, W. Pernice, and S. O. Demokritov. "Reconfigurable heat-induced spin wave lenses". *Applied Physics Letters* 109.23 (2016), p. 232407. DOI: `10.1063/1.4971829`.

[113] J.-N. Toedt, M. Mundkowski, D. Heitmann, S. Mendach, and W. Hansen. "Design and construction of a spin-wave lens". *Scientific Reports* 6.1 (2016), p. 33169. ISSN: 2045-2322. DOI: `10.1038/srep33169`.

[114] J. Gräfe, P. Gruszecki, M. Zelent, M. Decker, K. Keskinbora, M. Noske, P. Gawronski, H. Stoll, M. Weigand, M. Krawczyk, C. H. Back, E. J. Goering, and G. Schütz. "Direct observation of spin-wave focusing by a Fresnel lens". *Physical Review B* 102.2 (2020), p. 024420. DOI: `10.1103/PhysRevB.102.024420`.

[115] S. Mayr, J. Förster, S. Finizio, R. A. Gallardo, R. Narkovic, G. Dieterle, K. Schultheiss, A. Semisalova, J. Bailey, E. Kirk, J. Lindner, J. Gräfe, J. Raabe, G. Schütz, M. Weigand, H. Stoll, and S. Wintz. "Time-resolved x-ray imaging of spin dynamics at tens of GHz using low-alpha synchrotron operation". *unpublished* (2021).

[116] P. Grünberg, M. G. Cottam, W. Vach, C. Mayr, and R. E. Camley. "Brillouin scattering of light by spin waves in thin ferromagnetic films (invited)". *Journal of Applied Physics* 53.3 (1982), pp. 2078–2083. DOI: `10.1063/1.330751`.

[117] P. Kabos, W. D. Wilber, C. E. Patton, and P. Grünberg. "Brillouin light scattering study of magnon branch crossover in thin iron films". *Physical Review B* 29.11 (1984), pp. 6396–6398. DOI: `10.1103/PhysRevB.29.6396`.

[118] J. Jorzick, S. O. Demokritov, C. Mathieu, B. Hillebrands, B. Bartenlian, C. Chappert, F. Rousseaux, and A. N. Slavin. "Brillouin light scattering from quantized spin waves in micron-size magnetic wires". *Physical Review B* 60.22 (1999), pp. 15194–15200. DOI: `10.1103/PhysRevB.60.15194`.

[119] A. A. Serga, A. V. Chumak, A. André, G. A. Melkov, A. N. Slavin, S. O. Demokritov, and B. Hillebrands. "Parametrically Stimulated Recovery of a Microwave Signal Stored in Standing Spin-Wave Modes of a Magnetic Film". *Physical Review Letters* 99.22 (2007), p. 227202. DOI: `10.1103/PhysRevLett.99.227202`.

[120] S. Schäfer, A. V. Chumak, A. A. Serga, G. A. Melkov, and B. Hillebrands. "Microwave spectral analysis by means of nonresonant parametric recovery of spin-wave signals in a thin magnetic film". *Applied Physics Letters* 92.16 (2008), p. 162514. DOI: `10.1063/1.2917590`.

[121] O. Gaier, J. Hamrle, S. Trudel, A. Conca Parra, B. Hillebrands, E. Arbelo, C. Herbort, and M. Jourdan. "Brillouin light scattering study of Co2Cr0.6Fe0.4Al and Co2FeAl Heusler compounds". *Journal of Physics D: Applied Physics* 42.8 (2009), p. 084004. ISSN: 0022-3727 1361-6463. DOI: `10.1088/0022-3727/42/8/084004`.

[122] S. Schäfer, V. Kegel, A. A. Serga, B. Hillebrands, and M. P. Kostylev. "Variable damping and coherence in a high-density magnon gas". *Physical Review B* 83.18 (2011), p. 184407. DOI: `10.1103/PhysRevB.83.184407`.

[123] M. Kostylev. “Non-reciprocity of dipole-exchange spin waves in thin ferromagnetic films”. *Journal of Applied Physics* 113.5 (2013), p. 053907. DOI: `10.1063/1.4789962`.

[124] R. E. Arias. “Spin-wave modes of ferromagnetic films”. *Physical Review B* 94.13 (2016), p. 134408. DOI: `10.1103/PhysRevB.94.134408`.

[125] J. Wu, D. Carlton, E. Oelker, J. S. Park, E. Jin, E. Arenholz, A. Scholl, C. Hwang, J. Bokor, and Z. Q. Qiu. “Switching a magnetic vortex by interlayer coupling in epitaxially grown Co/Cu/Py/Cu(001) trilayer disks”. *Journal of Physics: Condensed Matter* 22.34 (2010), p. 342001. ISSN: 0953-8984 1361-648X. DOI: `10.1088/0953-8984/22/34/342001`.

[126] S. Wintz, T. Strache, M. Körner, M. Fritzsche, D. Markó, I. Mönch, R. Mattheis, J. Raabe, C. Quitmann, J. McCord, A. Erbe, and J. Fassbender. “Direct observation of antiferromagnetically oriented spin vortex states in magnetic multilayer elements”. *Applied Physics Letters* 98.23 (2011), p. 232511. DOI: `10.1063/1.3597297`.

[127] S. S. Cherepov, A. Konovalenko, V. Korenivski, and D. C. Worledge. “Micromagnetics of Spin-Flop Bilayers: S, C, and Vortex Spin States”. *IEEE Transactions on Magnetics* 46.6 (2010), pp. 2124–2127. ISSN: 1941-0069. DOI: `10.1109/TMAG.2010.2043716`.

[128] P. Hansen, P. Röschmann, and W. Tolksdorf. “Saturation magnetization of gallium-substituted yttrium iron garnet”. *Journal of Applied Physics* 45.6 (1974), pp. 2728–2732. DOI: `10.1063/1.1663657`.

[129] P. Görnert and C. G. D’Ambly. “Investigations of the growth and the saturation magnetization of garnet single crystals $Y_3Fe_{5-x}Ga_xO_{12}$ and $Y_3Fe_{5-x}Al_xO_{12}$”. *physica status solidi (a)* 29.1 (1975), pp. 95–105. ISSN: 0031-8965. DOI: `10.1002/pssa.2210290111`.

[130] A. A. Serga, A. V. Chumak, and B. Hillebrands. “YIG magnonics”. *Journal of Physics D: Applied Physics* 43.26 (2010), p. 264002. ISSN: 0022-3727 1361-6463. DOI: `10.1088/0022-3727/43/26/264002`.

[131] S. Geller and M. A. Gilleo. “Structure and ferrimagnetism of yttrium and rare-earth-iron garnets”. *Acta Crystallographica* 10.3 (1957), p. 239. ISSN: 0365-110X. DOI: `10.1107/S0365110X57000729`.

[132] R. C. LeCraw, E. G. Spencer, and C. S. Porter. “Ferromagnetic Resonance and Nonlinear Effects in Yttrium Iron Garnet”. *Journal of Applied Physics* 29.3 (1958), pp. 326–327. DOI: `10.1063/1.1723119`.

[133] J. R. Eshbach. “Spin-Wave Propagation and the Magnetoelastic Interaction in Yttrium Iron Garnet”. *Journal of Applied Physics* 34.4 (1963), pp. 1298–1304. DOI: `10.1063/1.1729481`.

[134] R. W. Damon and H. v. d. Vaart. “Dispersion of spin waves and magnetoelastic waves in YIG”. *Proceedings of the IEEE* 53.4 (1965), pp. 348–354. ISSN: 1558-2256. DOI: `10.1109/PROC.1965.3747`.

[135] V. Cherepanov, I. Kolokolov, and V. L’Vov. “The saga of YIG: Spectra, thermodynamics, interaction and relaxation of magnons in a complex magnet”. *Physics Reports* 229.3 (1993), pp. 81–144. ISSN: 0370-1573. DOI: `https://doi.org/10.1016/0370-1573(93)90107-O`.

[136] S. O. Demokritov, V. E. Demidov, O. Dzyapko, G. A. Melkov, A. A. Serga, B. Hillebrands, and A. N. Slavin. “Bose-Einstein condensation of quasi-equilibrium magnons at room temperature under pumping”. *Nature* 443.7110 (2006), pp. 430–3. ISSN: 1476-4687 (Electronic) 0028-0836 (Linking). DOI: `10.1038/nature05117`.

[137] A. V. Chumak, A. A. Serga, and B. Hillebrands. “Magnon transistor for all-magnon data processing”. *Nature Communications* 5.1 (2014), p. 4700. ISSN: 2041-1723. DOI: `10.1038/ncomms5700`.

[138] T. Fischer, M. Kewenig, D. A. Bozhko, A. A. Serga, I. I. Syvorotka, F. Ciubotaru, C. Adelmann, B. Hillebrands, and A. V. Chumak. “Experimental prototype of a spin-wave majority gate”. *Applied Physics Letters* 110.15 (2017), p. 152401. DOI: `10.1063/1.4979840`.

[139] Q. Wang, M. Kewenig, M. Schneider, R. Verba, F. Kohl, B. Heinz, M. Geilen, M. Mohseni, B. Lägel, F. Ciubotaru, C. Adelmann, C. Dubs, S. D. Cotofana, O. V. Dobrovolskiy, T. Brächer, P. Pirro, and A. V. Chumak. “A magnonic directional coupler for integrated magnonic half-adders”. *Nature Electronics* 3.12 (2020), pp. 765–774. ISSN: 2520-1131. DOI: `10.1038/s41928-020-00485-6`.

[140] S. Klingler, A. V. Chumak, T. Mewes, B. Khodadadi, C. Mewes, C. Dubs, O. Surzhenko, B. Hillebrands, and A. Conca. “Measurements of the exchange stiffness of YIG films using broadband ferromagnetic resonance techniques”. *Journal of Physics D: Applied Physics* 48.1 (2014), p. 015001. ISSN: 0022-3727 1361-6463. DOI: `10.1088/0022-3727/48/1/015001`.

[141] F. Groß, N. Träger, J. Förster, M. Weigand, G. Schütz, and J. Gräfe. “Nanoscale detection of spin wave deflection angles in permalloy”. *Applied Physics Letters* 114.1 (2019), p. 012406. DOI: `10.1063/1.5074169`.

[142] J. J. Carmiggelt, O. C. Dreijer, C. Dubs, O. Surzhenko, and T. v. d. Sar. "Electrical spectroscopy of the spin-wave dispersion and bistability in gallium-doped yttrium iron garnet". *Applied Physics Letters* 119.20 (2021), p. 202403. DOI: `10.1063/5.0070796`.

[143] Y. S. Gui, A. Wirthmann, and C. M. Hu. "Foldover ferromagnetic resonance and damping in permalloy microstrips". *Physical Review B* 80.18 (2009), p. 184422. DOI: `10.1103/PhysRevB.80.184422`.

[144] Y. K. Fetisov, C. E. Patton, and V. T. Synogach. "Nonlinear ferromagnetic resonance and foldover in yttrium iron garnet thin films-inadequacy of the classical model". *IEEE Transactions on Magnetics* 35.6 (1999), pp. 4511–4521. ISSN: 1941-0069. DOI: `10.1109/20.809144`.

[145] F. J. Morin. "Magnetic Susceptibility of αFe_2O_3 and αFe_2O_3 with Added Titanium". *Physical Review* 78.6 (1950), pp. 819–820. DOI: `10.1103/PhysRev.78.819.2`.

[146] M. L. Néel. "Essai d'interprétation des propriétés magnétiques du sesquioxyde de fer rhomboédrique". *Ann. Phys.* 12.4 (1949), pp. 249–268.

[147] C. G. Shull, W. A. Strauser, and E. O. Wollan. "Neutron Diffraction by Paramagnetic and Antiferromagnetic Substances". *Physical Review* 83.2 (1951), pp. 333–345. DOI: `10.1103/PhysRev.83.333`.

[148] R. Lebrun, A. Ross, O. Gomonay, V. Baltz, U. Ebels, A. L. Barra, A. Qaiumzadeh, A. Brataas, J. Sinova, and M. Kläui. "Long-distance spin-transport across the Morin phase transition up to room temperature in ultra-low damping single crystals of the antiferromagnet α-Fe2O3". *Nature Communications* 11.1 (2020), p. 6332. ISSN: 2041-1723. DOI: `10.1038/s41467-020-20155-7`.

[149] P. R. Elliston and G. J. Troup. "Some antiferromagnetic resonance measurements in α-Fe2O3". *Journal of Physics C: Solid State Physics* 1.1 (1968), pp. 169–178. ISSN: 0022-3719. DOI: `10.1088/0022-3719/1/1/320`.

[150] J. O. Artman, J. C. Murphy, and S. Foner. "Magnetic Anisotropy in Antiferromagnetic Corundum-Type Sesquioxides". *Physical Review* 138.3A (1965), A912–A917. DOI: `10.1103/PhysRev.138.A912`.

[151] R. Lebrun, A. Ross, O. Gomonay, S. A. Bender, L. Baldrati, F. Kronast, A. Qaiumzadeh, J. Sinova, A. Brataas, R. A. Duine, and M. Kläui. "Anisotropies and magnetic phase transitions in insulating antiferromagnets determined by a Spin-Hall magnetoresistance probe". *Communications Physics* 2.1 (2019), p. 50. ISSN: 2399-3650. DOI: `10.1038/s42005-019-0150-8`.

[152] J. Han, P. Zhang, Z. Bi, Y. Fan, T. S. Safi, J. Xiang, J. Finley, L. Fu, R. Cheng, and L. Liu. "Birefringence-like spin transport via linearly polarized antiferromagnetic magnons". *Nature Nanotechnology* 15.7 (2020), pp. 563–568. ISSN: 1748-3395. DOI: `10.1038/s41565-020-0703-8`.

[153] T. Wimmer, A. Kamra, J. Gückelhorn, M. Opel, S. Geprägs, R. Gross, H. Huebl, and M. Althammer. "Observation of Antiferromagnetic Magnon Pseudospin Dynamics and the Hanle Effect". *Physical Review Letters* 125.24 (2020). PRL, p. 247204. DOI: `10.1103/PhysRevLett.125.247204`.

[154] M. Fuller. "Experimental Methods in Rock Magnetism and Paleomagnetism". In: *Methods in Experimental Physics*. Ed. by C. G. Sammis and T. L. Henyey. Vol. 24. Academic Press, 1987, pp. 303–471. ISBN: 0076-695X. DOI: `https://doi.org/10.1016/S0076-695X(08)60590-6`.

[155] A. H. Morrish. *Canted Antiferromagnetism: Hematite*. 1995. DOI: `10.1142/2518`.

[156] J. W. Anthony, R. A. Bideaux, K. W. Bladh, and M. C. Nichols. *Hematite*. Handbook of Mineralogy. Chantilly, USA: Mineralogical Society of America, 2001.

[157] E. J. Samuelsen and G. Shirane. "Inelastic neutron scattering investigation of spin waves and magnetic interactions in α-Fe2O3". *physica status solidi (b)* 42.1 (1970), pp. 241–256. ISSN: 0370-1972. DOI: `https://doi.org/10.1002/pssb.19700420125`.

[158] T. Riste and A. Wanic. "A neutron diffraction study of spin fluctuations in α-Fe2O3". *Journal of Physics and Chemistry of Solids* 17.3 (1961), pp. 318–333. ISSN: 0022-3697. DOI: `https://doi.org/10.1016/0022-3697(61)90198-6`.

Acknowledgements

The work presented in this thesis would not have been possible without the help and support of numerous people. Over the course of my PhD, I got to meet and work with many great people and I would like to thank all of you.

First of all, special thanks to my supervisor Sebastian Wintz for introducing me to the world of spin waves and for guiding me through all of my projects. A huge thank you for your excellent support, your great ideas and the fun we had, especially at beamtimes! Thanks also for your positive outlook on life in general and on my projects in particular!

Many thanks to my boss Jörg Raabe for the continuous support during my thesis. Thanks for being able to calmly find a solution to any kind of problem and for giving me the freedom to work independently!

I would like to thank Laura Heyderman for being my academic advisor. Thanks for welcoming me as a guest in your group and for your valuable feedback on my writing. I would also like to thank Pietro Gambardella for stepping in as a co-advisor.

A big thank you to Simone Finizio. You have the most incredible knowledge of sample fabrication, imaging beamlines and Swiss mountains, thank you for sharing it with me! Without your ebeam lithography magic, several of my projects would not have been possible.

Many thanks to Aleš Hrabec for being the best Commanding Director of Research that I could have wished for. Thanks for your advice on antiferromagnets, sputtering and my papers as well as for securing me a desk in your office.

I am grateful to everyone who supported me on beamtime at Maxymus. Many thanks to Markus Weigand for knowing the beamline inside out, Johannes Förster for the night shifts together, Hermann Stoll for the high-frequency support and the early morning check-up calls, Joachim Gräfe, Joe Bailey, Frank Schulz and Michael Bechtel.

I would like to thank Joakim Reuteler for the help with the Xe PFIB and in developing the window thinning process. You always managed to find time for me and a solution for my problems! Many thanks to Stefan Stutz for help with the lapping and polishing process and for always trying to improve things. Thanks to Elisabeth Müller for the initial discussions about thinning samples.

Many thanks to the LMN cleanroom team and in particular to Vitaliy Guzenko, Koni Vogelsang, Dario Marty and Christopher Wild for advice and help. For the NiO annealing, I'd like to thank Darek Gawryluk.

Many thanks to Lukáš Flajšman for proposing the spin-wave focusing project and doing simulations for it. Thanks also to you and Michal Urbánek for coming to PSI for beamtime. Thanks to Jonathan Leliaert and Bartel Van Waeyenberge for performing simulations for the Ga:YIG. Many thanks to Rodolfo Gallardo for the script for numerical calculations of spin-wave dispersions. Many thanks to Carsten Dubs for growing amazing Ga:YIG samples. Thanks to Kilian Lenz, Antje Oelschlägel and Charlotte Hermann for performing FMR measurements on them. Regarding the hematite project, I would like to thank Phani Arekapudi and Olav Hellwig for the initial discussions and Fabian Ganss and Benny Böhm for doing SQUID measurements. Thanks to Anna Semisalova for performing AFMR measurements and to Rysard Narkovic for CPW calculations.

Thanks to Martina Füglister, Margit Braun-Shea and Liz Hoss for helping me navigate through the administrative jungles of PSI and ETH. Thanks also to the guys at the PSI post office!

My time at PSI would not have been so nice without the people there and I am thankful for all the support that I got from my two groups. From the Mesosytos, I would like to thank my girls Laurita, Diane, Claire and Susmita for always cheering me up when my stuff didn't work, Rhea for all the great chats over coffee and ice cream, Namrata for being my deadline mate, Eugenie for helping me get started, Paolo for the great time in Sweden, Jizhai for the random knowledge, Kevin, Sergii and Federico for the QBBQs, Jingyuan for our fun time at ESM, Anja for always organising everything, Gavin, Phönsi, Dominik, Aleks, Sam, Michael, Zhaochu, Alex, Zhentao, Jamie and Valerio. At PolLux, my thanks go to Kathy for the support when the boys were going crazy, Manu for our long discussions, Blagoj, Sebastian G., Ben and Lars. Many thanks for all the nice chats at the beamline coffee table and couch also to the guys at NanoXAS: Zbynek, Nicolo, Trey and Luca.

I would like to also thank my friends outside of work for the great conversations over drinks and dinners, for the wonderful outdoor adventures and for listening to my rambling about failed samples and experiments: Steffi and little Max, Darya, Martin, Alex, Marjam, and Manu!

Finally, many thanks to my parents for their continuous love and support throughout my entire life. This would not have been possible without you. Vielen Dank für alles!

List of Publications

- S. Finizio, S. Wintz, K. Zeissler, A. V. Sadovnikov, **S. Mayr**, S. A. Nikitov, C. H. Marrows, and J. Raabe. "Dynamic Imaging of the Delay- and Tilt-Free Motion of Neel Domain Walls in Perpendicularly Magnetized Superlattices". *Nano Letters* 19.1 (2019), pp. 375–380. issn: 1530-6984. doi: 10.1021/acs.nanolett.8b04091.

- S. Finizio, K. Zeissler, S. Wintz, **S. Mayr**, T. Weßels, A. J. Huxtable, G. Burnell, C. H. Marrows, and J. Raabe. "Deterministic Field-Free Skyrmion Nucleation at a Nanoengineered Injector Device". *Nano Letters* 19.10 (2019), pp. 7246–7255. issn: 1530-6984. doi: 10.1021/acs.nanolett.9b02840.

- J. Förster, J. Gräfe, J. Bailey, S. Finizio, N. Träger, F. Groß, **S. Mayr**, H. Stoll, C. Dubs, O. Surzhenko, N. Liebing, G. Woltersdorf, J. Raabe, M. Weigand, G. Schütz, and S. Wintz. "Direct observation of coherent magnons with suboptical wavelengths in a single-crystalline ferrimagnetic insulator". *Physical Review B* 100.21 (2019), p. 214416. doi: 10.1103/PhysRevB.100.214416.

- C. Donnelly, S. Finizio, S. Gliga, M. Holler, A. Hrabec, M. Odstrčil, **S. Mayr**, V. Scagnoli, L. J. Heyderman, M. Guizar-Sicairos, and J. Raabe. "Time-resolved imaging of three-dimensional nanoscale magnetization dynamics". *Nature Nanotechnology* (2020). issn: 1748-3395. doi: 10.1038/s41565-020-0649-x.

- Z. Luo, A. Hrabec, T. P. Dao, G. Sala, S. Finizio, J. Feng, **S. Mayr**, J. Raabe, P. Gambardella, and L. J. Heyderman. "Current-driven magnetic domain-wall logic". *Nature* 579.7798 (2020), pp. 214–218. issn: 1476-4687. doi: 10.1038/s41586-020-2061-y.

- S. Finizio, S. Wintz, **S. Mayr**, A. J. Huxtable, M. Langer, J. Bailey, G. Burnell, C. H. Marrows, and J. Raabe. "Current-induced dynamical tilting of chiral domain walls in curved microwires". *Applied Physics Letters* 116.18 (2020), p. 182404. doi: 10.1063/5.0005186.

- S. Finizio, **S. Mayr**, and J. Raabe. "Time-of-arrival detection for time-resolved scanning transmission X-ray microscopy imaging". *Journal of Synchrotron Radiation* 27.5 (2020). issn: 1600-5775. doi: 10.1107/S1600577520007262.

- S. Finizio, S. Wintz, **S. Mayr**, A. J. Huxtable, M. Langer, J. Bailey, G. Burnell, C. H. Marrows, and J. Raabe. “Time-resolved visualization of the magnetization canting induced by field-like spin–orbit torques”. *Applied Physics Letters* 117.21 (2020), p. 212404. doi: 10.1063/5.0029816.

- **S. Mayr**, L. Flajšman, S. Finizio, A. Hrabec, M. Weigand, J. Förster, H. Stoll, L. J. Heyderman, M. Urbánek, S. Wintz, and J. Raabe. “Spin-Wave Emission from Vortex Cores under Static Magnetic Bias Fields”. *Nano Letters* 21.4 (2021), pp. 1584–1590. issn: 1530-6984. doi: 10.1021/acs.nanolett.0c03740.

- Z. Luo, S. Schären, A. Hrabec, T. P. Dao, G. Sala, S. Finizio, J. Feng, **S. Mayr**, J. Raabe, P. Gambardella, and L. J. Heyderman. “Field- and Current-Driven Magnetic Domain-Wall Inverter and Diode”. *Physical Review Applied* 15.3 (2021), p. 034077. doi: 10.1103/PhysRevApplied.15.034077.

- **S. Mayr**, S. Finizio, J. Reuteler, S. Stutz, C. Dubs, M. Weigand, A. Hrabec, J. Raabe, and S. Wintz. “Xenon Plasma Focused Ion Beam Milling for Obtaining Soft X-ray Transparent Samples”. *Crystals* 11.5 (2021), p. 546. issn: 2073-4352. doi: 10.3390/cryst11050546.

- **S. Mayr** and S. Wintz. “Increasing the signal bandwidth - From ferromagnetic to antiferromagnetic magnonic systems”. As part of A.V. Chumak et al. “Roadmap on Spin-Wave Computing”. url: arxiv.org/abs/2111.00365, *submitted for publication.*

- S. Pile, S. Stienen, K. Lenz, R. Narkowicz, S. Wintz, J. Förster, **S. Mayr**, M. Buchner, M. Weigand, V. Ney, J. Lindner, and A. Ney. “Nonstanding spin waves in a single rectangular permalloy microstrip under uniform magnetic excitation”. url: https://arxiv.org/abs/2111.07773, *submitted for publication.*

- S. Finizio, C. Donnelly, **S. Mayr**, A. Hrabec, and J. Raabe. “Three-Dimensional Vortex Gyration Dynamics Unraveled by Time-Resolved Soft X-ray Laminography”. url: https://arxiv.org/abs/2111.13533, *submitted for publication.*

- J. Bailey, S. Finizio, J. Förster, **S. Mayr**, M. Weigand, C. Dubs, E. Josten, J. Gräfe, J. Dreiser, E. Goering, J. Raabe, G. Schütz, G. Aeppli and S. Wintz. “X-ray magnetic linear dichroism for time resolved imaging of axial spin dynamics on the nanometre length and picosecond timescale”. *unpublished.*

- **S. Mayr**, J. Förster, S. Finizio, R.A. Gallardo, R. Narkovic, G. Dieterle, K. Schultheiss, A. Semisalova, J. Bailey, E. Kirk, J. Lindner, J. Gräfe, J. Raabe, G.

Schütz, M. Weigand, H. Stoll, and S. Wintz. “Time-resolved x-ray imaging of spin dynamics at tens of GHz using low-alpha synchrotron operation”. *unpublished*.